DETERMINATION OF REACTION KINETICS AND MECHANISMS OF 1.13NM TOBERMORITE BY IN-SITU NEUTRON DIFFRACTION

Saskia Bernstein

Dissertation

Fakultät für Geowissenschaften

der Ludwig-Maximilians-Universität

München

vorgelegt von

Saskia Bernstein

aus Schönebeck

München den 12.Januar 2011

Erstgutachter: *Prof. Dr. Karl Thomas Fehr*

Zweitgutachter: *Prof. Dr. Herbert Pöllmann*

Tag der Disputation: *27. Mai 2011*

the cupola of the pantheon in Rome, build by the Romans using the oldest concrete-like material of the world - Opus Caementitium

Table of Content

Chapter 3: HAND: An Hydrothermal Autoclave for Neutron Diffraction

Chapter 4: Reaction and growth kinetics of 1.13nm tobermorite crystallizing in AAC

Chapter 5:outlook

List of figures

Chapter 1.

Chapter 2.

Chapter 3.

Chapter 4.

Danksagung

Jetzt, da diese Arbeit anscheinend doch noch ein gutes Ende findet, ist es an der Zeit, denjenigen zu danken, die mich auf diesem doch recht langen und oft auch steinigen Weg begleitet haben. Es sind in 6 Jahren so viele gewesen, dass Ihr mir hoffentlich nicht böse seid, wenn ein paar ungenannt bleiben.

Zunächst einmal gilt mein innigster Dank meinen Eltern, die mich immer auf jede erdenkliche Weise unterstütz haben und die mir wenn ich es brauchte zur Seite standen. Ohne euch wäre ich nicht da wo ich jetzt bin.

Meinem Betreuer möchte ich danken für die Möglichkeit zu dieser Doktorarbeit. Ich danke ihm für all die Möglichkeiten zur Diskussion, für die vielen ermutigenden, manchmal auch strengen Worte, für den Freiraum den er mir gelassen hat und nicht zuletzt für den Kaffee, der immer bereit stand. Danke Tommi !

Ein ganz besonderes Dankeschön geht an Andi Laumann, dem besten Zuhörer den ich kenne. Dafür das er wusste, mit meinen Launen umzugehen aber vor allem dafür, dass er die vergangenen 10 Jahre immer ein guter Freund war und es hoffentlich auch noch in den folgenden sein wird.

Meiner Nuria danke ich für ihr Verständnis, für die stundenlangen Gespräche und für den Spaß den wir zusammen hatten... un besito

Dir Pablo danke ich einfach nur fürs zur Seite stehen, manchmal sicher die schwerste Aufgabe.

Danke an Yaping, Andi, Christoph, Michi, Felix und Linda, dass sie mein kreatives Chaos ertragen haben, welches manchmal doch recht raumfüllend war und einfach dafür dass sie die besten Büro-Kollegen sind die man sich vorstellen kann.

Dem Freistaat Bayern möchte ich danken, dass er mir diese Arbeit überhaupt ermöglicht hat durch die finanzielle Unterstützung mittels einem Stipendium nach dem „Bayerischen Eliteförderungsgesetz“

Dr. Rupert Hochleitner, Kurator der Mineralogischen Staatssammlung danke ich für die Bereitstellung zahlreicher Mineralien, die ich für meine Untersuchungen benötigte.

Ich danke auch allen, die an der Entwicklung und des Baus der für die Experimente benötigten Autoklaven beteiligt waren.

Herrn Tom Hansen danke ich ganz besonders für die Unterstützung zu jeder Tages. - und Nachtzeit während der Messzeiten am ILL. Ohne ihn gäbe es die Daten nicht, die den Kern dieser Arbeit bilden.

Summary

1.13nm tobermorite belongs to the mineral group of calcium-silicate-hydrates or short CSH-phases. Natural CSH-phases are due to the specific areas of formation rare in nature but synthetic members have applications in many different sections of the industry. 1.13nm tobermorite for example is the main binding phase in aerated autoclaved concrete (AAC), a building material which became more and more important over the last decades. It is easy to process due to its low density but nevertheless offers an excellent strength resistance caused by the interlocking lathlike tobermorite crystals. The embodied air filled pores effect very good insulation behaviour, which is of great importance for an ecologically sensitive method of construction. Despite the high significance of AAC for the building industry the standard of knowledge referring to the ongoing processes during production is still not satisfying. The applied conditions during the production are in part based on empirical values and just the macroscopic properties of the product are controlled. The macroscopic properties are primary determined by the microscopic ones, like type and amount of formed mineral phases and their structure and texture. Several scientific studies dealing with this topic are already published but the hence resulting set of data on mineral forming processes and their kinetics is still deficient. Previous studies have shown that the formation of 1.13nm tobermorite is just metastable under the conditions present during productions. In equilibrium 1.13nm tobermorite decomposes to xonotlite and quartz, which has a fatal influence on the strength resistance of the building material. Therefore the present work addresses in detail on the determination of the reaction kinetics of the formation of 1.13nm tobermorite within the system $CaO\text{-}SiO_2\text{-}H_2O$ by in situ neutron diffraction. To assure a successful interpretation of the experimental data, crystallographic well

characterised sample material is needed. Therefore the crystal chemistry of natural xonotlites was previously studied and the results are integrated in the presented work. The neutron diffraction experiments were conducted at three different temperatures and to different grain sizes of quartz to determine the influence of these parameters. The experiments were carried out at the D20 powder diffractometer of the the Institute Laue Langevin research reactor in Grenoble (France). For this purpose an autoclave (HAND) was designed which enables an investigation of the previously synthesized greenbodies under saturated steam pressure. The high neutron flux at the D20 provides a time resolution of 1 exposure per minute, hence sufficient data for the early state of the reaction could be collected as well. The obtained diffraction pattern were evaluated with respect to the reaction progress and subsequently interpreted in terms of the present reaction process by using a kinetic model. It could be shown that the formation of 1.13nm tobermorite is a non-isokinetic process with changes in the reaction mechanism from solution control to diffusion control and in most of the cases back to diffusion control. The determined transition times and points of portlandite expense and tobermorite occurrence were compared with respect to the influence of reaction temperature and grain size of quartz. Based on the data for the reaction progress, the rate constant for the different sections of the reaction were calculated. Using the rate constants determined at different temperatures the activation energies of the tobermorite formation were calculated.

Zusammenfassung

1.13nm Tobermorite gehört zur Mineralgruppe der Calciumsilikathydrate oder kurz CSH-Phasen. Natürliche Vertreter dieser Gruppe sind aufgrund der speziellen Bildungsräume in der Natur eher selten, synthetische CSH-Phasen finden jedoch Anwendung in den verschiedensten Bereichen der Industrie. 1.13nm Tobermorite zum Beispiel ist die primäre Phase in Porenbeton, einem Baustoff der in den letzen Jahrzehnten immer mehr an Bedeutung gewann. Er ist aufgrund seiner geringen Dichte leicht zu verarbeiten, bietet aber trotzdem hervorragende Festigkeitseigenschaften durch die Verzahnung der lattenförmigen Tobermoritkristalle. Die enthaltenen luftgefüllten Poren bewirken außerdem sehr gute Dämmeigenschaften, welche für eine ökologische umweltbewusste Bauweise von hoher Bedeutung sind. Trotz des hohen Stellenwertes von Porenbetonprodukten in der Bauindustrie ist der Wissensstand über die während der Herstellung ablaufenden Prozesse noch unbefriedigend. Die während der Herstellung herrschenden verwendeten Produktionsbedingungen beruhen meist auf empirischen Werten und überprüft werden nur die makroskopischen Eigenschaften des fertigen Baustoffs. Die makroskopischen Eigenschaften werden aber primär durch die mikroskopischen Eigenschaften, sprich Menge und Art der entstehende Mineralphasen und deren Struktur und Textur, bestimmt werden. Mehrere wissenschaftliche Arbeiten zu diesem Thema wurden bereits veröffentlicht, der daraus resultierende Datensatz bezüglich der ablaufenden Mineralbildungsprozesse und deren Kinetik ist aber immer noch unzureichend. In vorangegangenen Arbeiten wurde gezeigt, dass sich 1.13nm Tobermorit im Porenbeton unter den gegebenen Bedingungen nur metastabil bildet. Unter Gleichgewichtbedingungen zerfällt dieser zu Xonotlite und Quarz, was sich in verheerendem Maße negativ auf die Festigkeitseigenschaften des Baustoffs

auswirken würde. Die vorliegende Arbeit befasst sich daher eingehend mit der Bestimmung der Reaktionskinetik von 1.13nm Tobermorit im System CaO-SiO_2-H_2O mittels in situ Neutronenbeugung..Um die in den Versuchen gewonnenen Daten erfolgreich auswerten zu können, erfordert es kristallographisch gut charakterisiertes Probenmaterial. Aus diesem Grund wurde die Kristallchemie von natürlichen Xonotliten im Vorfeld eingehend studiert und die gewonnenen ergebnisse sollen mit in die vorliegende Arbeit einfließen. Die Neutronenbeugungs-Experimente wurden bei drei verschiedenen Temperaturen und mit zwei unterschiedlichen Korngrößen der Quartzfraktion durchgeführt, um den Einfluss dieser Parameter beurteilen zu können Die in die Auswertung einbezogenen Experimente wurden am D20 Pulverdiffraktometer des Forschungsneutronenreaktors des Instituts Laue-Langevin in Grenoble (Frankreich) durchgeführt. Hierfür wurde eigens ein Autoklav (HAND) entwickelt, der es ermöglicht die zuvor hergestellten Grünkörper unter gesättigter Dampfatmosphäre zu untersuchen. Der hohe Neutronenfluss am D20 ermöglicht eine zeitliche Auflösung von 1 Diffraktogramm pro Minute, so konnten genügend Daten für das Frühstadium der Reaktion gesammelt werden. Die so erhaltenen Aufnahmen wurden bezüglich des Reaktionsumsatzes ausgewertet und mithilfe von kinetischen Modellen hinsichtlich des Reaktionsmechanismus interpretiert. Es zeigte sich das die Bildung von 1.13nm Tobermorit nicht isokinetisch ist, sondern zunächst ein lösungskontrollierter Abschnitt vorliegt welcher übergeht in einen diffusionskontrollierten Teil und in den meisten Fällen erneut wechselt zu einem lösungskontrollierten Abschnitt. Die so erhaltenen Üebergangszeiten und Zeitpunkte des vollständigen Verbrauchs von Portlandit und des ersten Auftretens von 1.13nm Tobermorit wurden hinsichtlich des Einflusses von Reaktionstemperatur und Quarzkorngröße miteinander verglichen. Aus den Daten wurden anschließend die Geschwindigkeitskonstanten für die verschiedenen Abschnitte der Reaktion

berechnet. Aus den so erhaltenen Geschwindigkeitskonstanten bei verschiedenen Temperaturen konnten die Aktivierungsenergien bestimmt werden.

Chapter 1: Introduction

1.1 Calcium Silicate Hydrates (CSH)

Calcium-silicate-hydrates are mineral phases mostly formed in weathered and hydrothermally altered basic rocks. One of the most famous deposits is known from Maroldsweisach, Bavaria, where natural calcium-silicate-hydrates are found in xenolites inside basalt. Due to the spatial and in terms of geology short occurrence of the needed formation conditions, calcium silicate hydrates are rather rare. The huge variety and the complicate crystal chemistry despite a simple composition of calcium silicium and water (Fig:1.1) made them subject of several studies. But their main importance lies in the construction industry. Calcium-silicate-hydrates are the main binding phases in many building materials. The basic principal is the bonding of grained materials by inorganic or hydraulic binders like lime and portland cement, respectively. As most common and widespread material concrete needs to be mentioned. Concrete can be described as artificial chemical sedimentary rock where aggregates like sand or gravel are bonded by the crystallizing phases in the cement after adding water. The acicular crystals are interlock with each other causing the desired resistance and constructive strength of

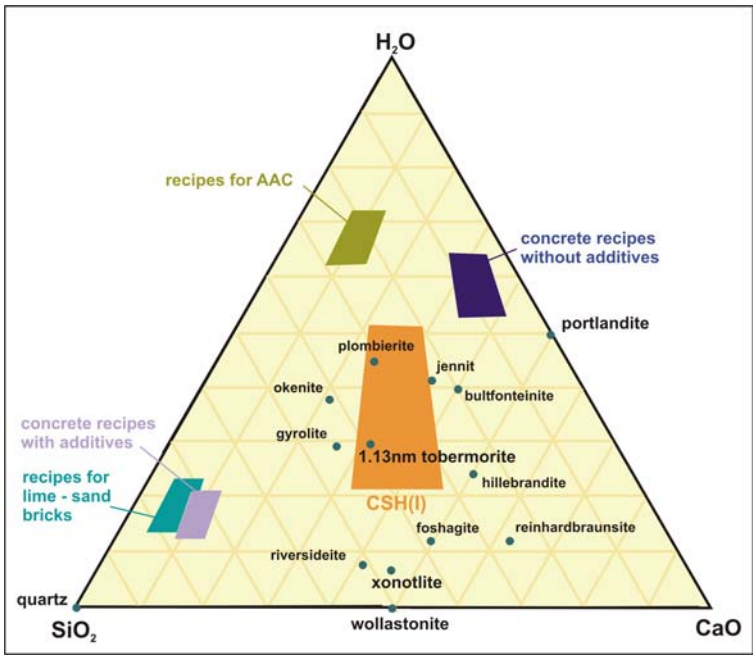

Fig.1.1.: ternary system CaO-SiO2-H2O with some of the most important natural CSH-phases and the composition of recipes of common building materials

the material. Already 2000 years ago the Romans had this knowledge and used the first concrete like building material known as OPUS CAEMENTITIUM for their monumental examples of architecture like the pantheon (cover picture) or the colosseum in Rome. But beside concrete ,steam cured building materials like lime-sand bricks and aerated autoclaved concrete gained more and more importance in our era.

1.2. Aerated autoclaved concrete

1.2.1 History

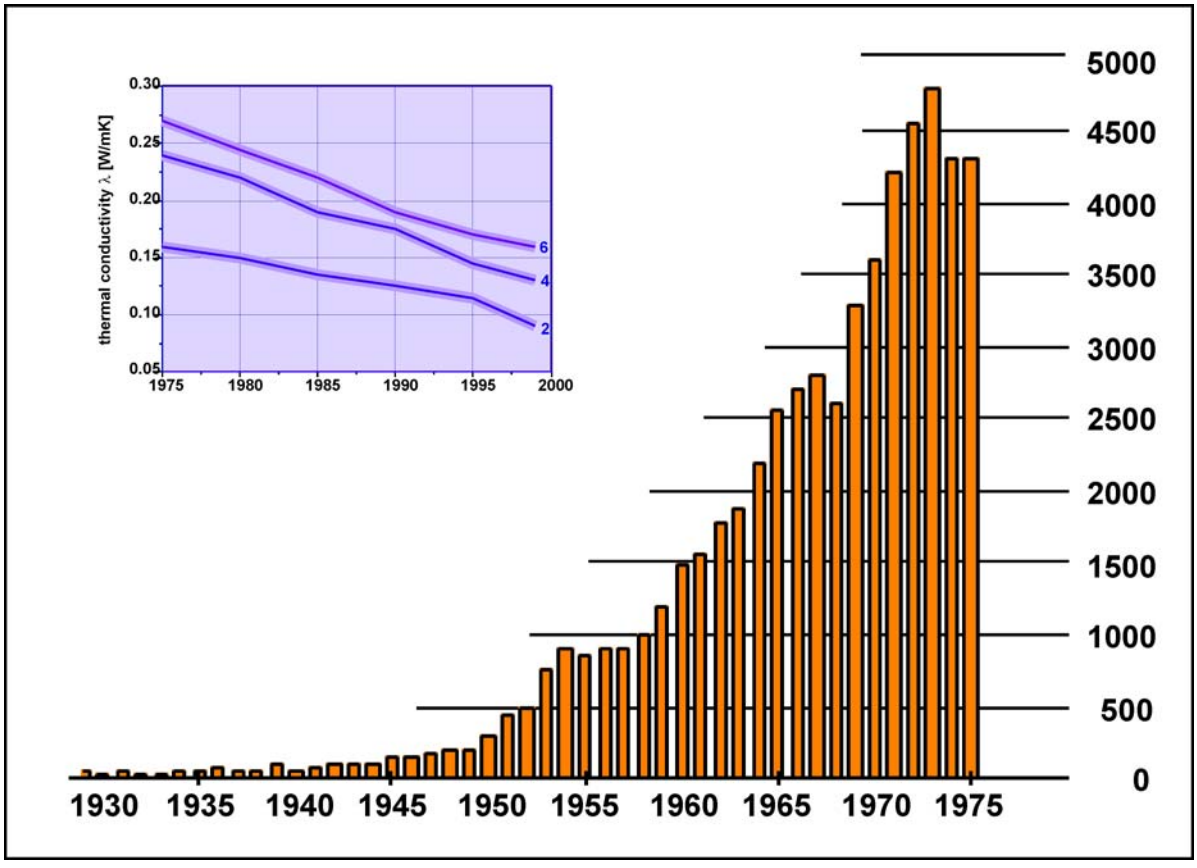

Fig.1.2: increase of YTONG products in $10^3 m^3$ from 1930 to 1975 and improvement of thermal conductivity from 1975 to 2000 for the strength categories 2, 4 and 6 madified after Dubral (1992)

Due to the scarcity of energy and recourses after the First World War the governments of many European countries tightened the requirements of building materials in terms of insulation behaviour and cost of production and supported a lot of scientific research. In 1924 the Swedish scientist A. Eriksson developed the basic method of producing aerated autoclaved concrete based on the preliminary work of Zernikov and Michaelis on lime sand mortar combined with the pore-forming method of Aylsworth and Dyer by adding metal powders to the mixture. The material is outstanding for its good heat insulation behaviour caused by the pores (Fig.1.2.) and a high compressive strength despite a low density.

1.2.2 Industrial production

The first industrial production started in 1929 in Yxhult (Sweden) intrducing the trade name YTONG (**Y**XHULTS ÅNGEHÄRDADE GASBE**TONG).** The number of plants increased over the thirties due to the huge demand. The Second World War temporarily haltered the quick spread of AAC but nevertheless the development of

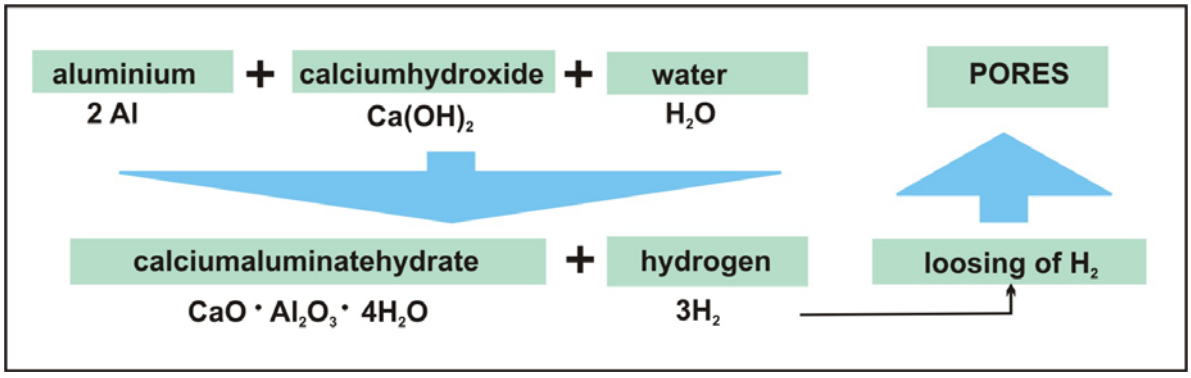

Fig.1.3.:formation of pores by the alkaline reaction of Al and Ca(OH) after Homann (2008)

AAC product worldwide increased immensely between 1929 and 1975 as depicted in Fig.1.2. Today the annual production In western Europe add up to 8.65 mio m³ over 50% of which are produced in Germany (Dubral, 1992).The global success was first

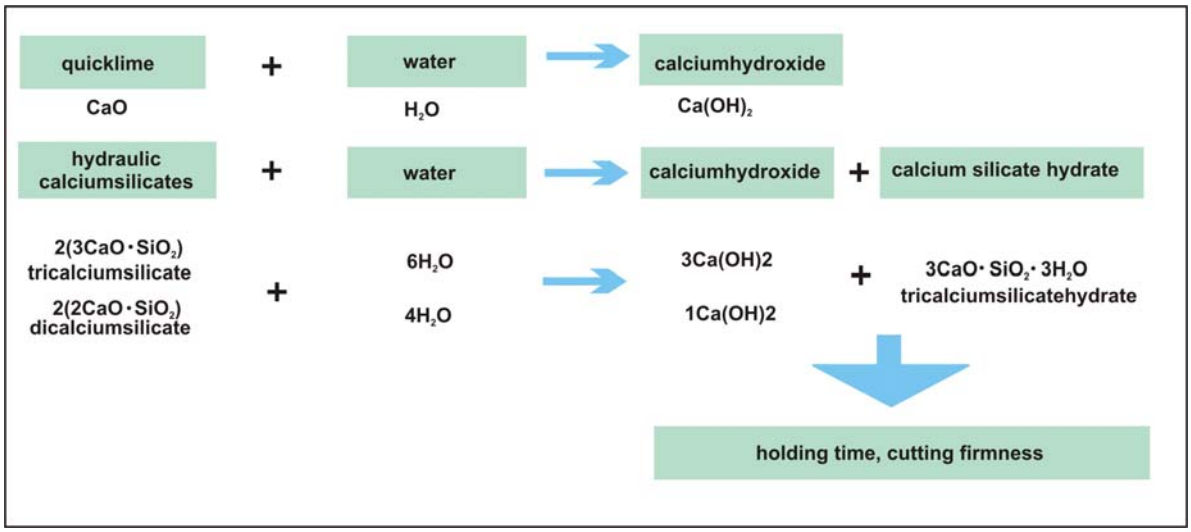

Fig.1.4: hydration of CaO and cement clinker phases to form ca(OH) and Ca(OH) and tricalcium silicate hydrate,respectively, modified after Homan (2008)

of all established by the companies YTONG, Siporex and Durox.

Over the years some improvements were made on the industrial production of AAC like cutting with wires instead of saw but the main concept stayed the same. After grinding the raw materials lime, sand and cement are mixed followed by an exhaustive dispersing with water. To safe cost the waste from cutting and recycled

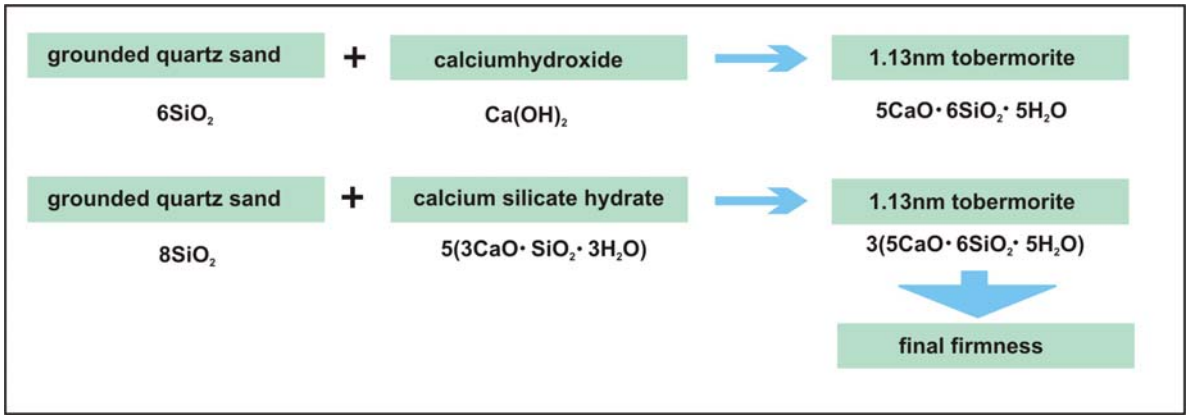

Fig.1.5.: formation of 1.13nm tobermorite by the reaction of ground quartz and Ca(OH) or calcium silicate hydrate, respectively, modified after Homan (2008)

AAC is added to the raw materials as well as anhydrite or gypsum to advance the formation of the desired mineral phase. Right before pouring the paste through the moulds aluminium is added to the mixture as pore-builder. The paste rests for about

two hours at elevated temperatures. During that time pores are formed by the reaction of aluminium with calcium hydroxide and water (see Fig 1.3) causing an expansion of the cake. Meanwhile the quicklime and the cement clinker phases dicalciumsilicate (C_2S) and tricalciumsilicate (C_3S) react with water to form calcium hydroxide and calciumhydroxide and tricalciumsilicatehydrate, respectively (see fig.1.4) and a basic resistance is reached. The greenbody is removed from the mould, cut and stored in the autoclaves for hydrothermal curing. The curing normally takes place at temperatures around 190°C and saturated steam pressure (12.5bar) over a time span of 6 up to 12h. During autoclaving the crystalline phase 1.13nm tobermorite is formed by the reactions shown in (Fig 1.5)

1.2.3 Properties

The material AAC is outstanding for its high compressive strength despite a very low weight and density due to the pores. The pores causing as well a extremely good heat and acoustic insulation behaviour. Important values to determine quality of the building material are the shrinkage, the e-modul and the heat conductivity which are monitored regularly during production. Those values are optimized in the industrial production process by changing the ratio of the different raw materials and therefore the raw density of the “cake” as explained in the unpublished report resulting from an internship in an AAC-plant in Bourgoin Jallieu, France (appendix A).

This empiric method in fact leads to the desired results but the scientific research of the last decades has shown that the macroscopic properties of AAC and other construction materials are controlled by the microscopic ones, speaking of the type and structure of the evolving CSH-phases. A targeted control of the ongoing mineral forming reactions and therefore the macroscopic properties of AAC is just possible

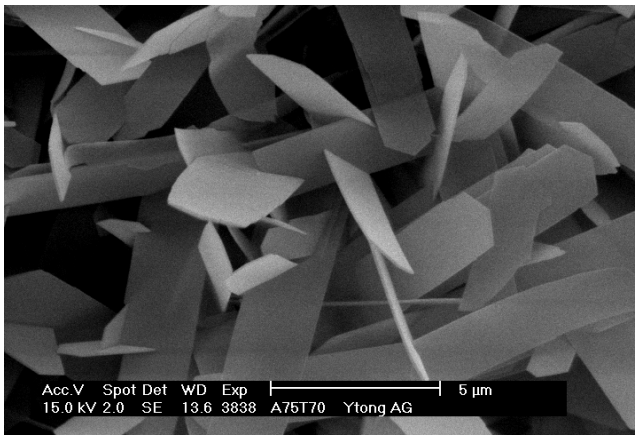

Fig.1.6: network of lathlike tobermorite crystals in AAC

with an extensive quantitative knowledge of the structural characteristics, the thermodynamic parameters and the reaction kinetic. Despite the intense research of the last decades this is still insufficient and should be the main aim of the presented work. The influence of temperature and grain size of quartz on the formation of 1.13nm tobermorite was studied by in-situ neutron diffraction. Based on the experiments detailed information on the reaction mechanisms were obtained and beyond that rate constants and activation energies were calculated as explained in the chapter 4.

1.3 Tobermorite in AAC

As mentioned before (Fig. 1.4), 1.13nm tobermorite is the main phase evolving during the hydrothermal hardening of AAC. The lathlike crystals interlock to each other to form a network causing the good compressive strength of the product (Fig. 1.6). The tobermorite-forming reactions does not reach the chemical equilibrium within the technical time scales, thus under the chosen curing conditions

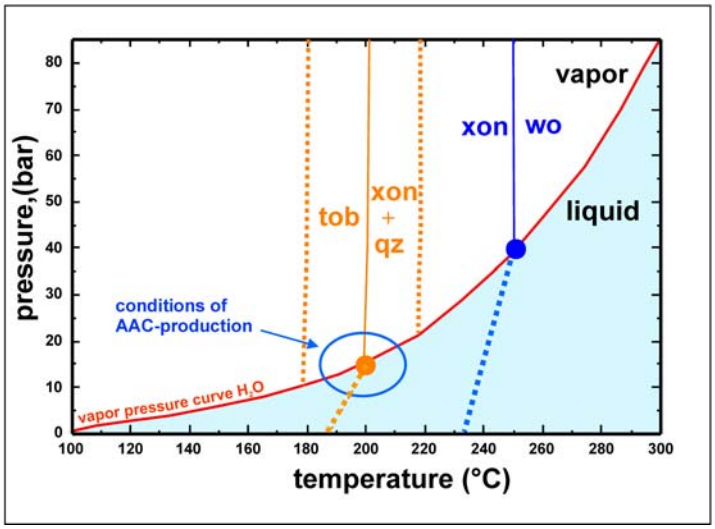

Fig.1.7: p-T diagram of tobermorite stability

the formed 1.13nm tobermorite is stabilized metastable (Gabrosek *et al*., 1993; Fehr and Zuern, 1997; Zuern and Fehr,2000.). Under equilibrium conditions 1.13nm tobermorite decomposes to xonolite and quartz (fig.1.7). Xonotlite has a fibrous structure which would remarkably decrease the compressive strength of the brick.

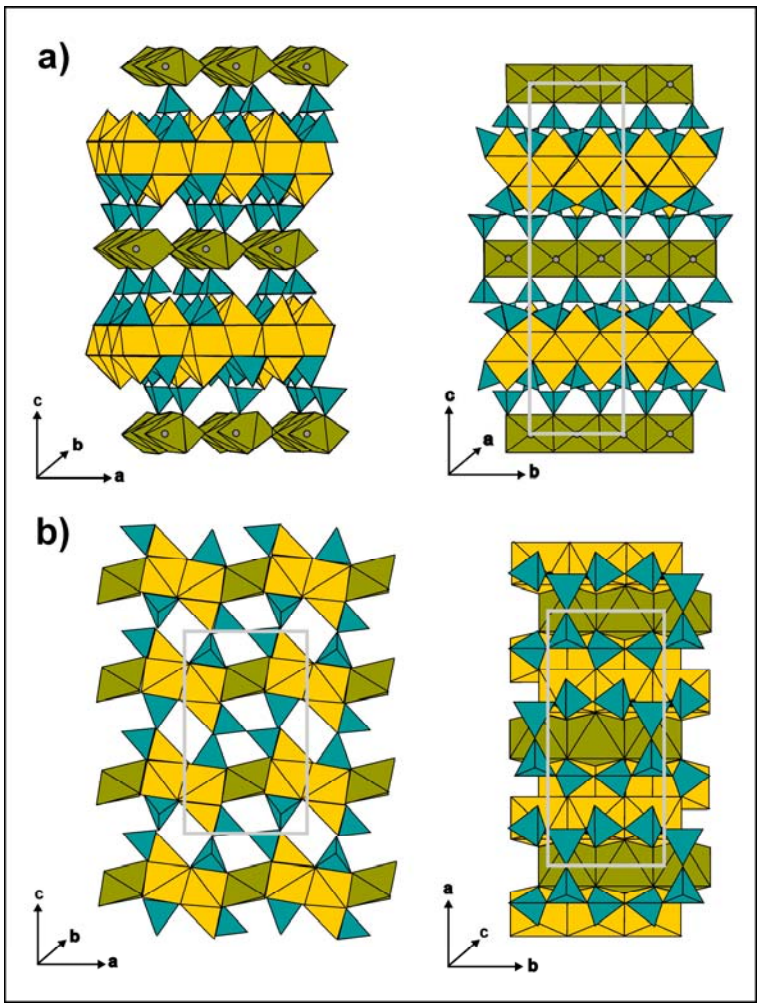

Fig.1.8: structure of tobermorite (a) and xonotlite (b) modified after Bonaccorsi et al (2005) and Hejny & Armbruster (2001)

Both 1.13nm tobermorite and xonotlite show the characteristic structural features of infinite silicate double chains of a type called *Dreier-Doppelketten* built up of condensed *Dreierketten* common to almost all CSH-Phases (fig.1.8). The chains are intercalated by a Ca-O layer (portlandite layer) so the structure consists of a central layer of calcium octahedra which has silicate sheets on each side. The calcium octahedra share oxygens with the silicate tetrahedra, the distance between two edges in the calcium octahedral layer is about the same length as a silicate *Dreierketten* unit. This feature enables differing linkage possibilities of Ca and Si layers and therefore polytism occurs. For both xonotlite and tobermorite several polytypes are known. Often the crystals show an intergrowth of more then one polytype which complicates an assignment by diffraction techniques. An intergrowth

in nanoscale causes order/disorder phenomena which also hinder a clear description of the structure. These rare minerals are often too small in size for single crystal diffraction which is needed to obtain a detailed solution of the structure. For this reason we wanted to find a way to use the simple and fast method of X-ray powder diffraction to describe the structural characteristics of crystalline material obtained by synthesis without limitations by crystal size or time consuming Rietveld analysis of the patterns. The method was proofed based on natural samples of xonotlite and will be explained in chapter 2.

Coming back to tobermorite, here the composite layers of one calcium and two silicate layers are bound together by an interlayer containing calcium ions and water molecules. The grade of hydration affects the basal spacing of the structure in [001]. Based on that three members are known from the tobermorite group 0.9nm tobermorite or riversideite, the 1.13nm tobermorite or tobermorite senso stricto (part of this study) and the 1.4nm tobermorite also named as plombierite. Tobermorite 1.4nm transforms into the 1.13nm one by heating to 100°C, further heating up to 300°C leads to the 0.9nm tobermorite. by proceeding dehydration (Merlino et al. 2001). it is known from some 1.13 nm tobermorites to not shrink on dehydration and are therefore called “anomalous (Mitsuda & Taylor 1978). The average structure was described by Hamid but the real structure was solved by Merlino et al. (2001, 1999) which is based on two polytypic modification of orthorhombic and monoclinic symmetry leading to a disordered structure (O/D character). In AAC, 1.13nm tobermorite is close to the composition $Ca_5Si_6O_{16}$ $(OH)_2$ $*4H_2O$ and occurs in association with semi-crystalline CSH-phases CSH (I) and CSH (II) as minor components. In contrast to tobermorite these phases are highly disordered and display a wide range of compositions.

Chapter 2: Crystal Chemistry of Xonotlite $Ca_6Si_6O_{17}(OH)_2$. Part I: Determination of Polytypes using X-Ray Powder Diffraction

2.1. Introduction:

As already mentioned in chapter 1 1.13nm tobermorite is formed metastable under the normally conditions during production of AAC. The thermodynamically stable phase is xonotlite (fig 1.7). Xonotlite differs from 1.13nm tobermorite by its structure and texture. While tobermorite forms lathlike crystals which influence the pressure resistance of the product in a positive way due to the interlocking “house of card” structure, xonotlite crystallizes more needle-like what extensively decreases the pressure resistance. Despite this knowledge just a few data exist on the reaction kinetics and mechanisms present during the formation of 1.13nm tobermorite in AAC. There is a strong need of collecting kinetic data to understand and control the processes during the hydrothermal curing of AAC, which are the major aim of this work and will be discussed in detail in chapter 4.

The determination of reaction and growth kinetics of CSH-phases and the calculation of thermodynamic equilibrium demands material well characterized by its crystal chemistry. Single crystal diffraction would be the most exact method to determine the structure of CSH-phases but is often not applicable due to the lack of single crystals of sufficient size. Beyond that one has to deal with short range order effects due to the order disorder behaviour of many CSH-phases and the presence of one ore more polytypes intergrown in one crystal. Applying the Rietveld method on data obtained by synchrotron or neutron diffraction is often time consuming and reaches the limits if more then two polytypes occur in the same crystal. Therefore another aim of the present work was to find a fast and easy method to distinguish between different

polytypes by x-ray powder diffraction, which would be suitable for fine grained crystals as well. In the presented paper this method was tested on different natural polytypes. Based on the work of Hejny and Armbruster deriving structural data for the different polytypes present in xonotlite by single crystal x-ray diffraction, the theoretical powder diffraction patterns were calculated. The polytypes of natural xonotlites were determined by matching the measured patterns with the model patterns Characteristic peaks of lower intensities were chosen in the range of 10 and 35° 2Θ to distinguish between the different polytypes. Ten natural xonotlite samples from seven different localities and different lithologies were investigated. After determining the present polytypes a correlation to the conditions of formation was done.

2.2. Structure and polytypism of xonotlite

Mamedov & Belov (1955, 1956) were the first to propose a structure model for xonotlite which was later confirmed by Eberhard et al. (1981). The structure of xonotlite consists of Ca-O-polyhedral layers in both sevenfold and octahedral coordination and $[Si_6O_{17}]$-*Dreier-Doppelketten.* The CaO polyhedras are edge-sharing to form infinite chains in b-direction and joined together resulting in layers parallel to (001). Between these layers the $[Si_6O_{17}]$-*Dreier-Doppelketten* are located. Each of these double chains consists of two wollastonite-like *Dreier-Einfachketten* with two paired tetrahedra and one bridging tetrahedron (Fig.: 1.8). The structural units were confirmed by extended X-ray absorption fine structure (EXAFS) investigations of Ca (Lequeux et al., 1999) and by ^{29}Si NMR (Cong et al., 1996; Noma et al., 1998) on synthetic material, respectively.

Due to the same length of $[Si_6O_{17}]$-*Dreier-Doppelketten* and two Ca-polyhedra there exist two different ways of attachment of the double chains to the polyhedral layers and hence various polytypes are possible (Gard, 1966; Kudoh & Takeuchi, 1979). Based on the structure model of Mamedov & Belov (1955, 1956a) and the confirmation of Eberhart et al (1981) six different polytypes (four ordered and two one-dimensional disordered) were suggested for xonotlite. These Polytypes can be seen as different stacking in [100]- and [001]-direction of a protoxonotlite-cell introduced by Kudoh & Takeushi (1979). In [100]-direction a continuous shift of **+b/4 or –b/4** or an alternating shift of **+b/4 and –b/4** is possible. In [001]-direction the protoxonotlite-cells are either in juxtaposed positions or shifted by **b/2**. The combination of these different stacking modes leads to four ordered polytypes

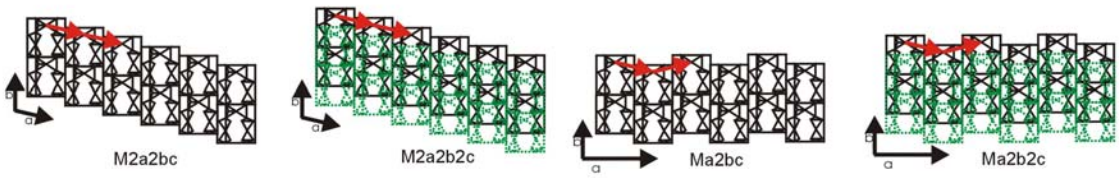

Fig 2.1: polytypes of xonotlite

M2a2bc, M2a2b2c, Ma2bc and Ma2b2c as shown in Figure 2.1. The letter M indicates the monoclinic symmetry of the protoxonotlite-cell and the three lower case letters, with numerical values in front if necessary, indicate the periodicity of the three directions in space according to the modified Gard-notation (Guinier et al., 1984). The different cell parameters were determined by Hejny & Armbruster (2001)

For M2a2bc and M2a2b2c twinning is possible if one species displays intergrowth of domains with continuous shift of **+b/4** in a-direction and continuous shift of **–b/4**. Streaks parallel to a* observed in single crystal patterns by Gard (1966) were assigned to the two known disordered polytypes P∞21 and A∞22 (Corresponding to Ma_d2bc and Ma_d2b2c in modified Gard-notation). Hejny & Armbruster (2001)

extended the group of possible polytypes by $Ma2bc_d$ and $M2a2bc_d$, which have one-dimensional disorder in c-direction as indicated by streaks observed parallel to c* (Chisholm, 1980; Eberhard et al.,1981). Short spikes recorded perpendicular to the c* streaks have been interpreted in terms of two-dimensional disorder (Dornberger-Schiff, 1964), and they are termed with the corresponding symbol Ma_d2bc_d (Hejny & Armbruster, 2001).

2.3. Assigned polytypes

X-ray powder diffraction (XRPD) data were determined with a STOE STADI P-diffractometer using a SIEMENS KRISTALLOFLEX 710/710H generator operating at the following conditions: 40 kV, beam current 30mA, curved Germanium monochromator, step scan in the 2Θ region 10-60° with 0,01 2Θ steps and Cu-Ka-radiation (l=1.5406 Å). Most of the xonotlites show intergrowth of two or three different polytypes. As the characteristic peaks are of very low intensity sometimes not all are detectable in the investigated patterns. Due to occurring texture effects some peaks have highly increased and others decreased intensities. Some of the characteristic peaks can coincide with those of other polytypes (if present in the same sample). For this reason different peaks had to be used for polytype assignment in the different samples. The reproducibility of the obtained results was verified by means of random sampling.

In all samples the M2a2b2c polytype was found but in Xon2, Xon8 and Xon9 with only minor amounts. This predominance is an effect of specific growth conditions availing the development of one polytype. Hejny and Armbruster (2001) explain this preferred development by the more balanced and therefore favourable distribution of OH-groups at the free apices of each Ca-octahedron in the structure of this polytype.

The Ma2b2c-polytype could be detected in two samples found in Russian rodingites of Bazhenovskoe (Xon1) and Chukotka (Xon3) and in two samples found in Mn-ore deposits from the Wessels Mine located in the Kalahari Manganese Field of South Africa (Xon8) and from Franklin, New Jersey (Xon9), respectively.

Ma2bc is developed in the xonotlite from Mäntijärvi (Finland) with an exceptionally high amount and in the well crystalline sample from N'Chwaning Mine (Xon4) investigated by Hejny & Armbruster (2001). In addition this polytype does exist with minor amounts in xonotlites of Bazhenovskoe (Xon1) and Chukotka (Xon3).

The occurrence of M2a2b2c and Ma2bc in Xon4 is in good agreement with the investigations of Hejny & Armbruster (2001) on xonotlites from the same locality. They also reported the presence of Ma2b2c polytype which could not be confirmed in this study. This can be explained by different intergrown polytypes even in samples from the same locality due to small scale fluctuations in the physico-chemical conditions during formation.

The M2a2bc-polytype was first detected in natural xonotlite from Chukotka (Russia) by Garbev (2004) using Rietveld-modelling of diffraction data obtained by syncrotron radiation. In this study the M2a2bc polytype could clearly be detected in xonotlites from Mäntijärvi (Xon2) and Chukotka (Xon3). Esteban et al. (2003) made their assignment in Xonotlites from Carratraca (Spain) by use of X-ray powder diffraction, too. Due to the missing description of the occurrence of M2a2bc polytype in natural xonotlites in literature, this polytype was not taken into account by Esteban et al.(2003). This is in contrast to the results of this study where the development of M2a2bc polytype in xonotlite from Carratraca (Xon5) could be confirmed by the presence of three characteristic reflections.

The above mentioned lower intensity of (h0l)-reflections in all patterns can be explained by a preferred orientation of the acicular crystals along their elongated b-

axes during preparation. The observed phenomenon of inverse intensity-ratio in (0kl) and (hkl)-reflections in M2a2bc-polytype may be caused by preferred orientation of more disk-shaped crystals.

2.4. Correlation of chemical composition and assigned polytypes

Quantitative chemical data for xonotlites were obtained by electron microprobe analysis (EMPA) using a CAMECA SX100 operated at 15 keV acceleration voltage and 20 nA beam current. Synthetic wollastonite (Ca,Si), periclase (Mg), corundum (Al), hematite (Fe), escolaite (Cr), natural ilmenite (Mn,Ti), albite (Na) and osumilite (K) were used as standards and matrix correction was performed by the PAP procedure (Pouchou & Pichoir, 1984). The reproducibility of standard analyses was <1% for each element routinely analysed. For a detailed description of the chemical composition of all investigated xonotlite samples the reader is referred to the appended article (appendix B).

Due to the different lithologies of the localities the investigated samples were divided into three different groups. Xonotlites formed in kimberlites (1), xonotlites in rodingites (2) and xonotlites formed by metasomatic processes close to Mn- and Mn-Zn- ore-deposits (3), respectively. Group 1 is only represented by the xonotlite from Mäntijärvi (Finland). This sample exhibits a low SiO_2- and CaO-content and a slight enhancement of Na_2O up to 0.09 wt%.

Group 2-xonotlites were formed in rodingites (Xon1, Xon3, Xon5, Xon6) and are characterized by the highest CaO-amount of 47.07 up to 47.59 wt%. Analyses of Carratraca-xonotlites (Xon5) are in good agreement to those of acicular crystals replacing hydrogrossular of the same locality published by Esteban et al. (2003)

Samples belonging to group 3 are formed by hydrothermal alteration (250-400ºC) of the primary sedimentary and low-grade metamorphic Mn-ores (Kalahari Manganese Field ; Xon4, Xon8) or high-grade metamorphic Mn-Zn-ores (Franklin, New Jersey; Xon9) and showing slightly higher Mn-content. This could be explained by a preferred integration of Mn on the Ca-positions in Xonotlite-structure, likewise indicated by a lower Ca-content. A substitution of Al for Si on tetrahedral-sites, indicated by the higher amount of Al_2O_3 could be detected noticeably only in the sample from Carratraca and one from Wessels mine. De Bruiyn et al. (1999) described a higher SiO_2- and CaO-content in xonotlites of N'Chwaning Mine in comparison to those of Wessels Mine, which could be confirmed in this investigation. In addition De Bruiyn et al. (1999) detected slightly higher FeO-contents which could not be verified in the samples of this study. In all investigated xonotlites Al, Na and Mn are the only elements which are enriched in remarkable amounts. A enhancement of Mg known from synthetic xonotlites (Quian et al., 1997) could not be detected in the investigated natural xonotlites

2.5. Conclusion:

A clear coherence of different lithology of the habitat and the developed polytype could not be confirmed. Xon2 from kimberlites (Mäntijärvi, Finland) is in a special position referring to this question. It displays a very high amount of Ma2bc polytype compared to all other investigated samples. This can be linked to the special growth conditions in kimberlites.

The results of this study clearly demonstrate that X-ray powder diffraction is a useful and fast method to distinguish the different polytypes developed in xonotlite. It is the preferable option if crystallite size is too small for X-ray single crystal diffraction as it is typical for natural and synthetic xonotlites

Chapter 3: HAND - An Hydrothermal Autoclave for Neutron Diffraction

3.1. Introduction:

As described in chapter 1 1.13nm tobermorite is formed during the hydrothermal curing of AAC. To optimize the reaction conditions and control the formation of phases the exact determination of thermodynamic data and the kinetics of the reaction are needed. Most commonly hydrothermal reactions and their evolving phases at a certain temperature and pressure are studied by performing experiments using so called Parr-bombs. Initial materials and water are filled in the bomb and kept under the desired temperature for a certain amount of time. Subsequently the bomb is quenched with water and the products are investigated by the usual methods. This method reaches the limit when it comes to the determination of reaction kinetics. The scientist has to struggle with several problems. First of all, quenching effects can influence the final phase relations in particular and there is no guarantee to freeze the process exactly at one stage and to quench it without change. Furthermore a huge number of experiments at different compositions and temperatures are needed to obtain a sufficient amount of data-points which means an enormous expenditure of time. Reliable kinetic data can only be obtained by performing in-situ experiments by x-ray or neutron diffraction. For those experiments special reaction cells are needed tailored to the particular requirements of the scientific problem and of course the instrument, respectively. Therefore an autoclave was designed to perform neutron diffraction experiments on the formation of 1.13nm tobermorite.

3.2. Design of HAND

The hydrothermal autoclave for neutron diffraction (HAND) was designed to be a simple and cheap reaction cell fitting to the well-established ILL D20 (Walton and O'Hare, 2000; Hansen et al., 2008) station with its vanadium furnace. For a detailed description of the instrument the reader is referred to the appended article (appendix C) Changes of samples and apparatus must be possible fast and easy. Therefore the apparatus is mainly an upright steel tube closed at both ends. The steam necessary for the hydrothermal reaction is generated inside this tube during heating, so no separate steam supply is needed. The material chosen for the autoclave is cobalt-free stainless steal (4301, Linster, Aschau). The thickness of the walls is a compromise between the demands of a stability at an internal pressure of up to 40 bars and the aim to obtain a maximum penetration of the neutron beam. The schematic diagram of the reaction cell is given in Figure 3.1.

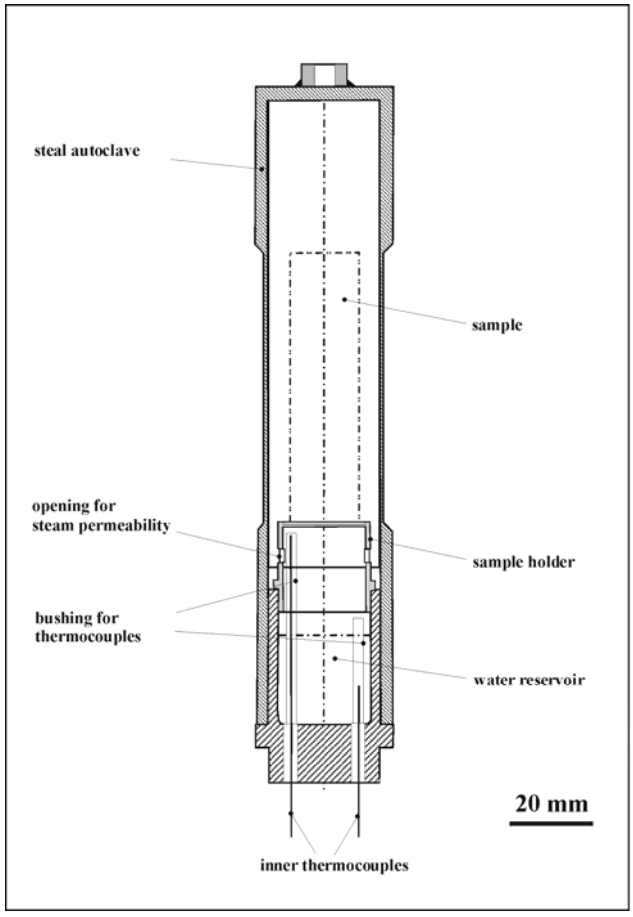

Fig.3.1: schematic drawing of HAND

HAND consist of three parts: bottom, sample support and cover (Fig.3.1.). The bottom is fixed inside the vanadium furnace device below the neutron beam. It serves as reservoir for D_2O and contains the bushings for the internal thermocouples. Inside the bottom the sample support is placed above the water reservoir. The cover is a

tube of 14 cm in length and 2.5cm in diameter which is closed at the upper end. It is simply screwed upon the bottom and can easily be replaced. Its walls have a narrowing down to 1 mm at the level of the neutron beam to maximize the intensity of the neutron flow through the sample.

3.3. Applicability for neutron diffraction experiments

To proof the applicability of HAND the pure system $CaO\text{-}SiO_2\text{-}D_2O$ was chosen to be studied first. The fast and easy sample preparation allows it to easily add different additives to the system. The bulk composition was set to a Ca/Si ratio of 0.5 projecting on the join tobermorite-quartz and a chosen D_2O/solids ratio of 0.8 resembles the recipes of industrially manufactured steam cured building materials [Fehr & Zuern, 2000].

Until now HAND was used for several beam times at ILL to perform experiments to investigate the influence of temperature, quartz grain size and Al-content on the formation of 1.13nm tobermorite. The results for these experiments are summarized and interpreted in chapter 4 and related articles (appendix D and E). The monitoring of the inner and outer thermocouple reveals an accuracy in sample temperature of ± 0.5°C and the desired reaction temperature of 190° was reached

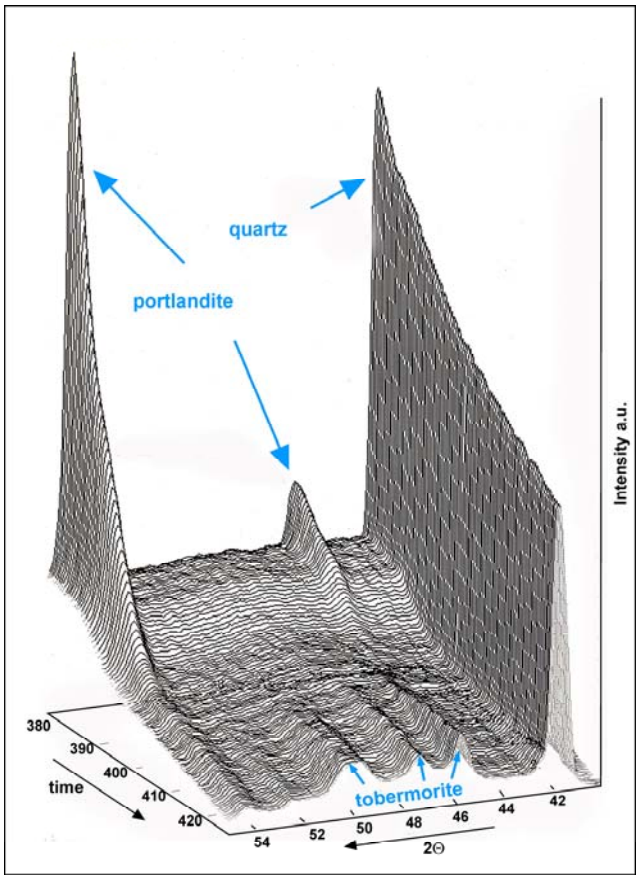

Fig.3.2: time resolved diffraction patterns of an experiment at 190°C and 16µm quartz grain size (modified after Zuern, Fehr & Hansen, 2002)

after 60 min of heating up. The expense of the initial solid phases quartz and portlandite with reaction time and the formation of 1.13nm tobermorite can be observed by the decrease of their Bragg-peaks in the time-resolved neutron diffraction pattern as demonstrated in Figure 3.2. within the range of 40° to 55° 2-Θ.

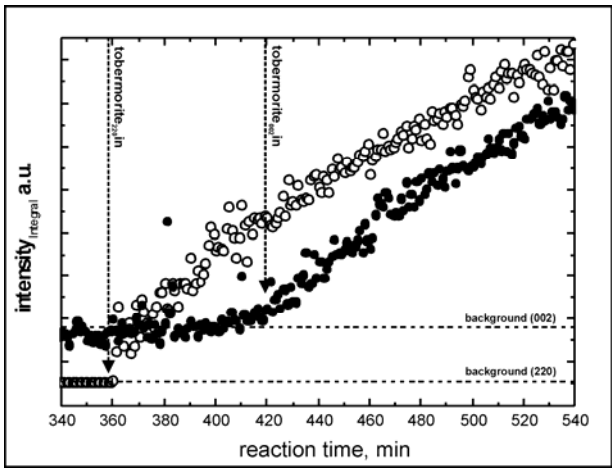

Fig.3.3: different onset of hk0 and 00l reflections of 1.13nm tobermorit during crystallisation

Sequential fitting of multiple, individual Bragg-peaks of every powder pattern were performed by a procedure programmed to perform this task from inside the 'Large Array Manipulation Program' (LAMP, *http://wwwold.ill.fr/data_treat/lamp/lamp.html*), the data-visualization and treatment system used at ILL. The main diffraction peak of iron (mantle of HAND) did not interfere with any peaks of the phases of the sample and was used to calibrate the intensities of the phases of interest. After 200 min. portlandite was dissolved completely, but crystallization of 1.13nm tobermorite did not start until 331 min. at 190°C (Fig.3.2.). The amount of quartz did not remain constant after the consumption of complete portlandite, indicating a reaction of quartz and initially formed semi-crystalline Ca-rich C-S-H(I). The first detectable reflections of tobermorite were those of (hk0) planes, (00l) reflections follow with a time lag of about 60 minutes (see fig. 3.3).

3.4. Conclusion

The high flux instrument D20 enables a time resolution of one minute for recording one diffraction pattern with a good peak/background ratio. Each single diffractogram allows an exact determination of the amount of phases and the decrease or increase

of phases as a function of time. The low scattering of the data on the amount of phases involved indicates, that a detailed kinetic modeling (e.g. using the model of Chan *et al*. (1978) or an Avrami-equation (Shaw et al., 2000) is possible on data obtained by HAND experiments. The steel used for HAND has the advantage to behave chemically inert and derived kinetic data correspond to the pure system SiO_2-CaO-D_2O. Furthermore, steel is a cheap material and easy to handle in contradiction to gold-coated Ti-Zr alloys used by Walton et al (1999).

The detailed compilation of information obtained by HAND-experiments leads to a better insight in the reaction kinetics and mechanisms of CSH-formation. Its applicability has been proofed in a variety of experiments studying the influence of different parameters on the reaction kinetics of 1.13nm tobermorite as will be shown in the next chapter. Beyond that, this autoclave offers a multitude of other possible applications in geo.- and material sciences. The mature design of HAND allows an easy adaptation on powder diffraction devices of other neutron sources assumed that they can provide a sufficient neutron flux.

Chapter 4: reaction and growth kinetics of 1.13nm tobermorite crystallizing in AAC

4.1. Introduction:

1.13nm tobermorite ($Ca_5Si_6O_{16}$ $(OH)_2$ $*4H_2O$) is known to be formed during the hydrothermal hardening of aerated autoclaved concrete (AAC), a widely-used building material for light weight constructions. In consequence of the rapid increase in applications of such materials during the last 10 years a strong need of more detailed scientific research arose simultaneously. Fundamental knowledge on the nature of CSH-phases had been given by Taylor (1964) with his studies on portland cement phases but there is still a demand of further investigations. The existence of various poorly ordered and metastable phases in the CSH-system hinder experimental work thus the thermodynamics, kinetics and structural features of 1.13nm tobermorite and its neighbours are still poorly understood. The knowledge of these properties is of essential importance as the mechanical properties of the mentioned building materials are strongly dependent from the type, amount and texture of the evolving CSH-phases. In AAC, 1.13nm tobermorite is close to the composition $Ca_5Si_6O_{16}$ $(OH)_2$ $*4H_2O$ and occurs in association with semi-crystalline CSH-phases CSH (I) and CSH (II) as minor components. In contrast to tobermorite these phases are highly disordered and display a wide range of compositions. They are classified by their Ca:Si ratio: CSH (I) with a Ca:Si ratio <1.5 and CSH (II) with a Ca:Si ratio > 1.5 according to Taylor (1950,1968). There has been a lot of work in this field aimed at understanding the formation mechanisms and growth kinetics of CSH-phases (Chan & Mitsuda., 1978; Klimesch & Ray,2002). But little quantitative data exist on the kinetics of 1.13 nm tobermorite formation. In addition there is no accordance on the nature of the reaction mechanism because some studies

proposed being solution controlled and others being diffusion controlled as pointed out in detail by Klimesch et al. (1996). The reaction mechanism and kinetics of the formation of 1.13 nm tobermorite in the pure cement-free system $CaO\text{-}SiO_2\text{-}H_2O$ from lime, silica and water under hydrothermal conditions were determined by quenching experiments at 180°-190°C/Psat (Taylor,1968; Chan et al. ,1978; Zürn & Fehr, 2000) and by an in-situ Neutron diffraction experiment (Fehr et al., 2002) as well. As mentioned in chapter 3, quenching experiments reveal the disadvantage of missing data for the early evolution of phases in time and have prevented a quantitative kinetic description so far.

The major aim of this study was to determine the influence of reaction temperature and quartz grain size on the formation of 1.13nm tobermorite in terms of reaction mechanism and reaction rate. Therefore the reaction mechanism was determined from in situ- neutron diffraction experiments and reaction constants were calculated for the pure system $CaO\text{-}SiO_2\text{-}D_2O$ at different temperatures (170,190,210°C, P_{sat}) and the employment of two different grain sizes of the quartz component with 16 and 8 µm, respectively.

The time-resolved neutron diffraction pattern were taken within the range of 8° to 153.6° 2-θ at λ = 2.4 Å to allow the analysis of d-spacing up to 11.3 Å, where the basal (002) reflection of the evolving 1.13nm tobermorite is expected. The mechanisms of the 1.13nm tobermorite forming reaction can be evaluated on the basis of the reaction conversion of quartz according to Chan et al (1978) assuming that there are no seeds in the reactants and the growth rate is low:

$$1-(1-\alpha)^{\frac{1}{3}} = kt^{1/n} \qquad (1)$$

where α gives the fractional reaction conversion of quartz, k the reaction constant and t the reaction time. According to equation (1) the factor n reveals information on

the reaction mechanism. If n=1 the reaction is solution controlled (phase boundary model), if n=2 the reaction is diffusion controlled (Jander equation),(Hancock & Sharp, 1972). Values for α were calculated from the decreasing integral intensity of the (101)-Bragg reflection of quartz. Rate constants for the overall reaction progress were calculated using equation (1) assuming slopes of 1 (n = 1) and 0.5 (n = 2) for a solution and diffusion controlled reaction mechanism, respectively. Based on the calculated rate constants for the three temperatures a first attempt to determine activation energies was done. Therefore activation energies E_A can be determined according to the Arrhenius equation (2) when data were plotted according to equation as follows

$$k = A \cdot e^{-\frac{E_A}{RT}} \quad (2)$$

where k is the rate constant, E_A the activation energy, T the temperature in Kelvin, R the gas constant and A the pre-exponential factor.

4.2. Results

The results for the neutron diffraction experiments are described and discussed in detail in the related articles (see appendix D and E). At this point, only the main findings will be mentioned. After determining the reaction conversion of quartz for all experiments and plotting the results terms of equation (1) as explained in the introduction, a change in slope can be seen. This could now lead to the conclusion that the chosen kinetic model of Chan et. al. (1978) is not valid for the investigated reaction but if one survey the single segments of each curve they are either described with a slope of 1 or 0.5 referring to an exponent of n= 1 or n= 2 in equation (1), respectively. Interpreting this in terms of the reaction mechanism it implies changing reaction mechanisms with the reaction progress. All experiments show a

change from a solution controlled mechanism to a diffusion controlled mechanism. In some of them a third segment could be assigned with a further solution controlled reaction mechanism. 1.13nm tobermorite is not formed directly, it is just found after the complete expense of portlandite. By determining the Ca/Si ratio of the evolving phases over the reaction progress one can see that the phases formed first are richer in Ca then expected for 1.13nm tobermorite. The Ca/Si ratio first reaches a maximum of 1.4 and then converges to the theoretical value of 1.13nm tobermorite of 0.83 This was first detected by our workgroup from neutron diffraction experiments in 2002 (Fehr et al., 2002). The initial step of the reaction is controlled by the solution of quartz and its reaction with portlandite, leading to the formation of a layer of semi crystalline CSH-phases surrounding the quartz grains as shown in Figure 4.1 for AAC steam cured at 190°C/P_{sat}(Zürn,1997). The second part of the reaction is controlled by the diffusion of SiO_2 through this layer of CSH-phases, portlandite is expensed completely and the Ca/Si ratio decreases. 1.13nm tobermorite is then formed by the reaction of quartz with the previously formed CSH-phases.

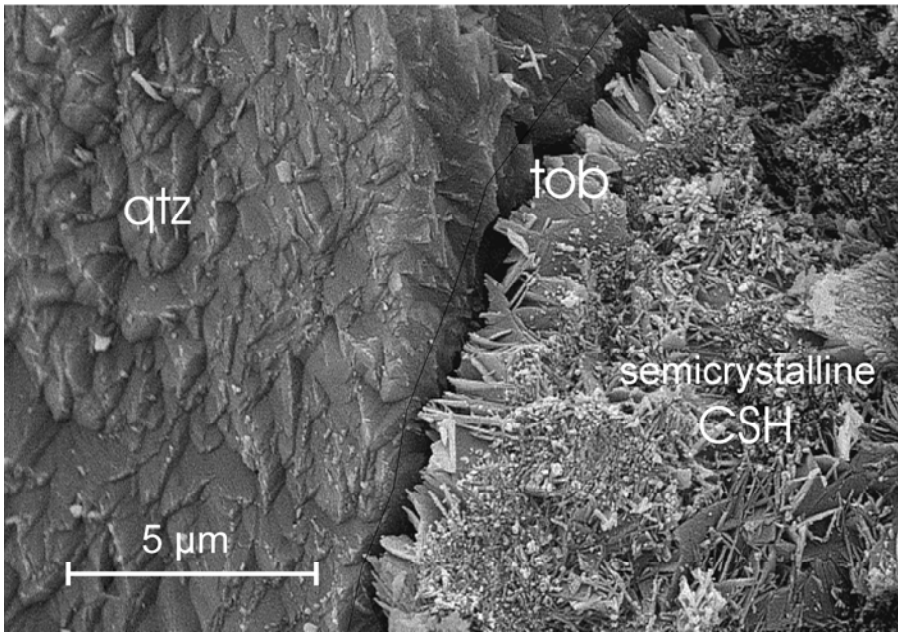

Fig.4.1:electron optical picture of a quartzgrain surrounded by a rim of freshly formed 1.13nm tobermorite and semicrystaline CSH-phases (Zürn,1997)

Comparing the transition times, the point of portlandite expense and the first occurrence of 1.13nm tobermorite-reflections the strong influence of temperature and grain size of quartz becomes apparent (Fig.4.2).

4.3. Influence of temperature and grain size of quartz

On the first glance, the use of finer quartz generally accelerates the reaction, portlandite is expensed earlier and also 1.13 tobermorite crystallizes faster. This is expected as a change in grain size from 16 to 8µm increases the specific surface

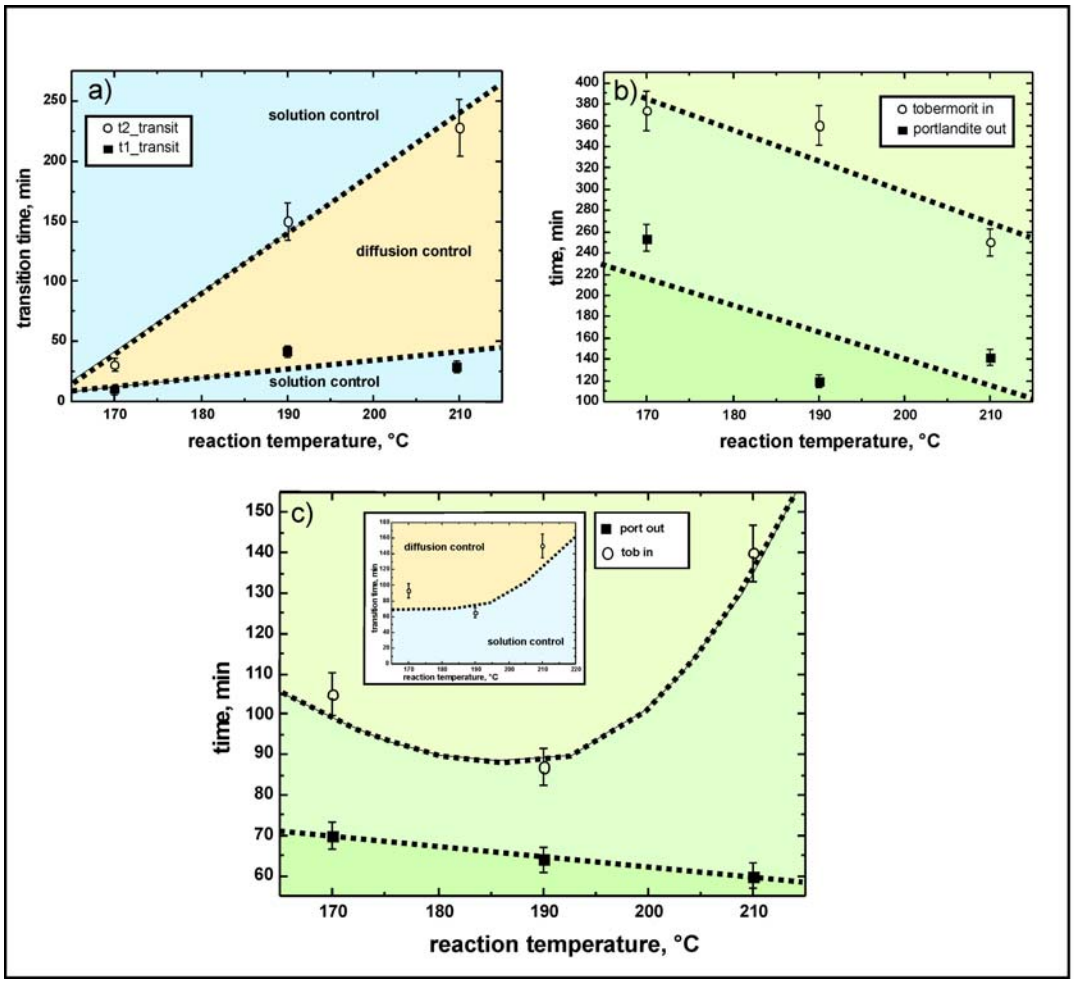

Fig. 4.2: changing transition time with reaction temperature and points of expense of portlandite and occurrence of 1.13nm tobermorite determined from experiments with 16µm quartz (a and b) and 8µm quartz (c)

about 44% resulting in a higher reactive area. But an increase in specific surface do

not only accelerate the reaction, it also has a strong influence on the present reaction mechanisms as well, demonstrated by the missing second diffusion controlled segment in the experiments at 170 and 190°C/P_{sat} applying the 8µm quartz.

Applying 16µm quartz all experiments show a second change back to a solution controlled segment. With increasing reaction temperature the length of the diffusion controlled segment increases but the time for portlandite out and tobermorite in decreases. Initial semicrystalline CSH starts to react earlier with quartz to form 1.13 tobermorite indicated by the longer persistence of a diffusion controlled mechanism.

Experiments with 8µm quartz show a differing behaviour. For 170 and 190°C the second change to a solution controlled mechanism is missing or not detectable. Only at 210°C this change is present. But again the transition time from solution to diffusion control decreases with increasing reaction temperature. The point of portlandite expense slightly decreases with rising temperature. For 170 and 190° this is also valid for the point of tobermorite occurrence but at 210°C the time increases again, due to the present second change in reaction mechanism. This behaviour was assigned to the clear metastable formation of 1.13nm tobermorite under these conditions (Zürn & Fehr, 2000).

4.4 Quenching experiments

Based on this study kinetic data obtained from quenching experiments were recalculated in terms of equation (1) and can be now interpreted by applying two different slopes (n=1 and n=2) due to two distinct mechanisms during the reaction progress. Literature values (Klimesh & Ray, 2002; Zürn & Fehr 1997) were used to determine the transition temperatures (see appendix D, Fig.3) and interpreted concerning to the grain size dependency (see appendix D, Fig.4) The results are in

good agreement with findings of this study, showing an increase of reaction time with increasing grain size of quartz

4.5. Calculated rate constants and activation energies

The influence of both grain size and reaction temperature can as well be seen in the calculated rate constants and activation energies

The change of the rate constants with increasing specific surface for the three investigated reaction temperatures clearly shows an increase at a given temperature. The strongest increase occurs at 210°C, the rate constant changes from $2.795*10^{-4}$ s^{-1} to $3.214*10^{-4}$ s^{-1} for the first solution controlled part and from $2.784*10^{-4}$ s^{-1} to $2.794*10^{-4}$ s^{-1} for the diffusion controlled part with a decreasing grain size of quartz. Likewise the rate constant increases with increasing temperature what can be extracted from Figure 4.3. Based on the calculated rate constants for the three temperatures a first attempt to determine activation energies was done. The determined activation energies for the experiments containing the 16µm quartz are with 0.2 kJ/mol for the solution controlled segment and 1.8 kJ/mol for the diffusion controlled segment. They reveal values which were remarkably lower than those determined from the 8µm quartz

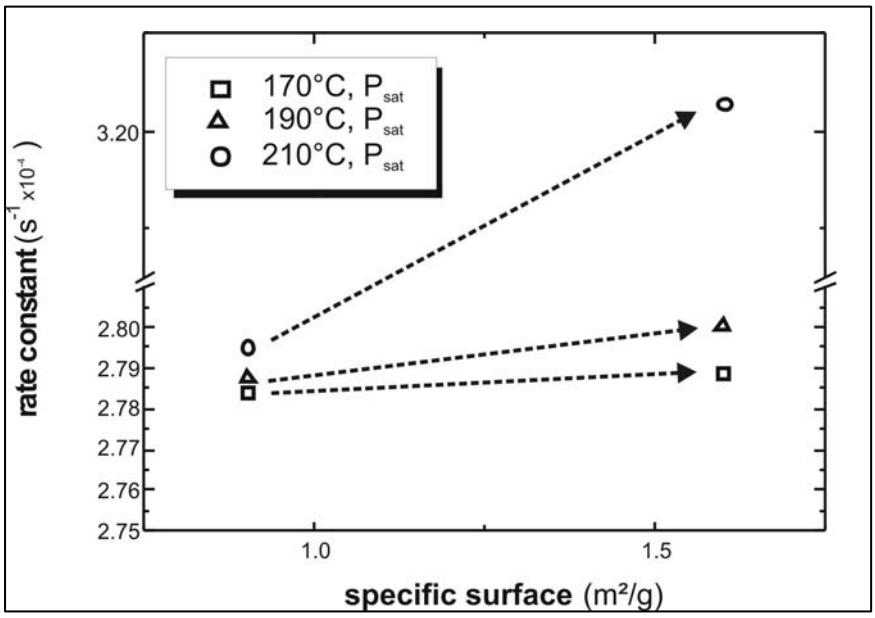

Fig.4.3: changing rate constant with increasing specific surface (decreasing grain size of quartz)

experiments of 6.2 kJ/mol and 7.4 kJ/mol, respectively. These values are considerably below 26 kJ/mol, 37 kJ/mol and 33kJ/mol determined for the system CaO-Al_2O_3-SiO_2-H_2O assuming an isokinetic behaviour (Shaw et al., 2000).

4.6. Conclusion

It could be shown that in-situ neutron diffraction is a very suitable method to investigate the kinetics of the 1.13nm tobermorite formation. The non isokinetic behaviour of the reaction could be evidenced by combining the high intensity of the D20 powder diffractometer at ILL together with an improved hydrothermal autoclave (manuscript 2) allowing constant reaction conditions and a fast and easy sample exchange. Furthermore exact times for the transition and the consumption of portlandite and the occurrence of 1.13nm tobermorite could be determined. Based on the data obtained by applying the kinetic model of Chan et al. (1978) on the values for the overall reaction progress rate constants could be determined for the first time. Likewise Shaw et al. calculated rate constants for the Tobermorite forming reaction but did not interpret their date in terms of the present reaction mechanism. By conducting experiments at three different temperatures, the temperature dependence and hence activation energies could be determined. The results of this study yield detailed kinetic data on the 1.13nm tobermorite formation, which were just insufficient investigated in the past. These data give a better understanding of the processes present during the production of AAC and could help to optimize production conditions and recipes resulting in shorter production times and an optimal exploit of the available resources.

5.1.Outlook

The presented work successfully studied the reaction kinetics of the 1.13nm Tobermorite formation in the system SiO_2-CaO-H_2O. But answering one question leads to several new ones, that is how science works. Future work should therefore focus on the influence of additives like Al, SO_4 and K to the reaction kinetics. They can enter the production process by the natural sand minerals like feldspar and mica. High temperature long term experiments could give insights in the decomposition of 1.13nm tobermorite to xonotlite and quartz.

The possibility to use porous samples for neutron diffraction experiments would improve the comparability to the production of AAC but is difficult to implement so far.

The pattern matching method to characterise the material in terms of polytism like done for natural xonotlite in the presented work should be assigned to neutron diffraction experiments as well. At the same time more analytical methods should be used for the characterisation. First attempts with FTIR and Raman yield promising result but need further work.

5.2.References:

ALEXANDERSON, A **(1979)**: *Relations between Structure and Mechanical Properties of Autoclaved Aerated Concrete*. Cem. Concr. Res. **9**(4),. 507-514

AYLSWORTH, J.W. AND DYER, F. A. **(1914)**: US Patent 1.087.098

E. BONACCORSI', S. MERLINO, A. R. KAMPF **(2005)**: *The crystal structure of Tobermorite 14Å, a CSH-Phase*. – J. of Am. Ceram. Soc., **88** (3),505-512

DE BRUIYN, H.; SCHOCH, A.E.; VAN DER WESTHUIZEN, W.A & BEUKES, G.J. **(1999)**: *The chemical composition of xonotlite and associated inesite from the Nchwaning and Wessels mines, Kalahari manganese field, South Africa.* N.Jb.Miner.Mh., **5**: 212-222

CHAN, F., MITSUDA, T. **(1978)**: *Formation of 11 Å tobermorite from mixtures of lime and colloidal silica with quartz, Cem.Concr.Res*. **8** 135-138.

CHAN, C.F.,SAKIYAMA, M.; MITSUDA, T. **(1978)**, *Kinetics of CaO-Quartz-H_2O reaction at 120°C in suspension*. - *Cem. Con. Res*. **8,** 1-6.

CHISHOLM, J.E. **(1980)**: *Polytism in xonotlite, $Ca_6Si_6O_{17}(OH)_2$*. - *In* Electron Microscopy and Analysis,. Inst. Phys. Conf. Ser., **52**, 109-112

CONG, X. & KIRKPATRICK, R.J. **(1996)**: *^{29}Si and ^{17}O NMR Investigation of the Structure of Some Crystalline Calcium Silicate Hydrates*. - Advn. Cem. Bas. Mat., **3**, 133-143

DORNBERGER-SCHIFF K. **(1964)**:*Grundzüge einer Theorie von OD-Strukturen aus Schichten*. - Abhandl. d. Deutsch. Akad. d. Wiss. zu Berlin. Klasse f. Chemie, Geol. u. Biol*.,* **3**, 1–107

DUBRAL, W. **(1992)**: *On production and application of AAC worldwide*. – Advances in Autoclaved Aerated Concrete, Wittmann (ed.), 3-9

EBERHART; E.; HAMID, S. & RÖTTGER, B. **(1981)**: *Strukturverfeinerung und Polytypie von Xonotlite*, - Z. Krist., **154**, 271-272

ERIKSSON, J. A. **(1924)**: DRP 447 194 of 12.6.1924

ESTEBAN, J.J.; CUEVAS, J. & TUBIA, J.M. **(2003)**: *Xonotlite in rodingite assemblages from the Ronda peridotite Betic Cordilleras, Southern Spain.* –Can. Mineral., **41**: 161-170

FEHR, K-T.; HUBER, M.; ZUERN, S.G.; HANSEN, T. *Proc. 5th ICSTR* (2002) 37-40

FEHR, K.T. AND ZUERN, S.G. **(1997)**: *Phase relations of 1.13 nm tobermorite, xonotlite, truscottite and gyrolite under hydrothermal conditions*, - in Proc. 5th Int. Symp. Hydrotherm. Reactions, 225-227.

GABROVSEK, R., KURBUS B., MUELLER D. AND W. WIEKER **(1993)** "Tobermorite formation in the system CaO, C3S-SiO2-Al2O3-NaOH-H2O under hydrothermal conditions," Cem. Con. Res. **23,** 321.

GARBEV, K. (2004): *Struktur, Eigenschaften und quantitative Rietveldanalyse von hydrothermal kristallisierten Calciumsilikathydraten (CSH-phasen)*,Thesis, University of Karlsruhe

GUINIER , A.; BOKIJ, G.B.; BOLL-DORNBERGER, K.; COWLEY, J.M.; DUROVIC, S.; JAGODSINSKI, H.; KRISHNA, P.; DEWOLFF, P.M.; ZVYAGIN, B.B.; COX, D.E.; GOODMAN, P.; HAHN, TH.; KUCHITSU, K. & ABRAHAMS, S.C. **(1984)**: *Nomenclature of Polytype Structures - Report of the International Union of Crystallography Ad.Hoc Committee on the Nomenclature of Disordered, Modulated and Polytype Structures*. - Acta Cryst, **A40**: 399-404

HAMID S.A. **(1981)**: *The crystal structure of the 11Å natural tobermorite $Ca_{2.25}[Si_3O_{7.5}(OH)_{1.5}]. 1H_2O$*. - Z. Kristallogr. **154** 189–198.

HANCOCK AND J.H. SHARP **(1972)**: *Method of Comparing Solid-State Kinetic Data and Its Application to the Decomposition of Kaolinite, Brucite, and $BaCO_3$*, J. Amer.Ceram.Soc. **55**, 74-77.

HANSEN, T.C.; HENRY, P.F.,FISCHER, H.E. (**2008**): *The D20 instrument at the ILL: a versatile high-intensity two-axis neutron diffractometer*. - Measurement Science & Technology.

HEJNY,C. & ARMBRUSTER, T. **(2001)**: *Polytypism in Xonotlite $Ca_6Si_6O_{17}(OH)_2$*. - Z.Kristallogr., **216**: 396-408

HOMAN, M. **(2008)**: *Porenbeton Handbuch- planen und bauen mit System*,Bundesverband Porenbeton, **6. Auflage**, Bauerverlag, Gütersloh

KALOUSEK , G.L.; NELSON, E.B **(1978)** : *Hydrothermal reactions of dicalcium silicate and silica*. - Cem. Concr. Res. **8**(3), 283-289

KLIMESCH D. S.; RAY A.; SLOANE B. **(1996)**: *Autoclaved cement-quartz pastes: The effects on chemical and physical properties when using ground quartz with different surface areas .1. Quartz of wide particle size distribution*. - Cem.Concr.Res. **26**, 1399-1408.

KLIMESCH D. S., RAY A. **(2002)**: *Effects of silica reactivity on the nature and formation of Al-1.1nm tobermorite*. - J.Therm.Anal.Calorim., 995-1003

KUDOH, Y. & TAKEUSHI, Y. **(1979)**: *Polytypism of xonotlite: (I) Structure of an A1 polytype.* - Min.Journal, **9**, 349-373

LEQUEUX, N., MORAU, A.; PHILIPPOT, S. & BOCH, P. **(1999)**: *Extended X-ray Absorbtion Fine Structure Investigation of Calcim Silicate Hydrates*. – J. Am. Ceram. Soc., **82** (5), 1299-1306

MAMEDOV,KH. & BELOV, N.V. **(1955)**: *Crystal structure of xonotlite*. – Dokl.Akad.Nauk SSSR, **104**: 615-618

MAMEDOV, KH. & BELOV, N.V. (**1956**): *Crystal structure of the mineral group wollastonite. 1 structure of xonotlite*. - Zapiskii Vsesoyuz. Miner. Obshchest, **85**: 13-38

MERLINO S., BONACCORSI, E. AND. ARMBRUSTER. T. **(1999)**: *Tobermorites: Their real structure and order-disorder (OD) character*, Amer.Miner. **84**, 1613-1621

MERLINO S., BONACCORSI E. AND ARMBRUSTER TH. (2001): *The real structure of tobermorite 11 angstrom: normal and anomalous forms, OD character and polytypic modifications*. - Eur. J.Min., **13**, 577-590

MICHAELIS, W. **(1881)**: DRP 14195 vom 2.6.

NOMA, H. ADACHI, Y.; MITSUDA, Y. & YOKOYAMA, T. **(1998)**: *^{29}Si and ^{1}H NMR of Natural and Synthetic Xonotlite*. - Chemistry Letters, 219-220

POUCHOU, J.L. & PICHOIR, F. **(1984)**: A new model fro quantitative X-ray microanalysis Part I: application to the analysis of homogenious samples. -La Recherche Aérospatiale, **3**: 13-38

QUIAN, G.; XU, G.; LI, H. & LI, A. **(1997)**: *Mg-Xonolite and its coexisting phases*. –Cem. Concr. Res., **27** (3), 315-320

SHAW, S., CLARK S. M. **(2000)**: *Hydrothermal formation of the calcium silicate hydrates, tobermorite ($Ca_5Si_6O_{16}(OH)_2$* $4H_2O$) and xonotlite ($Ca_6Si_6O_{17}(OH)_2$): an in situ synchrotron study*. - Chemical Geology **167**(1-2) 129-140.

SHAW, S. HENDERSON, C.M.B. & KOMANSCHEK, B.U. **(2000)**: *Dehydration/recrystallization mechanism , energetics, and kinetics of hydrated calcium silicate minerals: an in situ TGA/DSC and synchrotron radiation SAXS/WAXS study*. - Chemical Geology, **167**: 141-159

TAYLOR, H.F.W **(1950)**: *Hydrated calcium silicates. Part I. Compound formation at ordinary temperatures*. - J. Chem. Soc. **30**, 3682.

TAYLOR, H.F.W *Proc. Vth Int. Symp. Chem. Cem*. **Vol II** (1968) 1-26

TAYLOR, H.F.W. (1964): The calcium silicate hydrates. *in* 'The Chemistry of Cements' H.F.W. Taylor, Ed., *Academic Press, London*, 167–232.

WALTON, R.I. AND O'HARE, D. **(2000)**, *Watching solids crystallise using in situ powder diffraction*. - Chem. Commun. **23,** 2283 – 2291.

WALTON, R.I., FRANCIS, R.J., HALASYAMANI, P.S., O'HARE, D., SMITH, R.I., DONE, R. AND HUMPHREYS, R.J. (**1999**): *Novel apparatus for the in situ study of hydrothermal crystallizations using time-resolved neutron diffraction*, - Rev. Sci. Instr. **70**, 3391.

ZERNIKOW **(1877)**: *DRP 502* of 2.7.1877, Odenberg

ZUERN, S.G. AND FEHR, K.T. **(2000)**: *Phase relations and thermodynamic properties of 1.13 nm tobermorite and xonotlite.* in Proc. 6th Int. Symp. Hydrotherm. Reactions, 286-289.

ZUERN, S.G., FEHR, K.T. AND HANSEN, T. **(2002)**: *Determination of the reaction kinetics and reaction mechanisms of 1.13nm tobermorite by means of in-situ neutron diffraction*. in Proc Vth ICSTR, East Brunswich, 37-40

ZUERN, S.G. **(1997)**: *Einfluss der Sandminerale auf die Bildung von Calciumsilikathydraten (CSH-Phasen), das Gefüge und die mechanischen Eigenschaften von Porenbeton,* Inauguraldissertation, Logos-Verlag Berlin

5.3 Appendix

Appendix A

Report of the industrial internship at Xella Thermopierre, Bourgoin- Jallieu, France (unpublished)

Praktikumsbericht

Indusrtiepraktikum 13.09.-06.10.2006
YTONG/ Xella Thermopierre
St Savin (Bourgoin-Jallieu)

Herstellung von Porenbeton

Abb.1: Verwendung von Porenbeton

Zur Produktion von Porenbeton wird eine Mischung aus Branntkalk, Quarzsand und Zement verwendet. Die Sandfraktion wird fein gemahlen um die Kristallisation zu begünstigen. Im Werk von St Savin sollen in Zukunft 2 Sande verwendet mit unterschiedlichen Quarzgehalten. Der eine wird in der Nähe des Werks aus einem See gefördert und ist Quarzärmer der andere stammt aus Bedoin mit SiO_2 – Gehalten um die 93 %. Ein höherer Quarzgehalt wirkt sich positiv auf die Druckfestigkeit aus.
Das beim Zuschneiden der Kuchen anfallende Material wird als sogenanntes Rückgut dem Produktionsprozess wieder zugeführt. Für ein besseres Ansteifen der Masse wird zusätzlich noch Anhydrit ($CaSO_4$) beigemengt. Die Rohstoffe werden in den gewünschten Anteilen vermischt und mit Wasser zu einer Mörtelmischung angemacht in der der Kristallisationsprozess beginnt. Erst kurz vor dem Gießen wird fein gemahlenes Aluminiumpulver (2 Korngrößen) zugegeben das mit der alkalischen Mörtelmischung unter Bildung von Wasserstoff reagiert. Dadurch kommt es zur Porenbildung und zum Aufschäumen der ansteifenden Masse.
Die Formen (4x1x0.8m) werden bis zu ca. 2/3 mit der fertigen Masse befüllt und ruhen anschließend bei ca 37°C für 115 min in Kammern. Nach ca. 50 Minuten ist der „Kuchen“ bis zum Rand der Formen aufgegangen. Nach dem Ansteifen werden die Formen um 90° gedreht und der grünfeste Kuchen wird auf einen Wagen umgelagert. Anschließend erfolgt das Zuschneiden der Blöcke auf das gewünschte Maß mit Hilfe von Drähten. Am Ende des Produktionsprozesses steht die

Autoklavierung. Hier werden die Kuchen bei ca. 190°C und einem Sättigungsdampfdruck von 10-12 bar für 8-12 Stunden hydrothermal gehärtet.
Das fertige Produkt, YTONG® (SIPOREX®), zeichnet sich bei relativ geringer Dichte durch hohe Wärmedämmung (geringe Wärmeleitfähigkeit) und ausreichender Drückfestigkeit aus und findet im Hausbau auch aufgrund der einfachen Verarbeitung (geringes Eigengewicht und leicht zu schneiden) Anwendung.
Die Wärmeleitfähigkeit und die Druckfestigkeit des Materials sind von der Rohdicht, dem Quarzgehalt, der Feinheit des Sandes und der Menge an Bindemittel abhängig und werden im Werk täglich kontrolliert.

Kontrolle und Optimierung von Wärmeleitfähigkeit, Druckfestigkeit und Korngröße der Sandfraktion

Zur Optimierung dieser beiden Größen werden Versuchsgießungen mit bestimmten Gehalten an Bindemittel, Mischungsverhältnissen der beiden Sande und definierter Rohdichte hergestellt. Pro Gießung werden zwei Blöcke entnommen und aus ihnen drei Prüfwürfel mit 10 cm Kantenlänge herausgesägt. Die Richtung des entweichenden Wasserstoffs, die Nummer und der Tag der Gießung werden auf den Blöcken vermerkt (Abb.2). Anschließend werden die Würfel von 4 Seiten geschliffen um eine glatte Oberfläche zu erhalten die für die Messungen nötig ist. Die Würfel werden dann im Trockenschrank bei ca. 80°C getrocknet und vor den Messungen eine Nacht lang im Exikator gelagert um die Restfeuchte zu beseitigen.

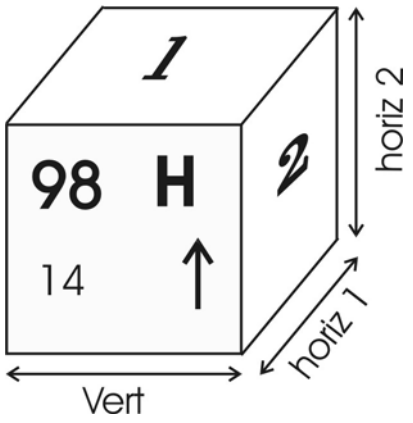

Abb.2: Prüfwürfel mit Beschriftung, Flächen zur Messung von λ (1) und A (2) und Angaben über Abmessungen

.

<u>Messung der Wärmeleitfähigkeit:</u>

Die Wärmeleitfähigkeit λ gibt an welche Wärmemenge Q in der Zeit t und bei einem Temperaturunterschied dT durch die Fläche A strömt. Die Prüfwürfel werden in der Reihenfolge B (bas) M (millieu) H (haut) in einem Exikator gestapelt. Der Wert für λ wird einmal zwischen den Würfeln B und M und einmal zwischen M und H auf der in Abb.2 mit 1 gekennzeichneten Fläche (vert × horiz 1) mittels einer Sonde gemessen. Bei der letzten Messung werden die Steine zusätzlich mit einem Gewicht beschwert. Aus dem Unterschied zwischen der vorgegebenen Temperatur und der in den

Steinen gemessenen Temperatur berechnet das Gerät den wert für λ in W/min*K. Die am in St Savin vorhandenen Messgerät ermittelten Werte werden anschließend korrigiert anhand einer Eichkurve die aus Messungen an einem genormten Gerät in Paris ermittelt wurde.

2.2 Prüfung der Druckfestigkeit:

Die Druckfestigkeit des Materials wird an der Fläche Nr 2 in Abb.2 gemessen. Es wird dabei die auf den Prüfquerschnitt (horiz1 × horiz2 siehe Abb2) wirkende Kraft ermittelt wen es zum Bruch kommt.
Die Druckfestigkeit des Materials steigt im Allgemeinen mit zunehmender Rohdichte (abnehmende Porosität). Um Gießungen unterschiedlicher Rohdichte miteinander vergleichen zu können muss noch auf diese normiert werden. Zur Ermittlung der Rohdichte werden zusätzlich Gewicht und Kantenlänge des Prüfkörpers gemessen. Der auf die Rohdichte normierte Wert wird als A-Zahl angegeben.

$$\text{A-Zahl} = \frac{\mathbf{Rc}}{\text{const.} \cdot \rho^2}$$

Rc : Druckfestigkeit in MPa/dm²
ρ : Rohdichte, trocken in kg/dm³
const: 62500000

Korngrößenbestimmung mittels Laser – Granulometrie

Eine weitere Größe die Einfluss auf die Eigenschaften des Porenbetons hat ist die Mahlfeinheit (Korngröße) der Sandfraktion. Hier gilt je feiner der Sand gemahlen ist desto besser verläuft die Kristallisation und desto höher ist die Druckfestigkeit des Produkts.
Es wurden zwei verschiedene Feinheiten des Sandes aus St Savin verwendet. Zum einen eine Mischung mit fein gemahlenem Sand aus St Savin wie er bisher auch in der normalen Produktion verwendet wurde. Zum anderen eine Mischung mit gröber gemahlenem Sand aus St Savin.
Die Korngröße des Sandes wird mit der Methode der Laser-Granulometrie bestimmt.
Die Korngrößenbestimmung mittels Laser-Granulometrie ist eine Methode, die die Projektionsfläche der Teilchen anhand der Beugung des Laserstrahls an den Teilchenrändern ermittelt. Über die Fläche wird auf das Volumen der Teilchen geschlossen. Bei der Berechnung der Volumenanteile einer bestimmten Korngröße wird davon ausgegangen das die Teilchen annähernd kugelförmig sind.

Aufgaben und Ziele des Praktikums

Während meines Praktikums wurden mehrere Versuchsgießungen produziert die ich dann hinsichtlich Wärmeleitfähigkeit und Druckfestigkeit untersuchen sollte. Dazu habe ich, wie unter 2. beschrieben, Prüfwürfel aus den Blöcken gesägt, diese anschließend geschliffen und für 5 Tage im Trockenschrank bei ca. 80°C gelagert.
Nach der Trocknung habe ich die Werte für die Wärmeleitfähigkeit und die Druckfestigkeit an den dafür vorgesehenen Messgeräten (siehe Punkt 2) ermittelt.

Ziel dieser Untersuchungen war es neue Rezepturen mit Verwendung des SiO_2 reichen Sandes zu testen und somit die Werte für Wärmeleitfähigkeit, Druckfestigkeit und auch der Korngröße der Sandfraktion zu optimieren. Hierfür wurden die beiden Sande in verschiedenen Mischungsverhältnissen verwendet. Bisher konnte nur eine Mischung in einem extra Silo hergestellt werden, die dann in allen Gießungen des Tages verwendet wurde. Die Installation eines neuen Programms ermöglicht es jetzt in jeder einzelnen Gießung die Anteile der beiden Sande zu variieren. Dies ist vielleicht für die normale Produktion weniger von Bedeutung, bietet aber für die Versuchsgießungen einen großen Vorteil.
Am Ende des Praktikums soll anhand der in dieser Zeit ermittelten Daten und anhand von Daten aus vorangegangenen Versuchen Optimierungskurven erstellt werden. In diesen werden die ermittelten A-Zahlen und Werte für λ gegen das CaO/SiO_2 – Verhältnis und zusätzlich den prozentualen Anteil an Bindemittel aufgetragen. Die Wärmeleitfähigkeit λ sollten idealer weise einen Wert 0.098 W/k*m nicht überschreiten. Denn je geringer die Wärmeleitfähigkeit umso besser ist die Wärmedämmung des Baumaterials. Für die A-Zahl gilt generell, je größer desto besser, sie sollte am Optimum aber über 1450 liegen. Einfluss auf diese Größen hat die Rohdichte des Materials, der Anteil an Calciumbinder, die Feinheit und der Quarzanteil in der Sandfraktion.

Versuche

Es wurden generell 2 Versuchsansätze verwendet. Zum einen wurden Gießungen produziert in denen, bei konstanten Mischverhältnis der beiden Sande der prozentuale Anteil an Bindemittel (taux de liant) variiert. Im zweiten Ansatz wurden die Mischverhältnisse variiert und der Anteil an Calciumbinder konstant gehalten. Die verwendeten Sandmischungen lagen bei 20, 30, 40, 45, 50,60 und 70% des Sandes aus Bedoin (quarzreich). Die Menge an Calciumbinder variierte zwischen 25 und 35% wobei ein Hauptaugenmerk auf den Bereich zwischen 28 und 30% gelegt wurde. Das CaO/SiO2 Verhältnis wurde im Nachhinein aus den reellen Mengenangaben der verschiedenen Bestandteile berechnet und variiert in beiden Versuchsansätzen.
Die Mischverhältnisse der Sandfraktion sind durch die verschiedenen Farben der Zeilen zu erkennen (siehe Legende)
Um das CaO/SiO2 Verhältnis zu berechnen wurde die chemischen Analysen der Firma Brück vom 25.06. 2006 verwendet
Der Wert für λ und ρ ist der Durchschnitt aus den Werten der bei jeder Gießung hergestellten 3 Prüfwürfeln (H M B).

Ergebnisse und Auswertung

Ohne Rücksicht auf eine Optimierung der Kenngrößen lässt sich zunächst einmal sagen das der Wert für λ mit abnehmender Rohdichte sinkt: Bei sinkender Rohdichte werden aber ebenfalls die werte für die Druckfestigkeit kleiner, was bis zu einem gewissen Grad tolerierbar ist.
Betrachtet man für die einzelnen Sandmischungen die besten erreichten Werte für λ und A so zeigt sich das unabhängig vom Mischungsverhältnis dieses Maximum sich

immer bei ca. 28 % Bindemittel befindet. Dies erscheint zunächst ein wenig seltsam da bei Zunahme des Quarzanteils auch der Anteil an Bindemittel steigen müsste. Erklären lässt sich dies meiner Ansicht nach durch das Verhältnis von CaO zu SiO_2. Dieses sinkt mit zunehmendem Anteil von Quarz bei konstanter Bindemittelmenge (siehe Abb 3).

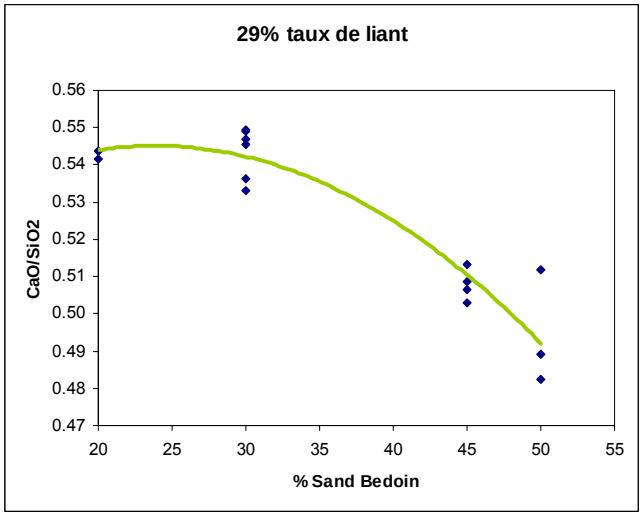

Abb.3: Änderung des CaO/SiO2 Verhältnis mit steigendem Anteil an Sand Bedoin bei konst taux de liant

Für die Maximalwerte heißt das, dass mit zunehmendem Anteil an Quarz im Sand die besten Werte für λ und A mit einem kleineren CaO/SiO_2 Verhältnis zu finden sind. Generell liegen das Maximum für die Quarzreichen Mischungen bei wesentlich höheren Werten als bei den Quarzarmen (Abb.4).

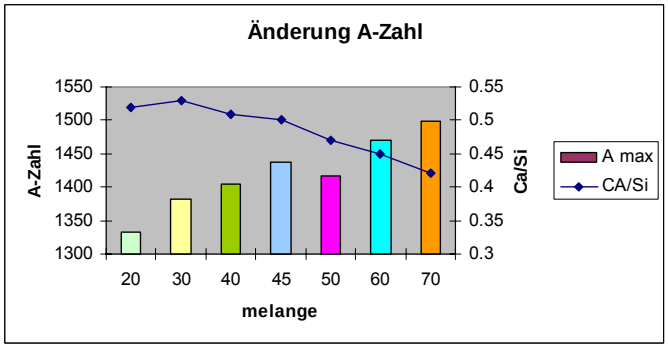

Abb.4: Zunahme der max A-Zahl mit steigendem Quarzanteil

a)

Melange % Sable bedoin	Gießung	Bindemittel %
20	6	26,28,29
30	26	23-33
40	13	26-30
45	7	28,29
50	35	23-35
60	6	26,27,28
70	10	27-31

b)

Melange		Maximal	Fit
			liant
20	A	1350	1333
	liant	26,4	26.2
	Ca/Si	0,52	0.52
30	A	1442	1381
	liant	27	28.1
	Ca/Si	0.51	0.53
40	A	1445	1405
	liant	27.9	27.9
	Ca/Si	0.51	0.51
45	A	1456	1437
	liant	28.9	28.6
	Ca/Si	0.51	0.5
50	A	1559	1416
	liant	26.9	27.7
	Ca/Si	0.46	0.47
60	A	1481	1471
	liant	27.1	27.6
	Ca/Si	0.45	0.45
70	A	1498	1498
	liant	27.1	27.1
	Ca/Si	0.42	0.42

c)

Melange % Sable bedoin	A	Rc	l	r
20	1350	2.64	0.093	350
30	1442	2.9	0.094	354
40	1445	3.29	0.1	377
45	1456	3.09	0.098	364
50	1559	3.47	0.103	373
60	1481	2.98	0.097	355
70	1498	3.04	0.096	356

Tabelle 1

a) Anzahl der Versuchsgießungen mit den verschiedenen Sandmischungen und den abgedeckten Bereich an Bindemittelanteil
b) Maximal ermittelte Werte für A (mit liant und Ca/Si) in den einzelnen Sandmischungen und werte der Maxima aus den Näherungskurven
c) Druckfestigkeit (Rc), Wärmeleitfähigkeit (λ) und Rohdichte (r) der Versuche mit maximaler A-Zahl in den verschiedenen Sandmischungen

Für die Auswertung der Ergebnisse wurden die ermittelten A-Zahlen gegen das CaO/SiO_2 Verhältnis aufgetragen. Um die Optimierungskurve zu erhalten wurden diese Daten mit einem Polynom 2. Ordnung angefittet.
Eine Auswertung hinsichtlich der Änderung von λ mit steigendem CaO/SiO_2 Verhältnis ist aufgrund der stark schwankenden Rohdichte schwierig.
Mit eine hohen Rohdichte nimmt zwar die Druckfestigkeit zu es wird aber auch der Wert für λ zu groß und umgekehrt.
Die Schwankungen in der Rohdichte sind auf unterschiedliches Aufgehen des Kuchens zurückzuführen. Geht der Kuchen stark auf wird in der Produktion viel Material weggeschnitten und der Wert für die Rohdichte wird geringer als der gewünschte.

Mit zunehmendem Quarzanteil im Sand sinkt der Grenzwert für die Rohdichte bei dem noch gute werte für λ erzielt werden.
Das bedeutet bei gleicher Rohdichte ist der Wert für λ besser bei niedrigeren Quarzgehalten der Sandmischung.
Betrachtet man das Maximum der ermittelten Optimierungskurven so wird deutlich das die A-Zahl mit steigendem Quarzgehalt im Sand zunimmt.

Das CaO/SiO2 Verhältnis nimmt jedoch ab
Für 20, 45 und 60 % S-Bedoin wurden keine vollständigen Optimierungskurven ermittelt da nur Werte für einen Ast der Kurve vorliegen und die A-zahlen erst beginnen wieder kleiner zu werden.
Deswegen sind in der Auswertung die Maximal ermittelten Werte berücksichtigt worden. Die maximal und aus den Optimierungskurven ermittelten Werte sind mit den dazugehörigen CaO/SiO_2 und Bindemittelanteil und zusätzlich ρ, λ und Rc für die Maxima aus den Tabellen 1a) und b) zu entnehmen.

20% Bedoin-Sand

Mit einer Mischung mit 20 % S-Bedoin wurde die größte A-Zahl (1350) bei einem Bindemittelanteil von 26.4% und einem CaO/SiO_2 Verhältnis von 0.52 ermittelt. A liegt somit noch deutlich unterhalb der geforderten 1450. Die Rohdichte dieser Gießung beträgt 350 kg/dm³ und λ ist gleich 0.093, beide Werte liegen im optimalen Bereich.

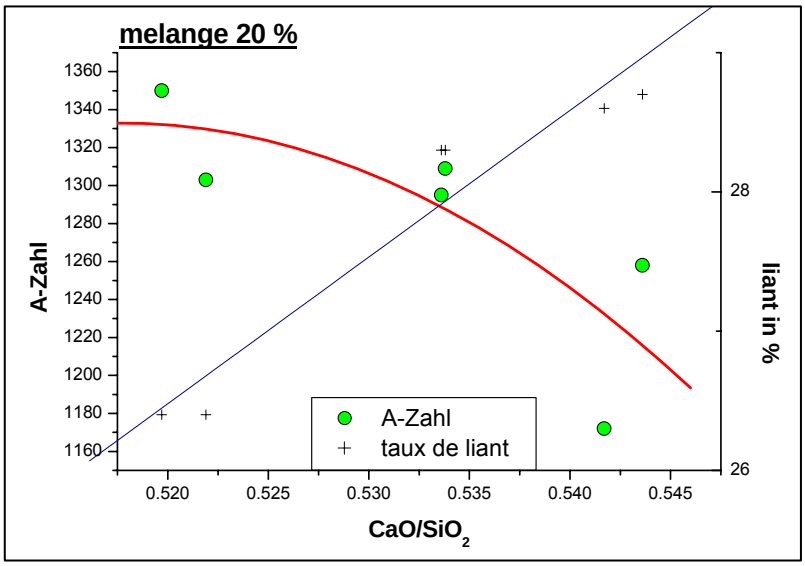

Abb.3: Optimierungskurve für A-Zahl bei 20% Bedoin-Sand

30% Bedoin-Sand

Bei 30%-iger Mischung liegt die aus der Optimierungskurve entnommene A-Zahl bei 1385 mit einem Bindemittelanteil von 27% und einem CaO/SiO_2 von 0.52. Auch der maximal ermittelte Wert liegt mit 1442 noch knapp unter dem Zielwert. Sowie r als auch λ sind mit 354 und 0.094 als gut einzustufen.

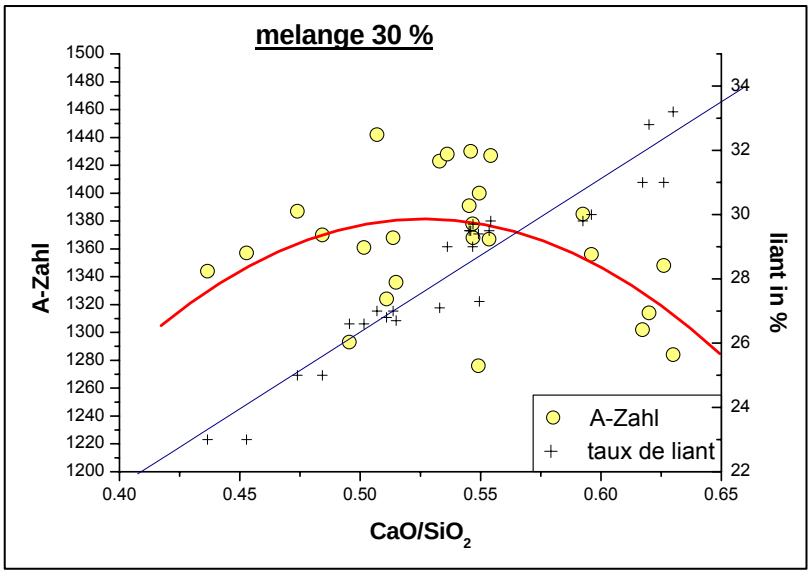

Abb.4: Optimierungskurve für A-Zahl bei 30% Bedoin-Sand

40% Bedoin-Sand

Mit 40% Bedoin-Sand beträgt der Wert aus der Kurve bei 1405 bei einem CaO/SiO_2 von 0.507 und einem Bindemittelanteil von. Der maximal ermittelte Wert liegt bei 1445 mit aufgrund der hohen ρ von 377einem zu großen λ von 0.100, dafür aber mit 3.29 bei einem sehr guten Wert für Rc. Die Rohdichte und somit auch λ sind besser bei geringeren Bindemittelanteilen.

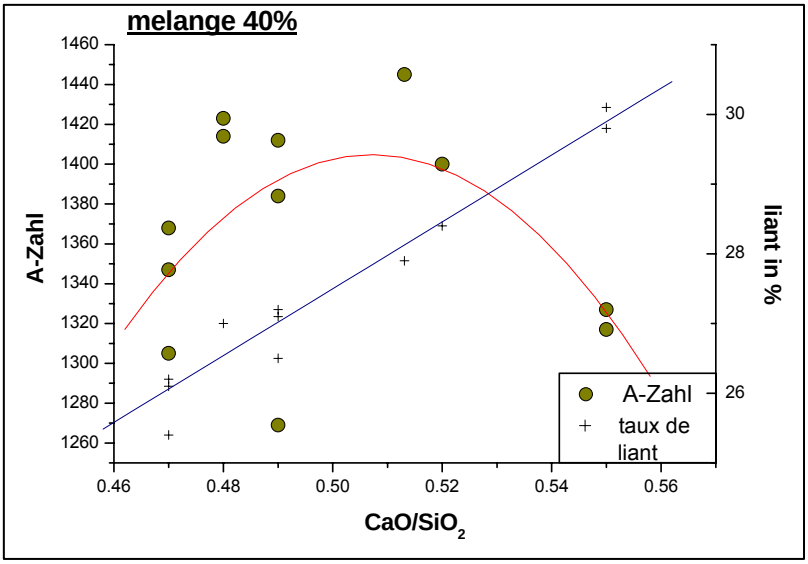

Abb.5: Optimierungskurve für A-Zahl bei 40% S-Bedoin

45 % Bedoin-Sand

Bei 45% liegen sowohl λ als auch Rc im akzeptablen Bereich und auch die A-Zahl übersteigt knapp das Limit von 1450 des zu erzielenden Werts.
Ein anfittten der Werte ist nicht möglich da die Versuche ganz knapp das Maximum erreicht haben und noch nicht genügend Werte für den „absteigenden Ast“ zur Verfügung stehen

50% Bedoin-Sand

Bei 50% Bedoin-Sand beträgt der Höchstwert von A (1416) laut Optimierungskurve bei einem CAO/SiO_2 von 0.47 und einem Bindemittelanteil von 27.7%. Die maximal ermittelte Wert 1559 liegt bei einem CaO/SiO_2 von 0.45 und einem Bindemittelanteil von 26.9 %. Dieser sehr hohe Wert ist auf die ebenfalls hohe ρ zurückzuführen was auch der schlechte Wert für λ von 0.103 bestätigt.

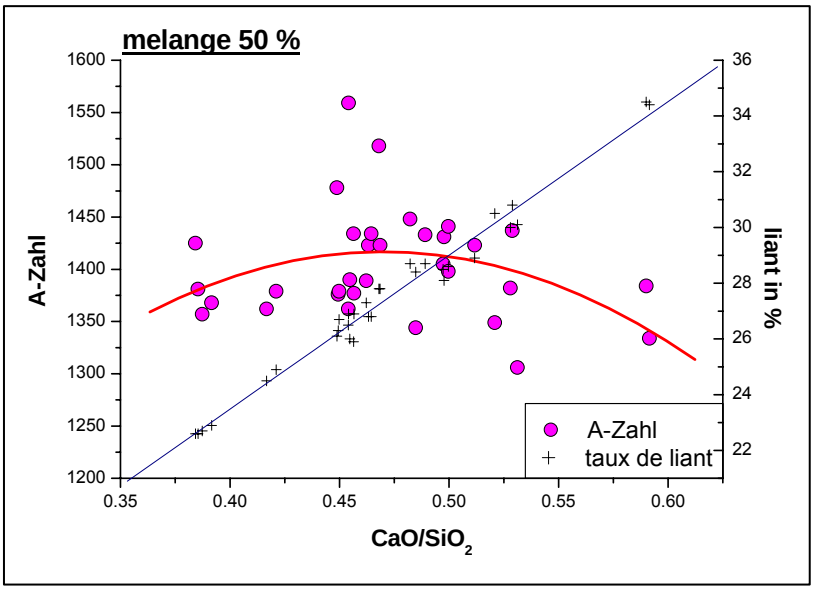

Abb.6: Optimierungskurve für A-Zahl bei 50% S-Bedoin

Sandfeinheit (Lasergranulometrie)

Der Einfluss der verschiedenen Sandfeinheiten wird in Abb. 5 deutlich. Es wurden zwei verschiedene Mahlfeinheiten des Sandes aus St Savin verwendet. In den Mischungen mit dem feinen Sand sind die Korngrößenverteilungen der beiden Sande ungefähr gleich in den anderen ist der Sand aus Bedoin relativ zum Sand aus St Sv feiner. Diese Gießungen mit dem liegen mit ihren A-Zahlen im Durchschnitt um 30 höher als die gleichen Gießungen mit feinerem Sand aus St Savin (siehe Abb.5). Auch hier zeigt sich wieder eine Zunahme der Differenz der A-Zahlen mit steigendem Quarzanteil im Sand Die große Abweichung des Wertes bei 50%-iger Mischung in der Reihe 2 ist auf eine zu hohe Rohdichte zurückzuführen.

Eine größere Feinheit des quarzreichen Sandes begünstigt somit die Kristallisation des Tobermorits und führt zu besseren Werten für die Druckfestigkeit.

INFORMATIONS SUR LE PRODUIT

IDENTIFICATION: bs bed 2
Fichier: ESSAI
Répertoire: C:\SIZERX\DATA\
Commentaires: Pompe = 100 %. Agitation = 100 %.
20 secondes d'ultrasons à 80 %.

N° d'Execution: 12
N° Enregistrement: 14

Mesuré le: Mer 27 Sep 2006 09:35
Analysé le: Mer 27 Sep 2006 09:35
Type de Résultat: Analyse

INFORMATIONS SUR L' INSTRUMENT

Gamme: 300 mm
Presentation: 2OFD
Modèle d'Analyse: Polydisperse
Modifications: Aucune

Longueur Faisceau: 2.40 mm
[Particule R.I. = (1.5295, 0.0100); Dispersant R.I. = 1.3300]

Préparateur: MS17

Obscuration: 9.2 %
Résiduel: 0.355 %

RESULTATS DE LA MESURE

Type de Distribution: Volume
Diametres:
D [4, 3] = 57.17 µm

Concentration = 0.0170 %Vol
D (v, 0.1) = 6.01 µm
D [3, 2] = 15.16 µm

Densité = 1.000 g / cub. cm
D (v, 0.5) = 44.98 µm
Span = 2.574E+00

Specific S.A. = 0.3957 sq. m / g
D (v, 0.9) = 121.80 µm
Uniformité = 8.413E-01

Taille (µm)	Volume Diff %	Taille (µm)	Volume Diff %	Taille (µm)	Volume Diff %	Taille (µm)	Volume Diff %
0.100	0.00	0.269	0.00	0.725	0.01	1.95	0.59
0.110	0.00	0.297	0.00	0.800	0.02	2.15	0.63
0.122	0.00	0.328	0.00	0.883	0.02	2.38	0.65
0.135	0.00	0.362	0.00	0.975	0.02	2.63	0.66
0.149	0.00	0.400	0.00	1.08	0.02	2.90	0.67
0.164	0.00	0.442	0.00	1.19	0.03	3.20	0.68
0.181	0.00	0.488	0.01	1.31	0.22	3.53	0.71
0.200	0.00	0.539	0.00	1.45	0.43	3.90	57.27
0.221	0.00	0.595	0.01	1.60	0.49	63.00	35.37
0.244	0.00	0.656	0.01	1.77	0.53	250.0	
0.269		0.725		1.95			

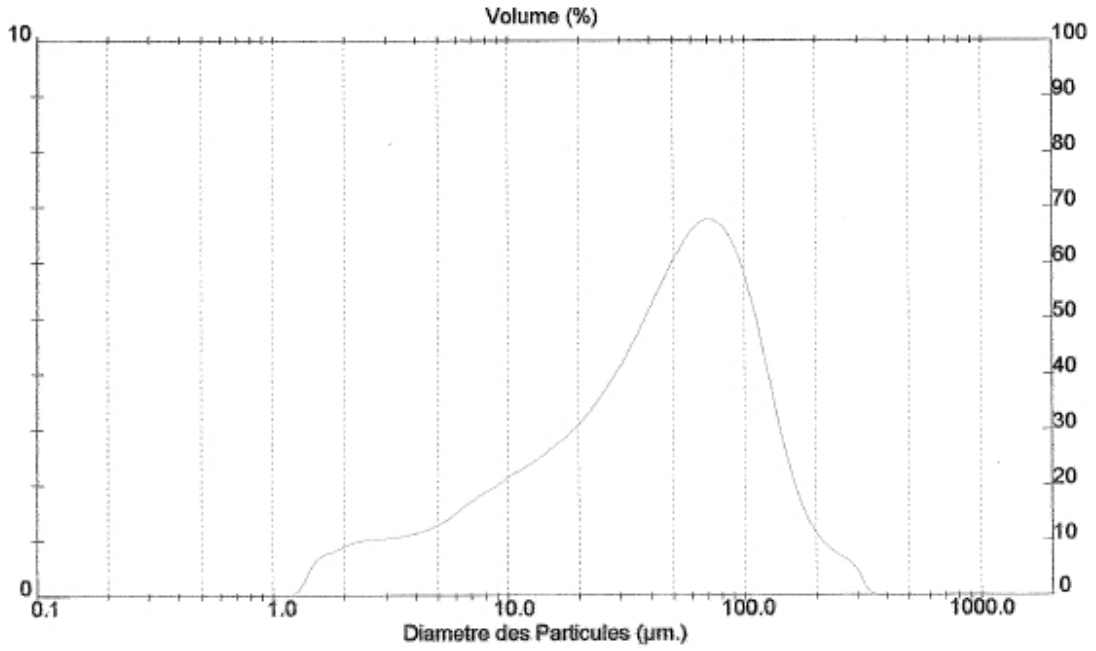

Abb.7: Ergebnisse der Lasergranulometrie fur den Bedoin-Sand

INFORMATIONS SUR LE PRODUIT

IDENTIFICATION: bs sav 2 — N° d'Execution: 9 — Mesuré le: Mer 27 Sep 2006 08:49
Fichier: ESSAI — N° Enregistrement: 11 — Analysé le: Mer 27 Sep 2006 08:49
Répertoire: C:\SIZERX\DATA\ — Type de Résultat: Analyse
Commentaires: Pompe = 100 %. Agitation = 100 %.
20 secondes d'ultrasons à 80 %.

INFORMATIONS SUR L' INSTRUMENT

Gamme: 300 mm — Longueur Faisceau: 2.40 mm — Préparateur: MS17 — Obscuration: 16.7 %
Presentation: 2OFD — [Particule R.I. = (1.5295, 0.0100); Dispersant R.I. = 1.3300]
Modèle d'Analyse: Polydisperse — Résiduel: 0.350 %
Modifications: Aucune

RESULTATS DE LA MESURE

Type de Distribution: Volume — Concentration = 0.0283 %Vol — Densité = 1.000 g / cub. cm — Specific S.A. = 0.4423 sq. m / g
Diametres:
D [4, 3] = 61.18 µm — D [3, 2] = 13.56 µm — Span = 2.927E+00 — Uniformité = 9.481E-01

Taille (µm)	Volume Passant %	Taille (µm)	Volume Passant %	Taille (µm)	Volume Passant %	Taille (µm)	Volume Passant %
0.110	0.00	0.297	0.00	0.800	0.04	2.15	2.95
0.122	0.00	0.328	0.00	0.883	0.06	2.38	3.74
0.135	0.00	0.362	0.00	0.975	0.08	2.63	4.55
0.149	0.00	0.400	0.00	1.08	0.11	2.90	5.38
0.164	0.00	0.442	0.00	1.19	0.14	3.20	6.23
0.181	0.00	0.488	0.00	1.31	0.18	3.53	7.09
0.200	0.00	0.539	0.01	1.45	0.44	3.90	7.98
0.221	0.00	0.595	0.01	1.60	0.97	63.00	61.53
0.244	0.00	0.656	0.02	1.77	1.56	250.0	98.51
0.269	0.00	0.725	0.03	1.95	2.22		

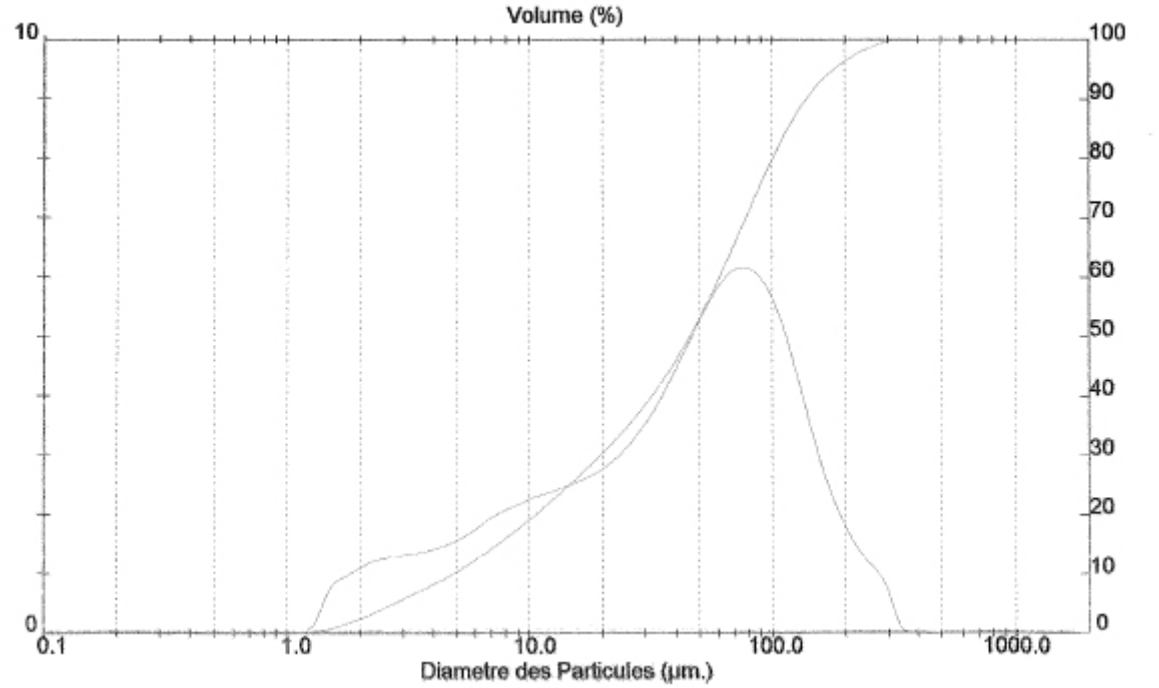

Abb.8: Ergebnisse der Lasergranulometrie für den feinen Savin-Sand (Standard)

INFORMATIONS SUR LE PRODUIT

IDENTIFICATION: bs sav grob2
Fichier: ESSAI
Répertoire: C:\SIZERX\DATA\
Commentaires: Pompe = 100 %. Agitation = 100 %.
20 secondes d'ultrasons à 80 %.

N° d'Execution: 14
N° Enregistrement: 16

Mesuré le: Mer 27 Sep 2006 10:01
Analysé le: Mer 27 Sep 2006 10:01
Type de Résultat: Analyse

INFORMATIONS SUR L' INSTRUMENT

Gamme: 300 mm
Presentation: 2OFD
Modèle d'Analyse: Polydisperse
Modifications: Aucune

Longueur Faisceau: 2.40 mm
[Particule R.I. = (1.5295, 0.0100); Dispersant R.I. = 1.3300]

Préparateur: MS17

Obscuration: 12.6 %
Résiduel: 0.392 %

RESULTATS DE LA MESURE

Type de Distribution: Volume
Diametres:
D [4, 3] = 78.88 µm

Concentration = 0.0236 %Vol
D (v, 0.1) = 5.60 µm
D [3, 2] = 15.45 µm

Densité = 1.000 g / cub. cm
D (v, 0.5) = 57.61 µm
Span = 3.124E+00

Specific S.A. = 0.3884 sq. m / g
D (v, 0.9) = 185.58 µm
Uniformité = 9.744E-01

Taille (µm)	Volume Diff %	Taille (µm)	Volume Diff %	Taille (µm)	Volume Diff %	Taille (µm)	Volume Diff %
0.100	0.00	0.269	0.00	0.725	0.01	1.95	0.65
0.110	0.00	0.297	0.00	0.800	0.02	2.15	0.70
0.122	0.00	0.328	0.00	0.883	0.02	2.38	0.72
0.135	0.00	0.362	0.00	0.975	0.02	2.63	0.73
0.149	0.00	0.400	0.00	1.08	0.03	2.90	0.74
0.164	0.00	0.442	0.00	1.19	0.03	3.20	0.74
0.181	0.00	0.488	0.01	1.31	0.24	3.53	0.75
0.200	0.00	0.539	0.00	1.45	0.47	3.90	46.04
0.221	0.00	0.595	0.01	1.60	0.54	63.00	42.43
0.244	0.00	0.656	0.01	1.77	0.59	250.0	
0.269		0.725		1.95			

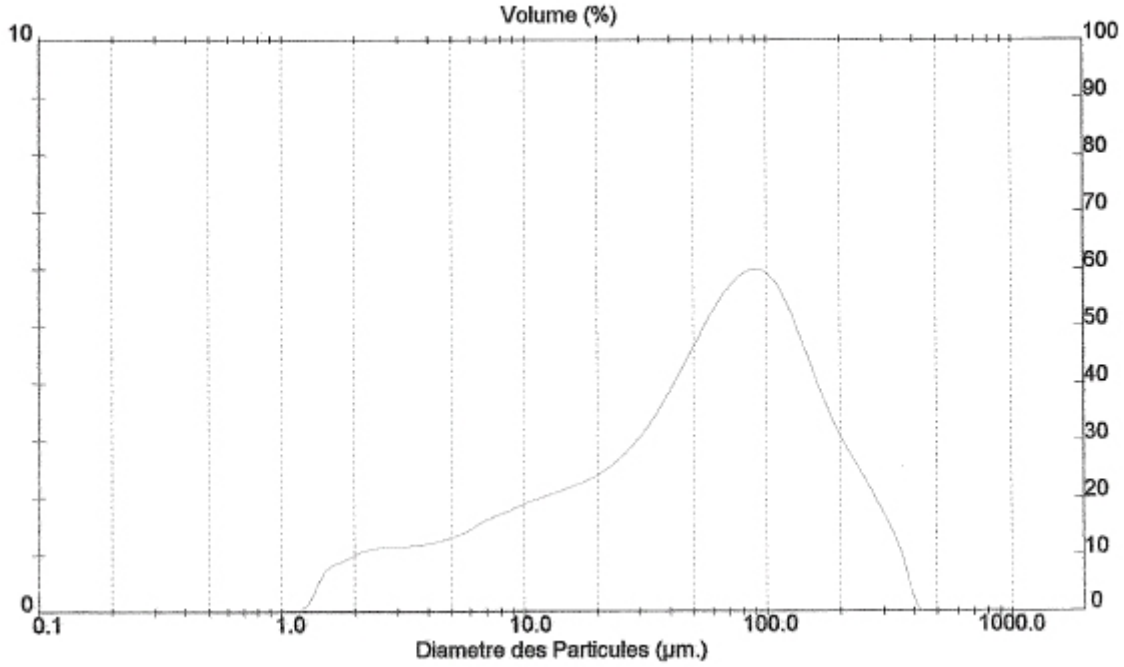

Abb.9: Ergebnisse der Lasergranulometrie für den groben Savin-Sand

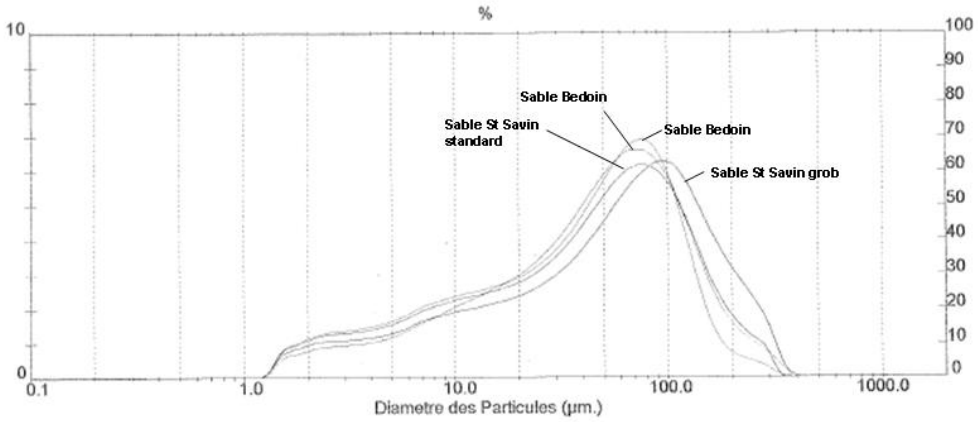

Abb.10: Granulometriekurven der verwendeten Sande

Tabelle 2
Ergebnisse der Lasergranulometrie

Sand	D < 10	D < 50	D < 90
St Savin fein	4.72	43.88	125.97
St Savin grob	5.67	58.10	181.94
Bedoin	6.08	45.34	125.18

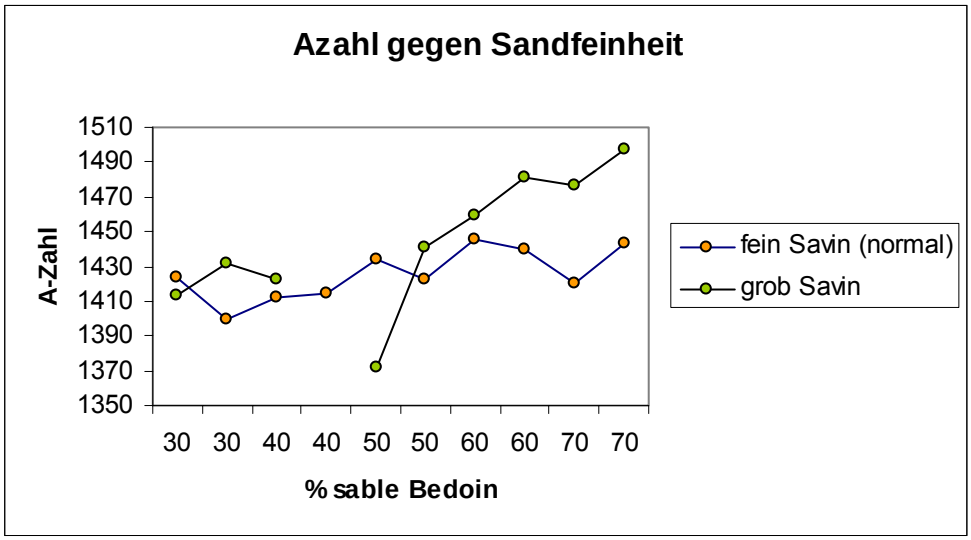

Abb.5: A-Zahl aufgetragen gegen die verschiedenen Sandmischungen mit feinem und gröber gemahlenem Sand aus St Savin

Zusammenfassung

Zusammenfassend ist zu sagen, dass eine sehr gute Optimierung der A-Zahlen fur die Mischung mit 30% Bedoin-Sand leider nicht möglich war. Es konnten nur Maximalwerte von 1380 erreicht werden.
Dieses Maximum erreicht man mit einem Bindemittelanteil von ca. 28% und einem entsprechenden CaO/SiO_2 Verhältnis von 0.53.
Mit quarzreicheren Mischungen können wesentlich bessere Ergebnisse erzielt werden.
Hierbei ist aber auf den Grenzwert der Rohdichte zu achten. Es fällt auf das mit höherem Anteil an BR, Zement und Kalk die Rohdichten oft zu hoch liegen.
Sehr deutlich in den Versuchen mit 50% Bedoin-Sand zu erkennen.
Es sollte daher beim Erstellen der Rezepte darauf geachtet werden diese werte möglichst gering zu halten und Bindemitttelanteil und CaO/SiO_2 über die Gesamtmasse an festem Material zu steuern.
Es reicht anscheinend nicht aus für eine kleinere rohdichte nur die Gesamtmasse an festen material zu verringern.
Weitere Versuche die durchgeführt werden sollten sind meiner Meinung nach auch Gießungen mit 100% Quarzsand. Hierzu können die Rezepte aus Montreau mit leichten Modifikationen übernommen werden. Dort verwendet man für die Rohdichte von 350 ausschließlich 100% Quarzsand da dieser in der werkseigenen Grube zur Verfügung steht.

Rezepte

Tabelle 3

	20	30	40	45	50	60	70
liant	26.3	28.0	28.1	28.5	27.6	27.6	27.1
Ca/Si	0.52	0.53	0.51	0.50	0.47	0.45	0.42
Ms	1940	1930	1940	1930	1940	1940	1940
Ss	1070	1030	1035	1020	1045	1045	1055
BR	280	280	280	280	280	280	280
Cim	360	370	380	380	375	380	375
Chaux	150	170	165	170	160	155	150
Anh	80	80	80	80	80	80	80
Al1	1.75	1.75	1.75	1.75	1.75	1.75	1.75
Al2	0.75	0.75	0.75	0.75	0.75	0.75	0.75

In Tabelle 3 sind die theoretischen Rezepte aufgeführt, die zum erreichen der jeweiligen Maximumswerte verwendet werden sollten.

In Tabelle 4 sind die Rezepte aufgelistet die tatsächlich verwendet wurden für die Gießungen mit den maximalen A-Zahlen.
Die dazugehörigen Nummern und das Datum der Gießung sind ebenfalls aus der Tabelle 4 zu entnehmen.
Diese Rezepte können immer nur Richtwerte sein da sie den Schwankungen der Mischmaschine unterliegen.

Tabelle 4

melange	20	30	40	45	50	60	70
taux de liant	26.4	27.3	27.9	28.9	26.9	27.2	30.2
CaO/SiO2	0.52	0.51	0.51	0.51	0.45	0.45	0.49
Ms	1900	1900	1940	1980	1980	1950	1940
Ss	1037.7	1021	999.2	1026.8	1087.2	1059	975
Br	280	280	320	300	280	280	300
Cim	358.5	367	380.8	413.2	391	371	399
Chaux	143.8	152	160	160	141.8	160	186
Anh	80	80	80	80	80	80	80
Al1	1.75	1.75	1.75	1.7	1.7	1.75	1.75
Al2	0.75	0.75	0.75	0.75	0.75	0.75	0.75
Gießung	64	101	75	78	76	81	59
Datum	19.09.2006	14.09.2006	21.09.2006	24.08.2006	07.09.2006	27.09.2006	29.09.2006

Appendix B

Crystal Chemistry of Xonotlite $Ca_6Si_6O_{17}(OH)_2$. Part I: Determination of Polytypes using X-Ray Powder Diffraction

published in: Neues Jahrbuch für Mienralogie, Vol. 186/2, p 153-162, August 2009

Crystal Chemistry of Xonotlite $Ca_6Si_6O_{17}(OH)_2$. Part I: Determination of Polytypes Using X-Ray Powder Diffraction (XRPD)

Saskia Bernstein, Karl Thomas Fehr, Rupert Hochleitner

Abstract: The crystal chemistry of xonotlite is mainly controlled by its four different polytypes. Ten natural xonotlites from three different lithologies were studied in order to determine their polytypes by powder methods as X-ray powder diffraction (XRPD). The chemical compositions were obtained by electron microprobe analysis (EMPA) and show constant compositions with minor substitutions of Mn and Al. To determine the 4 ordered polytypes known for xonotlite (M2a2b2c, M2a2bc, Ma2b2c, Ma2bc), the theoretical diffraction patterns were calculated based on atom coordinates of Hejny & Armbruster (2001). For each polytype characteristic reflections can be chosen. The assignments were conducted by means of pattern matching. The results reveal that xonotlite mainly occurs in nature as intergrowths of two up to four polytypes. It could be demonstrated that X-ray powder diffraction is a useful and fast method to determine the different polytypes of xonotlite.

Key words: xonotlite, crystal chemistry, polytypism, XRPD, pattern matching

Introduction

The physico-mechanical properties of steam-cured building materials are determined by the type and the structure of the Calcium-Silicate-Hydrates or CSH phases using the notation of cement chemistry for **C**aO, **S**iO_2 and **H**$_2$O, respectively. These binders are formed during the hydrothermal curing at elevated temperatures under saturated steam pressure. They could account for 10 up to 80 weight percent of the solid phases of the product. Depending on the

type of material and hardening temperature 1.13 nm tobermorite or xonotlite are the predominant phases with semi crystalline CSH-phases as minor components. In addition to steam cured building materials like light weight RPC there is a wide range of technical applications of xonotlite ranging from storage of hazardous wastes to insulating material and flame retardants. Xonotlite ($Ca_6Si_6O_{17}(OH)_2$), was described first by Rammelsberg (1866) in contact-metamorphic limestones of Tetela de Xonotla, Mexico and can be found in nature as a vein-forming mineral in many different localities. Xonotlite is formed mainly as a product of Ca-metasomatism in the contact-zone of Ca-bearing rocks with igneous (often ultramafic) rocks (Brown, 1978, Henry, 1999; Marincea et al., 2001; Esteban et al., 2003). Xonotlite crystallizes in monoclinic symmetry and is usually forming acicular to fibrous crystals up to centimetre size.

Mamedov & Belov (1955, 1956a) were the first to propose a structure model for xonotlite which was later confirmed by Eberhard et al. (1981). The structure of xonotlite consists of Ca-O-polyhedral layers and $[Si_6O_{17}]$-*Dreier-Doppelketten*. Two of the Ca-atoms are in sevenfold coordination surrounded by 6 oxygens in form of a trigonal prism and one additional oxygen on one prism plane, the third Ca-atom is in octahedral coordination (Fig. 1). CaO_6-octahedra and CaO_7-polyhedra in sevenfold coordination are both edge-sharing to form infinite chains in the b-direction. These structural elements were confirmed by extended X-ray absorption fine structure (EXAFS) investigations of Ca by Lequeux et al. (1999). The different chains are joined together by sharing edges and build up layers parallel to (001). Between these layers the $[Si_6O_{17}]$-*Dreier-Doppelketten* are located. Each of these double chains consists of two wollastonite-like *Dreier-Einfachketten* with two paired tetrahedra and one bridging tetrahedron as shown in Figure 1. These structural units were also confirmed by ^{29}Si NMR (Cong et al., 1996; Noma et al., 1998) on synthetic material. In comparison to Cong et al. (1996), Noma et al. (1998) observed a splitting of Q^2 sites which was attributed to different Si-O bond lengths and Si-O-Si angles of the paired tetrahedra and additional Q^1 sites which

were interpreted in terms of disorder and may be due to the synthesis path. In xonotlite the bridging tetrahedra are connected to the Ca-polyhedral layers. Due to the same length of $[Si_6O_{17}]$-*Dreier-Doppelketten* and two Ca-polyhedra there exist two different ways of attachment of the double chains to the polyhedral layers and hence various polytypes are possible (Gard, 1966; Kudoh & Takeuchi, 1979). The OH-group is located at the free apex of a CaO_6-octahedron where no bridging tetrahedra are attached (Kudoh & Takeuchi., 1979). Either every CaO_6-octahedron carries one OH-group, or CaO_6-octahedra containing two OH-groups are alternating with non-hydroxylated ones depending on the polytype developed. Noma et al. (1998) measured a ^1H NMR signal of 1.86 ppm in synthetic xonotlite. This proton was attributed as a component of a silanol-group. According to the xonotlite structure silanol-groups should not exist and their occurrence was not confirmed by other NMR studies (Grimmer & Wieker, 1971; Cong et al., 1996). In addition Noma et al. (1998) detected a broad shoulder at 5.26 ppm assigned to interlayer water, which was not verified by NMR- (Cong et al., 1996), IR- (Kalousek & Roy, 1957) and TGA/DSC-studies (Shaw et al., 2000).

Polytypism of xonotlite

Based on the structure model of Mamedov & Belov (1955, 1956a) and the confirmation of Eberhart et al (1981) six different polytypes (four ordered and two one-dimensional disordered) were suggested for xonotlite. These Polytypes can be seen as different stacking in [100]- and [001]-direction of a protoxonotlite-cell introduced by Kudoh & Takeushi (1979). In [100]-direction a continuous shift of **+b/4 or –b/4** or an alternating shift of **+b/4 and –b/4** is possible. In [001]-direction the protoxonotlite-cells are either in juxtaposed positions or shifted by **b/2**. The combination of these different stacking modes leads to four ordered polytypes M2a2bc, M2a2b2c, Ma2bc and Ma2b2c as shown in Figure 2. The letter M indicates the monoclinic symmetry of the protoxonotlite-cell and the three lower case letters, with numerical values in front if necessary, indicate the periodicity of the three directions in

space according to the modified Gard-notation (Guinier et al., 1984). The different cell parameters were determined by Hejny & Armbruster (2001) and are listed in Table 1. For M2a2bc and M2a2b2c twinning is possible if one species displays intergrowth of domains with continuous shift of **+b/4** in a-direction and continuous shift of **–b/4**. Streaks parallel to a* observed in single crystal patterns by Gard (1966) were assigned to the two known disordered polytypes P∞21 and A∞22 (Corresponding to Ma_d2bc and Ma_d2b2c in modified Gard-notation). Hejny & Armbruster (2001) extended the group of possible polytypes by $Ma2bc_d$ and $M2a2bc_d$, which have one-dimensional disorder in c-direction as indicated by streaks observed parallel to c* (Chisholm, 1980; Eberhard et al.,1981). Short spikes recorded perpendicular to the c* streaks have been interpreted in terms of two-dimensional disorder (Dornberger-Schiff, 1964), and they are termed with the corresponding symbol Ma_d2bc_d (Hejny & Armbruster, 2001).

Scope of this study

The determination of reaction and growth kinetics of CSH-phases and the calculation of thermodynamic equilibria demands material well characterized by its crystal chemistry. Single crystal diffraction is the most exact method to determine the different polytypes but these examinations are very time consuming and require crystals of a certain size. ufficiently big crystals of xonotlite are rare in nature and usually do not occur in synthesis experiments or technical applications. Therefore a less time-consuming determination method is required suitable for fine grained samples as well. Esteban et al (2003) could confirm the occurrence of M2a2b2c and Ma2b2c in the investigated sample from Carratraca (Spain) by comparing recorded and calculated diffraction patterns. Another attempt to determine the different polytypes was carried out by Garbev (2004) by using Rietveld-analysis and a structural model containing all polytypes. In the first part of this study the main focus is put on X-ray powder diffraction and pattern matching techniques of natural xonotlites. In addition a systematic

study on the composition of xonotlite from different localities is missing and only one report on the chemical variation in xonotlite from the Kalahari Manganese Field is given by de Bruiyn et al. (1999). Therefore a further aim of this study is to check for a dependency of the polytypes evolved and the chemical composition.

Experimental

Ten natural xonotlite samples from seven different localities and different lithologies were investigated (Tab. 2). All samples form polycrystalline aggregates of white to whitish crystals. Most of them consist of fine fibres sometimes displaying radial growth. In the sample from Mäntijärvi, Finland (Xon2) xonotlite is filling small cavities in a kimberlite and is accompanied by calcite. Xonotlites from Bazhenovskoe and Chukotka, Russia (Xon1, Xon3, Xon6, Xon7) and Carratraca, Spain (Xon5) occur in rodingite veins crosscutting serpentinites.

Xon4, Xon8 and Xon10 from the Kalahari Manganese Field, RSA and Xon9 from Franklin, New Jersey, are products of metasomatism caused by low temperature hydrothermal fluids in manganese- and zinc-manganese-deposits respectively. Xon4 is a well crystallized xonotlite forming acicular crystals up to 30 mm long and 1mm in diameter, which were previously used by Hejny & Armbruster (2001) for single crystal diffraction.

Quantitative chemical data for xonotlites were obtained by electron microprobe analysis (EMPA) using a CAMECA SX100 operated at 15 keV acceleration voltage and 20 nA beam current. Synthetic wollastonite (Ca,Si), periclase (Mg), corundum (Al), hematite (Fe), escolaite (Cr), natural ilmenite (Mn,Ti), albite (Na) and osumilite (K) were used as standards and matrix correction was performed by the PAP procedure (Pouchou & Pichoir, 1984). The reproducibility of standard analyses was <1% for each element routinely analysed.

X-ray powder diffraction (XRPD) data were determined with a STOE STADI P-diffractometer using a SIEMENS KRISTALLOFLEX 710/710H generator operating at the following conditions: 40 kV, beam current 30mA, curved Germanium monochromator, step scan in the 2Θ region 10-60° with 0,01 2Θ steps and Cu-Kα-radiation (λ=1.5406 Å). For determination of the present polytype or polytypic intergrowth the theoretic powder diffraction patterns of the four ordered polytypes were simulated for Cu-Kα-radiation. For calculations the tool "Visualizer" of ICSD was applied using the atomic coordinates for M2a2bc, Ma2bc and Ma2b2c of Hejny & Armbruster (2001). The diffraction pattern for the polytype M2a2b2c described by Kudoh & Takeushi (1979) was calculated with the software package "Fullprof" for Rietveld-refinement (Rodriguez-Carvajal; 1993). The obtained patterns were used to define every polytype by a set of diagnostic peaks in the range of 10-35° 2Θ. The polytypes of natural xonotlites were determined by matching the measured patterns with the model patterns. To revise the quality of the results Rietveld-analysis was performed for a selected sample (Figure 5) by using the FULLPROF-software (Rodriguez-Carvajal; 1993)

Results

Chemical composition

The chemical compositions of xonotlites under investigation are shown in Table 4. The data are the mean out of 10 analyses except for Xon2 where only three analyses were taken into account. All xonotlites are predominately Calciumsilikates, other elements only occur as minor components. The amount of SiO_2 ranges from 49.37 wt% up to 51.10 wt%. The CaO contents vary between 45.76 wt% and 47.48 wt%. Samples from the Kalahari Manganese Field (N'Chwaning and Wessels Mine) show the highest amounts of SiO_2 (49.37-51.10 wt%)

accompanied by a lower amount of CaO (45.82-47.48 wt%). Xonotlites from rodingites (Bazhenovskoe, Chukotka and Carratraca) contain the highest amounts of CaO up to 47.37 wt%. The content of Al_2O_3 is low and varies between 0.02 wt% and 0.04 wt% except for a sample from the Wessels Mine (Xon10 in Tab.4) and from Carratraca (Xon5 in Tab.4) revealing 0.12 and 0.06 wt%, respectively. The contents of FeO are negligible except for samples Xon2 showing a slightly higher value of 0.10wt%. MnO is considerably enriched in samples from the Kalahari Manganese Field (Xon4,Xon8 in Tab. 4) and the Franklin (Xon9), revealing contents of MnO from 0.18 up to 0.36 wt% as shown in Table 3. Only xonotlite from a kimberlite (Xon2 in Tab.4) and from rodingites in Carraraca (Spain, Xon5 in Tab.4) contains slightly higher alkali contents of 0.09 and 0.04 wt% Na_2O, respectively. The contents of MgO, K_2O, TiO_2 and Cr_2O_3 are negligible in all samples.

Simulated diffraction patterns

The calculated diffractograms of all four polytypes are shown in Figure 3. The patterns are displayed in two different scales (Figure 3) ranging from 10 to 25° 2Θ and 25 to 35° 2Θ, respectively. At the first sight the four diffraction patterns are quite similar. Seven peaks of high intensity and five of lower intensity are common for all four polytypes. Characteristic differences can only be found by a detailed investigation of peaks with lower intensities in the region between 10 and 35° 2Θ as depicted in Table 5. Peaks which allow distinction between the four polytypes are called "characteristic peaks". The indication corresponding to the values of ° 2Θ used in the text can be taken likewise from Table 5.

The calculated pattern of the M2a2b2c polytype shows ten characteristic peaks. Most demonstrative is the (013) peak at 22.7°2Θ. Weaker characteristic peaks are those at 13.8, 15.7, 18.8, 23.9, 26.1, 27.2, 29.2, 32.0 and 34.3° 2Θ.

The M2a2bc polytype shows nine characteristic peaks. The strongest are the (011), (-111) and (012) peaks at 17.6, 19.1 and 28.4° 2Θ, respectively. Further weaker peaks are those at 12.3, 14.3, 21.8, 29.3, 31.1 and 33.6° 2Θ.

The pattern of the Ma2b2c polytype has two stronger characteristic peaks at 23.1° 2Θ (113) and 29.6° 2Θ (511). Weaker peaks are to be found at 22.5, 30.8, 24.9, 34.5 and 14.6° 2Θ.

The pattern of the Ma2bc polytype shows the strongest peak at 18.2° 2Θ (111) and also distinct characteristic peaks at 17.4, 18.2, 20.4 and 28.6° 2Θ. Weaker peaks are at 12.0, 13.1, 15.9, 19.7, 23.6, 28.2, 30.2 and 32.3° 2Θ.

Polytypes in natural xonotlites

The characteristic peaks of the different polytypes in the investigated samples are summarized in Table 5. Most of the xonotlites show intergrowth of two or three different polytypes. As the characteristic peaks are of very low intensity sometimes not all are detectable in the investigated patterns. The assignement is demonstrated in Figure 4 for Xon2 (Mäntijärvi, Finland). Due to occurring texture effects, which are discussed later, some peaks have highly increased and others decreased intensities. Some of the characteristic peaks can coincide with those of other polytypes (if occurring in the same sample). For this reason different peaks had to be used for polytype assignment in the different samples. The reproducibility of the obtained results was verified by means of random sampling.

M2a2b2c

Every investigated xonotlite shows the peaks at 13.8, 22.7 and 34.3° 2Θ, characteristic for the M2a2b2c-polytype. These three peaks often have broad, asymmetrical shapes. They show a weaker intensity in the patterns of Xon2 (Mäntijärvi, Finland, Fig.4) and Xon8 (Wessels Mine, South Africa). This is due to a minor amount of the M2a2b2c polytype in these samples. In addition there is a distinct reflection at 26.1° 2Θ in Xon2 (see Fig.4). This reflection is also visible in the patterns of Xon3 (Chukotka, Russia) and Xon10 (Wessels Mine, South Africa) but here with a medium intensity. The characteristic peaks at 18.8 and 23.9° 2Θ are detectable only in the pattern of Xon5 (Carratraca, Spain). The (-111) peak at 15.7° has been found only subordinate in the patterns of Xon1 and Xon3, both from Russian rodingites. In sample 1, 3 and 10 the (2-13) peak is weakly developed. The (3-11) peak is detectable in patterns of Xon1, Xon4, Xon6 and Xon8 (Tab. 6). Sample 6, 7 and 10 show only characteristica of the M2a2b2c polytype. Whereas the peak at 13.8° 2Θ is weak in the calculated pattern, nearly all natural xonotlites show a much higher intensity. In contrast the 2-13 peak is of medium intensity in the calculated pattern, whereas in Xon5 it shows only a weak intensity.

M2a2bc

The M2a2bc polytype could be found in three of the investigated xonotlite samples. All three patterns show the peaks at 28.4, 29.3 and 33.6° 2Θ which have been used for the assignment of this polytype. Xon3 (Chukotka, Russia) shows every peak characteristic for the M2a2bc polytype (see Table 5) with exception of the (011) peak at 17.6° 2Θ, whereas the latter peak is strongly developed in the pattern of Xon2 (Mäntjärvi, Finland, Fig. 4).

The normally weak (-112) peak is highly increased in sample 5 from Carratraca (Spain), additional characteristic peaks of the M2a2bc polytype have been found only between 25 and 35° 2Θ.

Ma2b2c

This polytype could be found in four xonotlite samples. Two of them come from Russian rodingites (Xon1, Xon3) and the two remaining from manganese ore deposits at Wessels Mine in South Africa (Xon8) and at Franklin (New Jersey) in the USA (Xon9). All four patterns show the (213) and (511) reflections at 24.9 and 29.6° 2Θ. The (-111) peak at 14.6 2Θ, which has a very low intensity in the calculated pattern, is missing only in Xon9 (Franklin, New Jersey). The detection of the (013) and (611) characteristic peaks at 22.5 and 34.5° 2Θ is difficult due to the superposition with characteristic peaks of the M2a2b2c polytype at 22.7 and 34.3° 2Θ. The peaks at 23.1 2Θ and 30.8 2Θ were detected in the patterns of Xon9 and Xon3, respectively.

Ma2bc

This polytype has been found in four of the investigated xonotlites (Xon1, Xon2,Xon3, Xon4). The highest amount is detected in Xon2 due to very strong peaks at 30.2 and 32.3° 2Θ and a medium peak at 20.4° 2Θ which are to be seen with much lower intensities in the other patterns.

The peaks at 13.1, 28.2 and 28.6° 2Θ are missing in Xon2 but developed in the remaining three xonotlites. The peak at 12.0° 2Θ (weak in the calculated pattern) is detectable in Xon1 and Xon2, the peak at 18.2° 2Θ in Xon2 and Xon3 patterns. Both xonotlites from Russian rodingites show the peak at 15.9° 2Θ. The very weak peaks at 19.7 and 23.6° 2Θ of the calculated pattern are only developed in Xon3 and Xon1, respectively. The peak at 17.4 2Θ could not be detected.

Discussion

In this study ten different natural xonotlites were investigated concerning chemical composition and polytypism. Due to the different lithologies of the localities the samples could be assigned to three different groups. Xonotlites formed in kimberlites (1), xonotlites in rodingites (2) and xonotlites formed by metasomatic processes close to Mn- and Mn-Zn- ore-deposits (3), respectively.

Chemical composition

Group 1 is only represented by the xonotlite from Mäntijärvi (Finland). This sample exhibits a low SiO_2- and CaO-content and a slight enhancement of Na_2O up to 0.09 wt%.

Group 2-xonotlites were formed in rodingites (Xon1, Xon3, Xon5, Xon6) and are characterized by the highest CaO-amount of 47.07 up to 47.59 wt%. Analyses of Carratraca-xonotlites (Xon5) are in good agreement to those of acicular crystals replacing hydrogrossular of the same locality published by Esteban et al. (2003) as shown in Table 3 and 4.

Samples belonging to group 3 are formed by hydrothermal alteration (250-400ºC) of the primary sedimentary and low-grade metamorphic Mn-ores (Kalahari Manganese Field ; Xon4, Xon8) or high-grade metamorphic Mn-Zn-ores (Franklin, New Jersey; Xon9) and showing slightly higher Mn-content. This could be explained by a preferred integration of Mn on the Ca-positions in Xonotlite-structure, likewise indicated by a lower Ca-content.

A substitution of Al for Si on tetrahedral-sites, indicated by the higher amount of Al_2O_3 could be detected noticeably only in the sample from Carratraca and one from Wessels mine.

De Bruiyn et al. (1999) described a higher SiO_2- and CaO-content in xonotlites of N'Chwaning Mine in comparison to those of Wessels Mine, which could be confirmed in this investigation, as depicted in Table 3 and 4. In addition De Bruiyn et al. (1999) detected slightly higher FeO-contents which could not be verified in the samples of this study.

In all investigated xonotlites Al, Na and Mn are the only elements which are enriched in remarkable amounts. A enhancement of Mg known from synthetic xonotlites (Quian et al., 1997) could not be detected in the investigated natural xonotlites.

Polytypes

Due to the minor crystal size of xonotlites X-ray single crystal diffraction is often not applicable to distinguish between the different polytypes. Therefore the determination in this study is made by pattern matching powder diffractograms of investigated xonotlites and calculated patterns of the four ordered polytypes. Most of the investigated xonotlites show intergrowth of two or more polytypes.

In all samples the M2a2b2c polytype was found but in Xon2, Xon8 and Xon9 with only minor amounts. This predominance is an effect of specific growth conditions availing the development of one polytype. Hejny and Armbruster (2001) explain this preferred development by the more balanced and therefore favourable distribution of OH-groups at the free apices of each Ca-octahedron in the structure of this polytype.

The Ma2b2c-polytype could be detected in two samples found in Russian rodingites of Bazhenovskoe (Xon1) and Chukotka (Xon3) and in two samples found in Mn-ore deposits from the Wessels Mine located in the Kalahari Manganese Field of South Africa (Xon8) and from Franklin, New Jersey (Xon9), respectively.

Ma2bc is developed in the xonotlite from Mäntijärvi (Finland) with an exceptionally high amount and in the well crystalline sample from N'Chwaning Mine (Xon4) investigated by Hejny & Armbruster (2001). In addition this polytype does exist with minor amounts in xonotlites of Bazhenovskoe (Xon1) and Chukotka (Xon3).

The occurrence of M2a2b2c and Ma2bc in Xon4 is in good agreement with the investigations of Hejny & Armbruster (2001) on xonotlites from the same locality. They also reported the presence of Ma2b2c polytype which could not be confirmed in this study. This can be

explained by different intergrown polytypes even in samples from the same locality due to small scale fluctuations in the physico-chemical conditions during formation.

The M2a2bc-polytype was first detected in natural xonotlite from Chukotka (Russia) by Garbev (2004) using Rietveld-modelling of diffraction data obtained by syncrotron radiation. In this study the M2a2bc polytype could clearly be detected in xonotlites from Mäntijärvi (Xon2) and Chukotka (Xon3). Esteban et al. (2003) made their assignment in Xonotlites from Carratraca (Spain) by use of X-ray powder diffraction, too. Based on the by then missing description of the occurrence of M2a2bc polytype in natural xonotlites in literature, this polytype was not taken into account by Esteban et al.(2003). This is in contrast to the results of this study where the development of M2a2bc polytype in xonotlite from Carratraca (Xon5) could be confirmed by the presence of three characteristic reflections.

The above mentioned lower intensity of (h0l)-reflections in all patterns can be explained by a preferred orientation of the acicular crystals along their elongated b-axes during preparation. The observed phenomenon of inverse intensity-ratio in (0kl) and (hkl)-reflections in M2a2bc-polytype may be caused by preferred orientation of more disk-shaped crystals.

The powder diffraction data of sample 8 from Wessels mine (South Africa) were used additionally to perform a Rietveld refinement (Figure 5). The two polytypes determined by pattern matching were used as phases for the refinement. We obtained the best results by taking into account a preferred orientation in [010] which corresponds to the elongated b-direction of the crystals. But there is also a recognizable influence of the above mentioned [h0l] direction which could explain the observed difference in the region of the (102) reflection. The results show the exigence of further refinement with main focus on the different preferred orientations. For this reason we abandoned a quantitative analysis for now.

Conclusions

A clear coherence of different lithology of the habitat and the developed polytype could not be confirmed. Xon2 from kimberlites (Mäntijärvi, Finland) is in a special position referring to this question. It displays a very high amount of Ma2bc polytype compared to all other investigated samples. This can be linked to the special growth conditions in kimberlites.

The results of this study clearly demonstrate that X-ray powder diffraction is a useful and fast method to distinguish the different polytypes developed in xonotlite. It is the preferable option if crystallite size is too small for X-ray single crystal diffraction as it is typical for natural and synthetic xonotlites. The results show also the need of further investigations by other powder methods like FTIR and Raman spectroscopy. FTIR-data of xonotlite were published by Hochleitner & Fehr (2002) and an extensive investigation will be published in a forthcoming paper.

Acknowledgements

We would like to thank Prof. Dr. Thomas Armbruster and Dr. Clivia Hejny for kindly providing a natural xonotlite sample from N'Chwaning (South Africa). Detailed comments by an anonymous reviewer and Prof. Dr. Wolfgang Schmahl were also greatly appreciated.

References

BROWN, P.A. (1978): Xonotlite: a new occurrence at Rose Blanche, Newfoundland.- Can.Mineral.,**16**: 671-672

CHISHOLM, J.E. (1980): Polytism in xonotlite, $Ca_6Si_6O_{17}(OH)_2$. *In* Electron Microscopy and Analysis, 1979. Inst. Phys. Conf. Ser., **52**: 109-112

CONG, X. & KIRKPATRICK, R.J. (1996): ^{29}Si and ^{17}O NMR Investigation of the Structure of Some Crystalline Calcium Silicate Hydrates. - Advn. Cem. Bas. Mat., **3**: 133-143

DANA, E.S. & FORD, W.E. (1892): The system of mineralogy if James Dwight Dana, **6th edition**: 569; publisher unknown, New York, United States (USA)

DE BRUIYN, H.; SCHOCH, A.E.; VAN DER WESTHUIZEN, W.A & BEUKES, G.J. (1999): The chemical composition of xonotlite and associated inesite from the Nchwaning and Wessels mines, Kalahari manganese field, South Africa. - N.Jb.Miner.Mh., **5**: 212-222

DORNBERGER-SCHIFF, K. (1964): Grundzüge einer Theorie der OD-Strukturen aus Schichten. -Abhandlungen der Deutschen Akademie der Wissenschaften zu Berlin. Klasse für Chemie, Geologie und Biologie, **3**:1-107

EBERHART; E.; HAMID, S. & RÖTTGER, B. (1981): Strukturverfeinerung und Polytypie von Xonotlite:- Z. Krist., **154**: 271-272

ESTEBAN, J.J.; CUEVAS, J. & TUBIA, J.M. (2003): Xonotlite in rodingite assemblages from the Ronda peridotite Betic Cordilleras, Southern Spain. –Can. Mineral., **41**: 161-170

GARBEV, K. (2004): Struktur, Eigenschaften und quantitative Rietveldanalyse von hydrothermal kristallisierten Calciumsilikathydraten (CSH-phasen),Thesis, University of Karlsruhe

GARD, J.A.(1966): A System of Nomenclature for the Fibrous Calcium Silicates, and a Study of Xonotlite Polytypes. –Nature, **211**: 1078-1079

GRIMMER, A.-R. & WIEKER, W. (1971): Bestimmung der Art der Wasserbindung im Xonotlit 6CaO 6SiO_2 H_2O. –Z.anorg.allg.Chem., **384**: 34-42)

GUINIER , A.; BOKIJ, G.B.; BOLL-DORNBERGER, K.; COWLEY, J.M.; DUROVIC, S.; JAGODSINSKI, H.; KRISHNA, P.; DEWOLFF, P.M.; ZVYAGIN, B.B.; COX, D.E.; GOODMAN, P.; HAHN, TH.; KUCHITSU, K. & ABRAHAMS, S.C. (1984): Nomenclature of Polytype Structures. Report of the International Union of Crystallography Ad.Hoc Committee on the Nomenclature of Disordered, Modulated and Polytype Structures. -Acta Cryst, **A40**: 399-404

HEJNY,C. & ARMBRUSTER, T. (2001): Polytypism in Xonotlite $Ca_6Si_6O_{17}(OH)_2$.- Z.Kristallogr., **216**: 396-408

HENRY, D.A. (1999): Cuspidine-bearing skarn from Chesney Vale, Victoria. –Australian J. of Earth Sciences, **46**: 251-260

HOCHLEITNER, R. & FEHR, K.T. (2002): Infrared spectroscopy of natural xonotlites. –Beih .z. Eur. J. Mineral., **14**: 70

KALOUSEK, G.L. & ROY, R. (1957): Crystal Chemistry of Hydrous Calcium Silicates: II, Characterization of interlayer Water. - J. Am. Ceram. Soc., **40 [7]**: 236-239

KUDOH, Y. & TAKEUSHI, Y. (1979): Polytypism of xonotlite: (I) Structure of an A1 polytype - Min.Journal, **9**: 349-373

LEQUEUX, N., MORAU, A.; PHILIPPOT, S. & BOCH, P. (1999): Extended X-ray Absorbtion Fine Structure Investigation of Calcim Silicate Hydrates. –J. Am. Ceram. Soc., **82 [5]**: 1299-1306

MAMEDOV, KH. & BELOV, N.V. (1956a): Crystal structure of the mineral group wollastonite. 1 structure of xonotlite. - Zapiskii Vsesoyuz. Miner. Obshchest, **85**: 13-38

MAMEDOV,KH. & BELOV, N.V. (1955): Crystal structure of xonotlite. –Dokl.Akad.Nauk SSSR, **104**: 615-618

MARINCEA, S.; BILAL, E.; VERKAEREN, J.; PASCAL, M.-L; FONTEILLES, M. (2001): Superimposed parageneses in thee spurrite-, tilleyite- and gehlenite-bearing skarns from Cornet Hill Apuseni Mountains, Romania. –Can. Mineral., **39**: 1435-1453

NOMA, H. ADACHI, Y.; MATSUDA, Y. & YOKOYAMA, T. (1998): ^{29}Si and ^{1}H NMR of Natural and Synthetic Xonotlite. - Chemistry Letters, 219-220

POUCHOU, J.L. & PICHOIR, F. (1984): A new model fro quantitative X-ray microanalysis Part I: application to the analysis of homogenious samples. -La Recherche Aérospatiale, **3**: 13-38

PRODAN, A. MARINCOVIC, V.; VENE, N.; KURBUS, B. & BOSWELL, F.W. (1983): On structural relations between the CaO-SiO_2-H_2O phases. –Z. Kristallogr., **164**: 189-209

RAMMELSBERG, C. (1866): Über den Xonaltit, ein neues wasserhaltiges Kalksilikat, und den Bustamit aus Mexico. - Z. deutsch. geol. Ges. **18**: 33-34

SHAW, S. HENDERSON, C.M.B. & KOMANSCHEK, B.U. (2000): Dehydration/recrystallization mechanism , energetics, and kinetics of hydrated calcium silicate minerals: an in situ TGA/DSC and synchrotron radiation SAXS/WAXS study. - Chemical Geology, **167**: 141-159

QUIAN, G.; XU, G.; LI, H. & LI, A. (1997): Mg-Xonolite and its coexisting phases. –CCR, **27 [3]**: 315-320

RODRIGUEZ-CARVAJAL, J. (1993): Recent advances in magnetic structure determination by neutron powder diffraction.- Physica B., **192**: 55 - 69

Authors' address:
SASKIA BERNSTEIN, KARL THOMAS FEHR: Department für Geo- und Umweltwissenschaften, Ludwig Maximilians Universität, Theresienstraße 41, 80333 München

RUPERT HOCHLEITNER: Mineralogische Staatssammlung, Theresienstraße 41, 80333 München

Corresponding author's e-mail: bernstein@min.uni-muenchen.de

Table headings:

TABLE 1: Lattice parameter and symmetry of the ordered polytypes
after Hejny & Armbruster (2001)

TABLE 2: Localities of investigated xonotlites

TABLE 3: Literature values for chemical composition of natural xonotlites

TABLE 4: Average composition of investigated xonotlites obtained by EMPA, n= number of analyses taken into account, numbers in parentheses denote for standard deviation

TABLE 5: Characteristic peaks found in the 10 diffraction patterns and the resulting assigned polytypes (w=weak, m= medium, s=strong, b=broad)
the dominating polytype is marked by "+" those of minor amounts by "*"

Figure captions

Fig 1: structure of xonotlite

Ca-polyhedra: dark grey in octahedral coordination and light grey in sevenfold coordination
Si_6O_{17} tetrahedral-double chains in middle grey

protoxonotlite-cell with white dashed outlines
notice the two different possibilities (light and middle grey) of connecting a SiO_4-tetrahedral chain to the Ca-polyhedra

Fig 2: Four ordered polytypes shown as different stacking of the protoxonotlite-cell (dark outlines) after Hejny & Armbruster (2001).
Cells with displacement in c-direction are drawn with dashed outlines

Fig 3: Calculated powder diffraction patterns for all ordered polytypes (Cu-Kα) in the range of 10-25 and 25-35° 2Θ

Fig 4: Diffraction pattern of Xon2 (Mäntijärvi, Finland), peaks taken for assignment are marked by arrows and the number of corresponding polytype
1= M2a2b2c, 2=M2a2bc, 3=Ma2b2c, 4=Ma2bc

Fig 5: Rietveld-refinement for Xon8 (Wessels Mine, Souh Africa)

TABLE 1

	a [A]	**b [A]**	**c [A]**	**α [°]**	**β [°]**	**γ[°]**	**space group**
protoxonotlite cell	8.516	7.363	7.012	90.00	90.37	90.00	
M2a2bc	8.712	7.363	7.012	89.99	90.36	102.18	P1
M2a2b2c	8.712	7.363	14.023	89.99	90.36	102.18	A1
Ma2bc	17.032	7.363	7.012	90.00	90.36	90.00	P2/a
Ma2b2c	17.032	7.363	14.023	90.00	90.36	90.00	A2/a

TABLE 2

sample	**locality**	**reference**
Xon 1	Bashenovskoje, Russia	[a)]MSM 30538
Xon 2	Mäntijärvi, Finland	[a)]MSM 30536
Xon 3	Tschukotka, Russia	[a)]MSM 27382
Xon 4	N'Chwaning, South Africa	Fe175[b)]
Xon 5	Carratraca, Malaga,Spain	MSM 30537
Xon 6	Bashenovskoje, Russia	[a)]MSM
Xon 7	Bashenovskoje, Russia	[a)]MSM 28676
Xon 8	Wessels Mine, South Africa	Fe50
Xon 9	Franklin, New Jersey USA	[a)]MSM 1218
Xon 10	Wessels Mine, South Africa	Fe

a) Mineralogische Staatssammlung München
b) Hejny & Armbruster

TABLE 3

	Carratraca (1)	N´chwaning South Africa (2)	Wessels mine South Africa (2)	Heguri Japan (3)	Ohmi-Machi Japan (4)	Tchukotka Russia (5)	Tetela de Xonotla Mexico (6)	Cornett Hill, Romania (7)
SiO_2	50.07	50.02	49.96	49.99	50.80	49.52	49.58	49.79
CaO	47.39	46.15	45.85	46.19	44.70	46.26	43.56	47.28
Al_2O_3	0.04	n.m	n.m.	n.m.	0.38.	0.29	n.m.	0.20
FeO	0.07	0.28	0.62	0.36	0.04	n.m.	1.31	0.03
MnO	0.03	0.18	0.21	0.16	0.01	n.m.	1.79	0.01
MgO	0.00	0.05	0.05	n.m.	n.m.	n.m.	n.m.	0.08
Na_2O	0.02	n.m	n.m.	0.17	0.78	0.01	n.m.	0.00
K_2O	0.01	n.m.	n.m.	0.02	0.02	0.01	n.m.	n.m.
TiO_2	0.00	n.m.	n.m.	n.m.	n.m.	n.m.	n.m.	n.m.
Cr_2O_3	0.02	n.m.	n.m.	n.m.	n.m.	n.m.	n.m.	n.m.
H_2O		2.50	2.50	3.05	3.18.		3.70	2.51
total		99.18	99.19	99.94	99.92	96.11(incl. 0.02SO_2)	99.94	99.90

(1) Esteban et al., 2003; (2) de Bruiyn et al, 1999; (3) Kudoh et al, 1979;(4) Noma et al., 1998:
(5) Garbev, 2004; (6) Dana,E.S., 1892; (7) Marincea et al., 2001

TABLE 4

	Xon1	Xon2	Xon3	Xon4	Xon5	Xon6	Xon7	Xon8	Xon9	Xon10
K_2O	b.d.	b.d.	b.d.	b.d.	0.00	b.d.	b.d.	b.d.	b.d.	b.d.
Na_2O	b.d.	0.09(01)	b.d.	b.d.	0.03	b.d.	b.d.	0.05(03)	b.d.	b.d.
MgO	b.d.	b.d.	b.d.	b.d.	0.03	b.d.	b.d.	b.d.	b.d.	b.d.
Al_2O_3	0.04(02)	b.d.	0.03(01)	b.d.	0.08	0.02(01)	0.02(02)	b.d.	0.02(01)	0.12(06)
SiO_2	49.80(36)	479.37(05)	49.71(16)	51.10(18)	49.93	50.11(18)	49.37(23)	50.21(62)	49.41(23)	50.08(81)
CaO	47.37(22)	45.76(37)	47.37(29)	47.01(28)	47.08	47.10(16)	47.48(18)	46.73(41)	46.55(25)	45.82(77)
TiO_2	b.d.	b.d.	b.d.	b.d.	0.00	b.d.	b.d.	b.d.	b.d.	b.d.
MnO	b.d.	b.d.	b.d.	0.36(03)	0.01	b.d.	b.d.	0.18(02)	0.36(16)	b.d.
FeO	b.d.	0.10(05)	b.d.	b.d.	0.02	b.d.	b.d.	b.d.	b.d.	b.d.
Cr_2O_3	b.d.	b.d.	b.d.	b.d.	0.01	b.d.	b.d.	b.d.	b.d.	b.d.
Total	97.31(19)	95.37	97.21(30)	98.53(20)	97.19	97.31(23)	96.99(39)	97.20(45)	96.42(48)	96.09(12)

TABLE 5

° 2Θ	hkl	Xon1	Xon2	Xon3	Xon4	Xon5	Xon6	Xon7	Xon8	Xon9	Xon10
					M2a2b2c						
13.8	011	s,b	w	s,b	s	m	s,b	s,b	w	m	s,b
15.7	-111	w	-	s	-	-	-	-	-	-	-
18.8	111	-	-	-	-	m	-	-	-	-	-
22.7	013	s,b	w	s.b	s	s	s,b	s,b	m,b	m	s,b
23.9	1-13	-	-	-	-	w	-	-	-	-	-
26.1	113	-	s	m	-	-	-	-	-	-	m
27.2	211	-	-	-	w	s	s	-	-	-	m
29.2	2-13	m	-	w	-	-	-	-	-	-	ww
32	3-11	w	-	-	w	-	ww	-	w	-	-
34.3	015	s,b	w	s	s,b	s	m	s	ww	w	m
					M2a2bc						
12.3	010	-	w	m	-	-	-	-	-	-	-
14.3	1-10	-	-	m	-	-	-	-	-	-	-
17.6	011	-	m	-	-	-	-	-	-	-	-
19.1	-111	-	-	s	-	-	-	-	-	-	-
21.8	111	-	-	m	m*	-	-	s*	-	-	-
28.4	012	-	m	m	-	w,b	-	-	-	m	-
29.3	-112	-	s	m	-	ss	-	-	-	-	-
31.1	-1-12	-	-	m-s	-	m	-	-	-	-	-
33.6	-212	-	m	m	-	w	-	-	-	ww	-
					Ma2b2c						
14.6	-111	w	-	s	-	w	-	-	m	-	-
22.5	013	m,b	-	s,b	-		-	-	-	-	-
23.1	113		-	-	-	s	-	-	-	m	-
24.9	213	w	-	m	-	-	-	-	w	w	-
29.6	511	s	-	s	-	w,b	-	-	w	s	-
30.8	-413	-	-	m	-	-	-	-	-	-	-
34.5	611	-	-	-	-	-	-	-		w	-
					Ma2bc						
12	010	m	w,b	-	-	m	-	-	-	-	-
13.1	110	w	-	m	w	-	-	-	-	-	-
15.9	210	m	-	m	-	-	-	-	-	w	-
17.4	011	-	-	-	-	-	-	ww	-	-	-
18.2	111	-	w	m	-	m	-	-	-	-	-
19.7	310	-	-	s	-	-	-	-	-	-	-
20.4	211	w	m	m	w	-	-	-	-	-	-
23.6	311	m	-	-	-	-	-	-	-	-	-
28.2	012	w	-	m	w	-	-	-	-	-	-
28.6	-112	m	-	w	w,b	-	w	-	-	-	-
30.2	212	m,b	ss	m	w	-	-	-	-	-	-
32.3	312	w	s	w	m	-	-	m*	-	-	-
M2a2b2c		+	*	+	+	+	+	+	+	*	+
M2a2bc			*	*		*					
Ma2b2c		*		*					*	+	
Ma2bc		*	+	*	*						

Figure 1

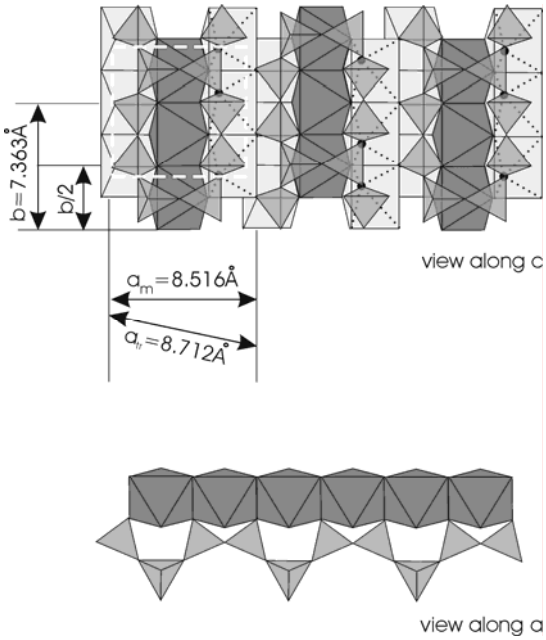

Figure 2

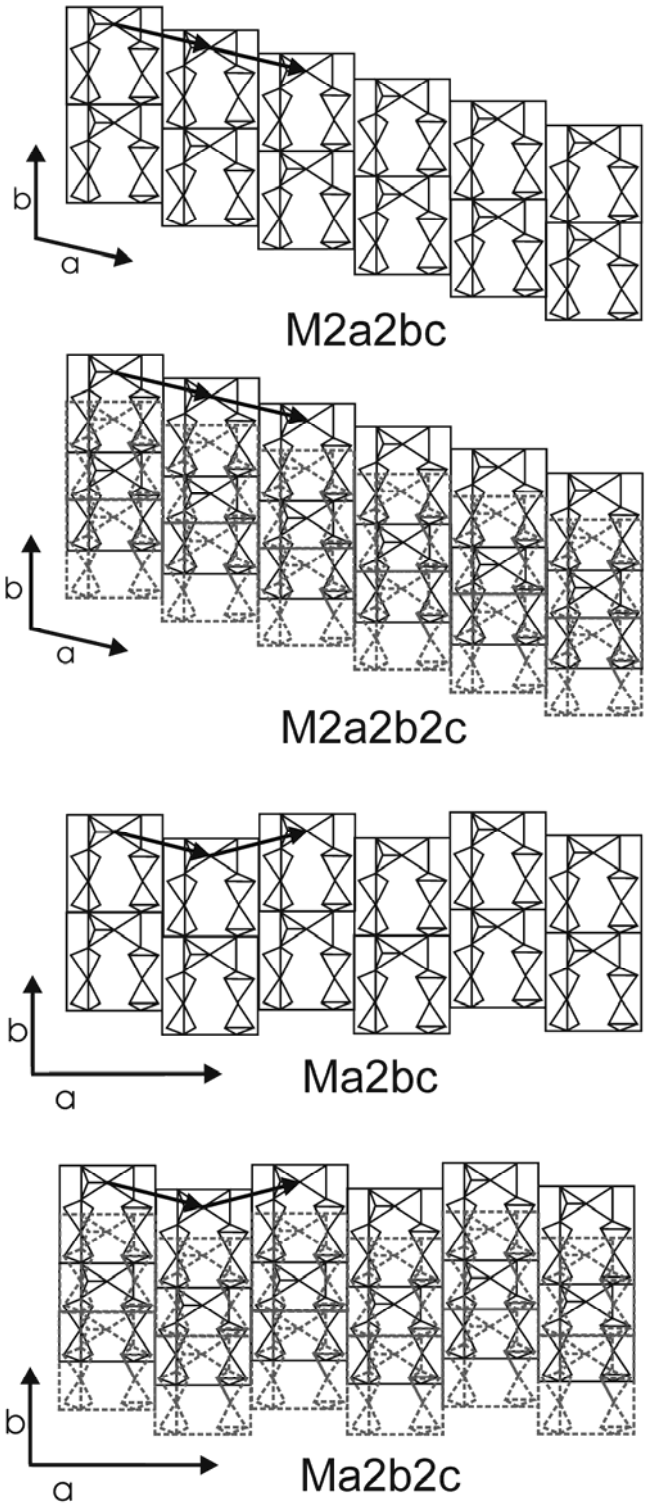

Figure 3

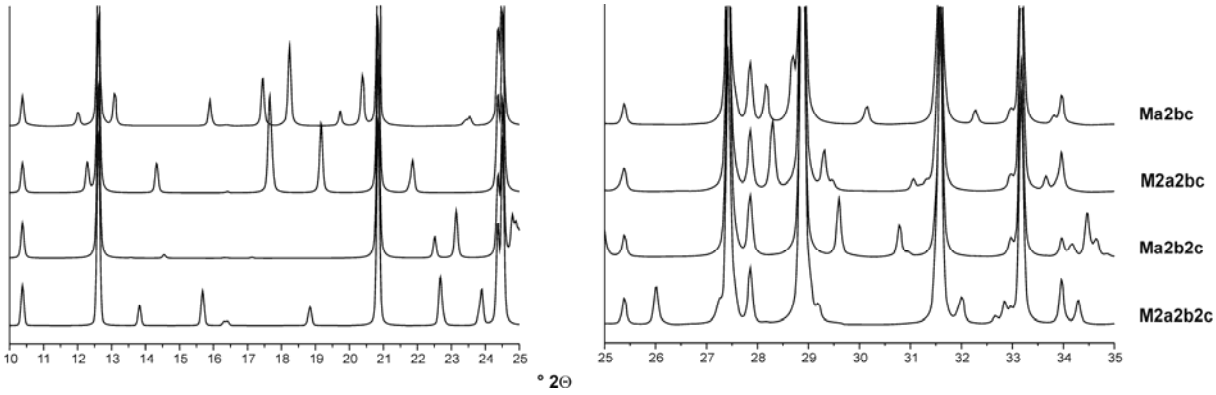
Ma2bc
M2a2bc
Ma2b2c
M2a2b2c
10 11 12 13 14 15 16 17 18 19 20 21 22 23 24 25
25 26 27 28 29 30 31 32 33 34 35
° 2Θ

Figure 4

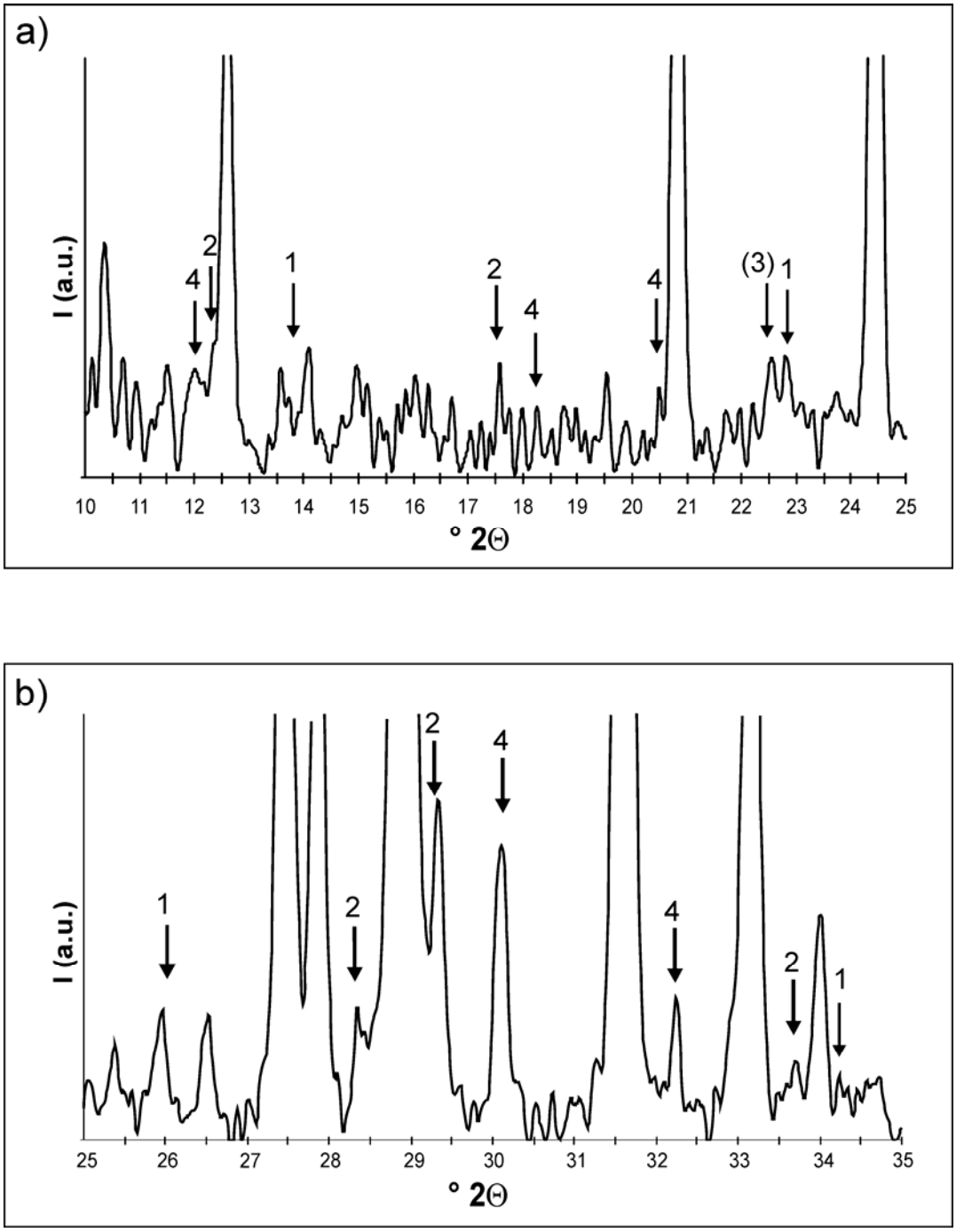
a)
I (a.u.)
4
2
1
2
4
4
(3)
1
10 11 12 13 14 15 16 17 18 19 20 21 22 23 24 25
° 2Θ
b)
I (a.u.)
1
2
2
4
4
2
1
25 26 27 28 29 30 31 32 33 34 35
° 2Θ

Figure 5

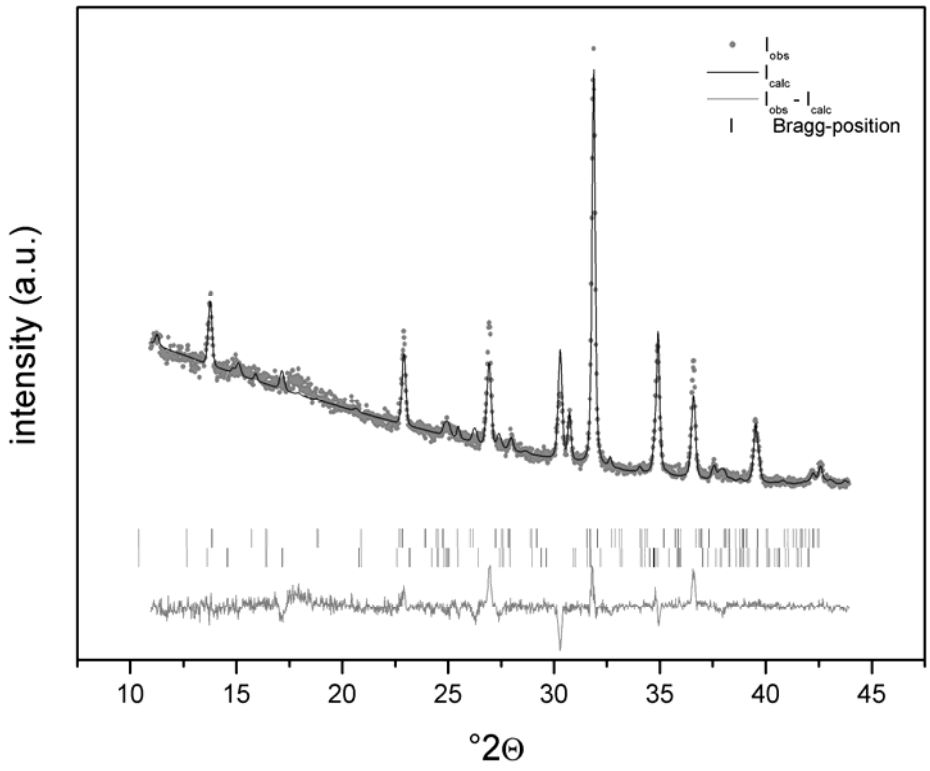
I obs
I calc
I obs - I calc
Bragg-position
intensity (a.u.)
10
15
20
25
30
35
40
45
°2Θ

Appendix C

A Hydrothermal Autoclave for Neutron Diffraction (HAND) – Design, Technique and Applicability
submitted to: Journal of Powder Diffraction, under rewiev

A Hydrothermal Autoclave for Neutron Diffraction (HAND) – Design, Technique and Applicability

K.T. Fehr[(1)], S. Bernstein[(1)], M. Huber[(1)], E. Peters[(2)], B. Walk-Lauffer[(3)], S.G. Zuern[(4)]

[(1)] Department of Earth & Environmental Sciences, Ludwig-Maximilians Universität, Munich, Germany

[(2)] YTONG Holding AG, R&D Center, Schrobenhausen, Germany; currently at Muenchener Stadentwaesserung, Munich, Germany

[(3)] Institute of Building- and Materials Chemistry, University of Siegen, Germany; currently at Rhein-Chemotechnik GmbH, Breitscheid, Germany

[(4)] YTONG Holding AG, R&D Center, Schrobenhausen, Germany; currently at PCI, Development Department, Augsburg, Germany

Abstract

An autoclave cell has been designed for performing time-resolved neutron diffraction analyses of dynamic processes occurring during hydrothermal reactions in the presence of a hydrous fluid. The hydrothermal autoclave for neutron diffraction (HAND) is described and its successful use on the crystallization of 1.13 nm tobermorite from lime and silica at 190°C and saturation pressure is demonstrated. The reaction time was set to 8 hours and the reaction product consisted of tobermorite, semi-crystalline calcium-silicate-hydrate C-S-H(I) and quartz. Tobermorite is formed on the expense of portlandite and quartz and by the reaction of semi-crystalline calcium-silicate-hydrate C-S-H(I) with quartz.

Keywords: Hydrothermal, autoclave, neutron diffraction, kinetic, tobermorite

1. Introduction

Hydrothermal syntheses under saturated steam pressure are usually performed by using so called Parr-bombs. Once the experiment is completed the sample is quenched and the reaction products are analysed. By this way of synthesizing one always has to deal with several problems. Quenching effects can influence the final phase relations in particular and there is no guarantee to freeze the process exactly at one stage and to quench it without change. Furthermore a huge number of experiments at different compositions and temperatures are needed to obtain a sufficient amount of data points which means an enormous expenditure of time. This is hardly possible by using Parr bombs without an enormous amount of both time and work. Reactions with fast kinetics are impossible to record by this method and reliable data especially from the early state of the reaction are missing. The best way to obtain kinetic data of a reaction is to observe it in-situ by x-ray or neutron diffraction. For those experiments special reaction cells are needed tailored to the particular requirements of the scientific problem and of course the applied instrument, respectively.

The reaction we are focussed on is the formation of 1.13nm tobermorite taking place during the hydrothermal hardening of aerated autoclaved concrete, a building material used worldwide due to its excellent mechanical properties. Corresponding to the production process of AAC or lime silicate bricks the hydrothermal hardening of lime silica based samples in the vapour phase and not in suspension should be examined. Former thermodynamic and experimental studies [Gabrosek *et al*., 1993; Fehr and Zuern, 1997; Zuern and Fehr, 2000a] have shown that tobermorite is metastable in the presence of quartz at temperatures of production and decomposes to the equilibrium phases xonotlite ($Ca_6Si_6(OH)_6$)

or gyrolite according to the bulk composition. This fact shows the strong need of kinetic models in order to describe the metastable formation of 1.13 nm tobermorite.

Requirement for successful in-situ experiments according to reaction kinetics is a high-flux neutron source [Polak et al., 1990;Walton et al., 2000; Walton and O'Hare, 2000] that enables an adequate time resolution in spite of the absorption of X-rays by the reaction cell and a diffractometer with a sufficient 2Θ range to detect the basal reflections of tobermorite. All this is fulfilled at the D20 powder diffractometer of the neutron reactor at ILL. Based on that background a functional and cheap reaction cell was designed. The hydrothermal autoclave for neutron diffraction (HAND) allows a fast sample exchange and can easily be fitted to the D20 or by minor modification to powder diffraction devices at other neutron sources.

.

2. The Neutron Powder Diffractometer D20 at ILL

D20 [Walton and O`Hare, 2000, Hansen et al., 2008] is a medium to high-resolution 2-axis diffractometer at the high flux reactor source at the ILL in Grenoble, providing a neutron flux of up to 10^8 $ns^{-1}cm^{-2}$ at the sample position. The schematic set up is given in figure 1. A stationary curved linear position sensitive detector (PSD),consisting of 48 precisely cut microstrip gas chamber detector (MSGC) plates provides a usable aperture of 153.6° (2Θ). The polygonal arrangement of the juxtaposed plates enables the continuous and homogeneous coverage of the whole 2Θ range, each plate covering 3.2°. The gas filling of 3 bar ^3He and 1 bar CF_4 and the detection gap of 5 cm results in a neutron detection efficiency from 60% (λ= 0.8Å) to 90% (λ=2.4Å).

A vertically focusing monochromator of pyrolytic graphite HOPG (002) in reflection position offers λ = 2.4 or 2.5 Å at a take-off angle of 42° or 44°. It is equipped with graphite filters to suppress harmonics. A copper monochromator Cu (200) in transmission gives wavelengths of λ ≈ 0.82, 0.88, 0.94 or 1.3Å at take-off angles of 26°, 28°, 30° or 42°. At λ = 1.3 Å the

monochromatic beam has its highest flux of about $9.8 \cdot 10^7$ $n \cdot cm^{-2} \cdot s^{-1}$. Soller collimators allow to reduce the divergence of the incident polychromatic beam (27') to α_1 = 10' or 20'.

Beyond that, D20 is equipped with a furnace consisting of a heating element,45 mm in diameter, made of a vanadium sheet. As vanadium has a very low coherent scattering length for neutrons this material only adds constant incoherent scattering to the powder diffraction pattern. This heating device is placed in a large vacuum vessel, to avoid scattering by air and oxidizing of the vanadium sheet and to improve thermal insulation. It is equipped with neutron-absorbing B_4C screens and a direct beam-stop to avoid neutrons diffracted by the aluminium walls of vessel to propagate to the detector.

All the above mentioned characteristics enable a large choice in Q-space, resolution, wavelengths and flux and accomplish high precision in intensity measurements. This makes D20 adaptable to various levels of crystallographic complexity and rapidity of the observed phenomenon and therefore an ideal tool for in-situ diffraction studies with time constants even below a second.

3. The Hydrothermal Autoclave for Neutron Diffraction (HAND)

The hydrothermal autoclave for neutron diffraction was designed to be a simple and cheap reaction cell fitting to the well-established ILL D20 [Walton and O'Hare, 2000; Hansen et al., 2008] station with its vanadium furnace. Changes of samples and apparatus must be possible fast and easy. Therefore the apparatus is mainly an upright steel tube closed at both ends. The steam necessary for the hydrothermal reaction is generated inside this tube during heating, so no separate steam supply is needed. The material chosen for the autoclave is cobalt-free stainless steal (4301, Linster, Aschau). The thickness of the walls is a compromise between the demands of a stability at an internal pressure of up to 40 bars and the aim to obtain a maximum penetration of the neutron beam. The schematic diagram of the

reaction cell is given in Figure 2. HAND consists of three parts: bottom, sample support and cover. The bottom is fixed inside the vanadium furnace device below the neutron beam. It serves as reservoir for D_2O and contains the bushings for the internal thermocouples. Inside the bottom the sample support is placed above the water reservoir. The cover is a tube of 14 cm in length and 2.5cm in diameter which is closed at the upper end. It is simply screwed upon the bottom and can easily be replaced. Its walls have a narrowing down to 1 mm at the level of the neutron beam to maximize the intensity of the neutron flow through the sample. During the first experiments HAND was equipped in addition with a valve to evacuate the interior but following experiments have shown that this is not necessary. In Contrary the valve on top causes problems with leak tightness. Therefore we decided to remove it in the new version (see Fig 2)

HAND is mounted in the vertical axis of the diffractometer inside the furnace device available at the instrument D20. Due to the geometric arrangement of the there existing neutron option (fig. 1) the lower limit of the 2Θ range is 8° using HAND with a sample diameter of 20 mm. Below this angle the obligatory beamstop cuts of the diffracted intensity.

4. Experimental

To proof the applicability of HAND we have chosen the pure system $CaO\text{-}SiO_2\text{-}D_2O$ to be studied first. D_2O instead of H_2O was chosen due to the lower interaction between deuterium and neutrons. The fast and easy sample preparation allows us to add different additives to the system easily. The bulk composition was set to a molar Ca/Si ratio of 0.5 projecting on the join tobermorite-quartz and a chosen D_2O/solids ratio of 0.8 resembles the recipes of industrially manufactured steam cured building materials [Fehr and Zuern, 2000].

The starting materials were mixed with mortar and pestle, the compound was poured into a mold (diameter 2cm, height 8cm) and then dried for 1 hour at 60°C to obtain the mandatory

solidity to place it on the sample support. For detailed description of used materials and sample preparation it shall be referred to the studies of Fehr and Zuern (2000) and Bernstein and Fehr (2010).

The temperature of the sample is controlled and monitored with thermocouples using a WEST controller. To determine the temperature gradient through the autoclave-cross-section an additional thermocouple was fixed on the exterior of HAND. Due to the sensitivity of hydrothermal reactions to temperature this is of great importance. Therefore the adjustment control parameter were optimized so that the desired temperature was reached after 1 hour and kept constant for 8 h of reaction time. The rather high background from heavy water and the presence of semi-crystalline phases demands good counting statistics Therefore the typical acquisition time for one powder pattern was set to one minute.

To observe a d-spacing up to 11.3 Å, where the (002) reflection of the evolving tobermorite is expected, the wavelength was set on 2.4 Å instead of 1.3 Å (highest flux). The option of 10' Soller collimators was abandoned, as this would decrease the intensity by a factor of four without an enormous gain in angular resolution. This is mainly limited by the large sample size [Caglioti et al., 1958].

5. Results

Until now HAND was used for several beam times at ILL to perform experiments under different conditions. The detailed description and discussion of the experiments was not the main scope of this paper and for further information we would like to draw the attention on other publications of our workgroup [Fehr & Zuern, 2000; Bernstein & Fehr, 2010]. The maximum reaction temperature of 190 °C was reached after 60 minutes of up heating (see fig. 3). The monitoring of the inner and outer thermocouple reveals an accuracy in sample temperature of ± 0.5°C depicted at the bottom part of figure 3. The homogeneity of the

sample cross-section and in the field of the incoming beam was verified by electron microprobe analyses. The reproducibility of standard analyses was <1% for each element routinely analysed.

The expense of the initial solid phases quartz and portlandite with the reaction time and the formation of 1.13 nm tobermorite can be observed by the decrease of their Bragg-peaks in the time-resolved neutron diffraction pattern as demonstrated in Fig. 4 within the range of 40° to 55° 2-Θ.

Sequential fitting of multiple, individual Bragg-peaks of every powder pattern were performed by a procedure programmed to perform this task from inside the 'Large Array Manipulation Program' (LAMP, *http://wwwold.ill.fr/data_treat/lamp/lamp.html*), the data-visualization and treatment system used at ILL. To take correctly into account the asymmetry due to the 'umbrella'-effect of detecting sections of the Debye-Scherrer cones with a linear PSD of a certain height, the correction of Finger *et al.* [1994] was applied to the data. The instrumental peak-shape of a Bragg-peak was described using a pseudo-Voigt function. The main diffraction peak of iron (mantle of HAND) did not interfere with any peaks of the phases of the sample and was used to calibrate the intensities of the phases of interest. The decrease of the calibrated intensities of quartz and portlandite is depicted in Fig. 4. After 200 min. portlandite was dissolved completely, but crystallization of 1.13nm tobermorite did not start until 331 min. at 190°C. The amount of quartz did not remain constant after the consumption of complete portlandite, indicating a reaction of quartz and initially formed semi-crystalline Ca-rich C-S-H. The first detectable reflections of tobermorite were those of (hk0) planes, (00l) reflections follow with a time lag of about 60 minutes (see fig. 5).

6. Discussion

The high flux instrument D20 provides a time resolution of one minute for recording one diffraction pattern with a good peak/background ratio. Each single diffractogram allows an

exact determination of the amount of phases and the decrease or increase of phases. The low scattering of the data on the amount of phases involved indicates, that a detailed kinetic modeling (e.g. using the model of Chan *et al*. [1978] or an Avrami-equation [Shaw et al., 2000] is possible on data obtained by HAND experiments.

The steel used for HAND remains chemically inert during an experiment. An autoclave cell, designed for D1B diffractometer at ILL by Polak et al. [1990], consisted of aluminum. Synthesis of CSH-phases in a hydrous atmosphere takes place at high pH-values (>12). At such conditions metallic aluminum does not behave chemically inert and will be dissolved. The presence of Al-ions in the system will change the reaction mechanism of 1.13 nm tobermorite formation [Huber et al., 1998; Mitsuda and Taylor, 1975; Klimesch and Ray, 1999, Bernstein and Fehr. 2010]. In addition, Al^{3+} is substituted for Si^{4+} in the tobermorite structure and the intra-crystalline order state of 1.13nm tobermorite will be changed resulting in an increase of the reaction rate [Fehr et al., 2003]. The steel used for HAND has the advantage to behave chemically inert and derived kinetic data correspond to the pure system SiO_2-CaO-D_2O. Furthermore, steel is a material cheap and easy to handle in contradiction to gold-coated Ti-Zr alloys used by Walton et al.[1999].

. The detailed compilation of information obtained by HAND-experiments leads to a better insight in the reaction kinetics and mechanisms of CSH-formation. Until now a large number of experiments has successfully be performed studying the pure system and the influence of different ions like Al^{3+}.or a varrying grain size of quartz [Fehr and Zuern, 2000; Bernstein and Fehr, 2010] Beyond that, this autoclave offers a multitude of other possible applications in Geo.- and Material sciences. The mature design of HAND allows an easy adaptation on powder diffraction devices of other neutron sources assumed that they can provide a sufficient neutron flux.

References

1. Journal article

BERNSTEIN, S.; FEHR, K.T. (**2010**), "The Formation of 1.13nm Tobermorite under Hydrothermal Conditions:1. The influence of quartz grain size within the system CaO-SiO_2-D_2O" *Progress in Crystall Growth and Characterization of Materials , **accepted***

CAGLIOTI, G., PAOLETTI, A. and RICCI, F.P. (**1958**), "Choise of collimators for a crystal spectrometer for neutron diffraction" Nucl. Instr. and Meth. **35** 223-228.

CHAN, C.F., SAKIYAMA, M. and MITSUDA, T. **(1978)**, "Kinetics of CaO-Quartz-H_2O reaction at 120°C in suspension" *Cem. Con. Res*. **8,** 1-6.

FINGER, L.W., COX, D.E. and JEPHCOAT, A.P. (**1994**) "A correction for powder diffraction peak asymmetry due to axial divergence," J. Appl. Cryst. **27**, 892-900.

GABROVSEK, R., KURBUS B., MUELLER D. and W. WIEKER **(1993)** "Tobermorite formation in the system CaO, C3S-SiO2-Al2O3-NaOH-H2O under hydrothermal conditions," *Cem. Con. Res.* **23,** 321.

HANSEN, T.C.; HENRY, P.F., FISCHER, H.E. (**2008**), "The D20 instrument at the ILL: a versatile high-intensity two-axis neutron diffractometer," Measurement Science & Technology.

KLIMESCH, D.S and RAY, A.S. (**1999**), "Effect of quartz content in the nature of al-substituted 11A tobermorite in hydrothermaly treated CaO-Al2O3-SiO2-H2O system," *Advanc. Cem. Res.* **11**, 179.

MITSUDA T. and TAYLOR, H.F.W. (**1975**) "Influence of aluminum on the conversion of calcium silicate hydrate gels into 11Å tobermorite at 90° and 120°,"*Cem. Con. Res.* **5,** 203-210.

POLAK, E., MUNN, J., BARNES, P., TARLING, S.E. and RITTER, C. (**1990**), Time-resolved neutron diffraction analyses of hydrothermal Synthesis using a novel autoclave cell," *J. Appl. Cryst.* **23,** 258-262.

SHAW, S, CLARK, S.M. and HENDERSON, C.M.B. (**2000**) "Hydrothermal formation of the calcium silicate hydrates, tobermorite ($Cs_5Si_6O_{16}(OH)_2$) 4H2O and xonotlite ($Ca_6Si_6O_{17}(OH)_2$): an in situ synchrotron study,"*Chem. Geol*. **167,** 129-140.

WALTON, R.I., SMITH, R.I., MILLANGE, F.,. CLARK, I.J,. SINCLAIR D.C and O'HARE, D. (**2000**), An in-situ time resolved neutron diffraction study of the hydrothermal crystallisation of barium titanate," *Chem. Commun.* **14,** 1267 – 1268.

WALTON, R.I. and O'HARE, D. **(2000)**, Watching solids crystallise using in situ powder diffraction, Chem. Commun. **23,** 2283 – 2291.

WALTON, R.I., FRANCIS, R.J., HALASYAMANI, P.S., O'HARE, D., SMITH, R.I., DONE, R. and HUMPHREYS, R.J. (**1999**) Novel apparatus for the in situ study of hydrothermal crystallizations using time-resolved neutron diffraction, Rev. Sci. Instr. **70**, 3391.

2. Selections from an anthology

FEHR, K.T. and ZUERN, S.G. **(1997)**, "Phase relations of 1.13 nm tobermorite, xonotlite, truscottite and gyrolite under hydrothermal conditions," in Proc. 5th Int. Symp. Hydrotherm. Reactions, 225-227.

FEHR, K.T. and ZUERN, S.G. **(2000)**, Mechanisms of calcium-silicate-hydrates under hydrothermal conditions," in Proc. 6th Int. Symp. Hydrotherm. Reactions, 278-281.

FEHR, K.T; HUBER, M.; ZÜRN, S.G. and PETERS E. (2003): Determination of the reaction kinetics and reaction mechanisms of Al-tobermorite under hydrothermal conditions by in-situ neutron diffraction. In FENG, S.H.; CHEN, J.S. & SHI, Z. (eds.): Hydrothermal Reactions and Techniques. World Scientific, New Jersey, 19-26

HUBER, M., FEHR, K.T. and ZUERN, S.G. (**1998**), Kinetische Studien zur Bildung von 1.13 nm Tobermorit unter hydrothermalen Bedingungen," in: Bauchemie von der Forschung bis zur Praxis", Monogr. 11 d. GDCh , 29-32, edited by W. Hiller.

ZUERN, S.G. and FEHR, K.T. (**2000a**), "Phase relations and thermodynamic properties of 1.13 nm tobermorite and xonotlite," in Proc. 6th Int. Symp. Hydrotherm. Reactions, 286-289.

3. Computer programs

LAMP, The Large Array Manipulation Program. *http://wwwold.ill.fr/data_treat/lamp/lamp.html*

Figure captions

Figure 1 Schematic diagram of the setup on the ILL D20 station

Figure 2 Schematic diagram of the HAND reaction cell (vertical section).

Figure 3 Cumulative distribution ($\mathbf{Q_3}$) and density distribution ($\mathbf{q_3}$) of quartz grainsize

Figure 4 Time resolved neutron diffraction pattern in the 2-Theta range 40 – 55 ° at T = 190°C.Time resolution is one minute.

Figure 5 Variation of the integral intensity of portlandite (●)and quartz (○) and the maximum intensity of tobermorite (002) (∗) with time, temperature profile for the experiment is shown in the lower part of the diagram.

Figure 6 occurrence of (hk0) and (00l) reflections in the course of the experiment

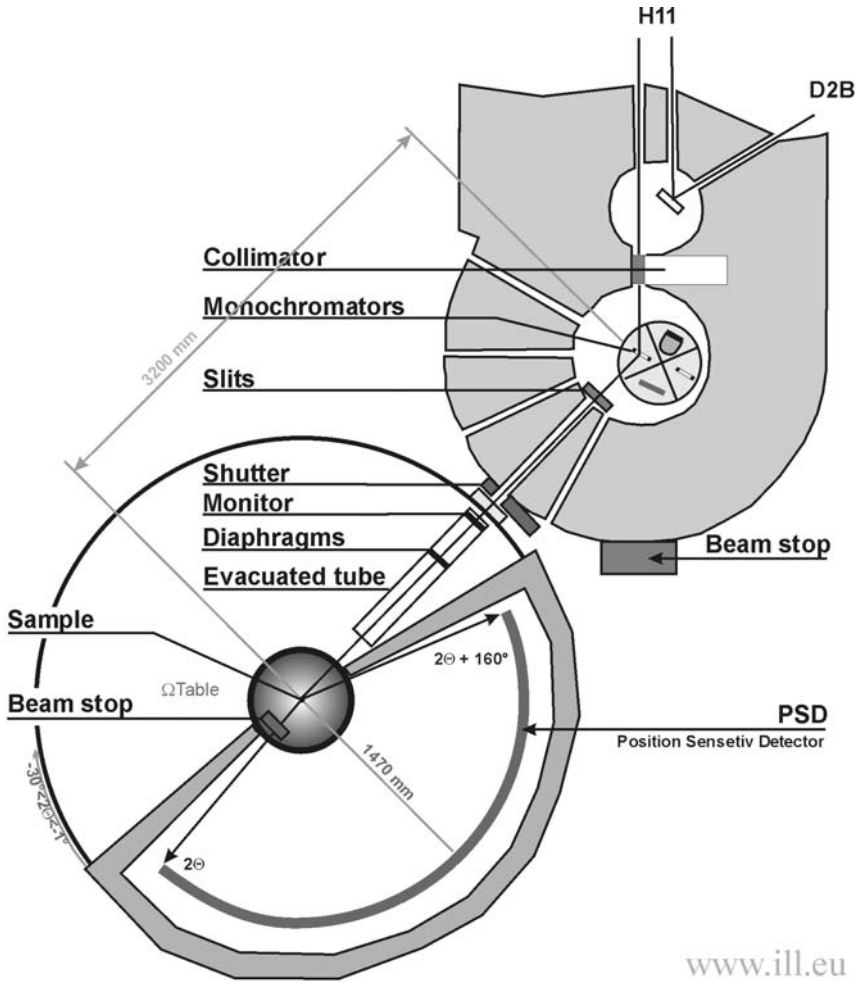
H11
D2B
Collimator
Monochromators
3200 mm
Slits
Shutter
Monitor
Diaphragms
Evacuated tube
Beam stop
Sample
2Θ + 160°
ΩTable
Beam stop
PSD
Position Sensetiv Detector
1470 mm
-30° <2Θ<-1°
2Θ
www.ill.eu

Figure 1

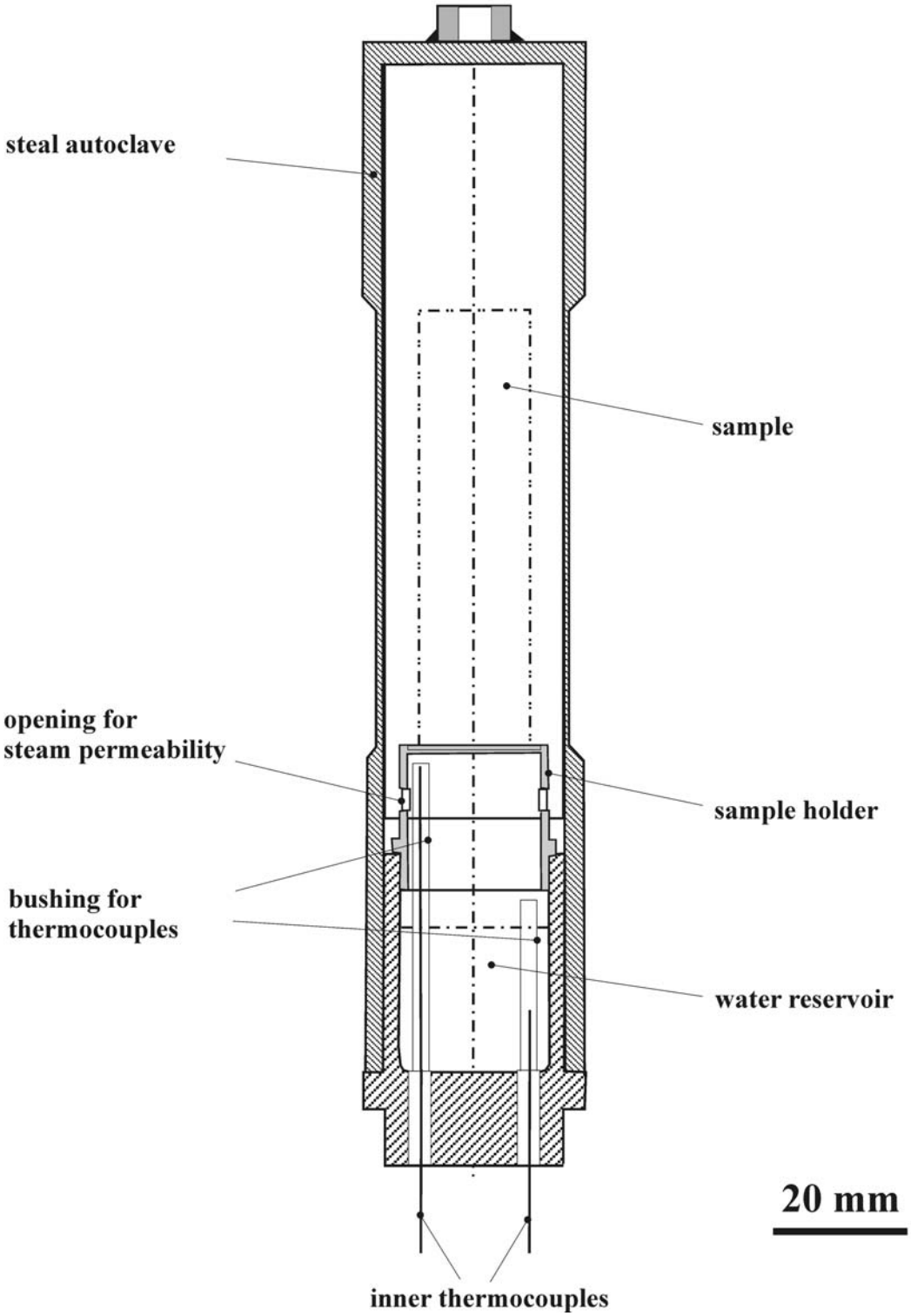
steal autoclave
sample
opening for
steam permeability
sample holder
bushing for
thermocouples
water reservoir
20 mm
inner thermocouples

Figure 2

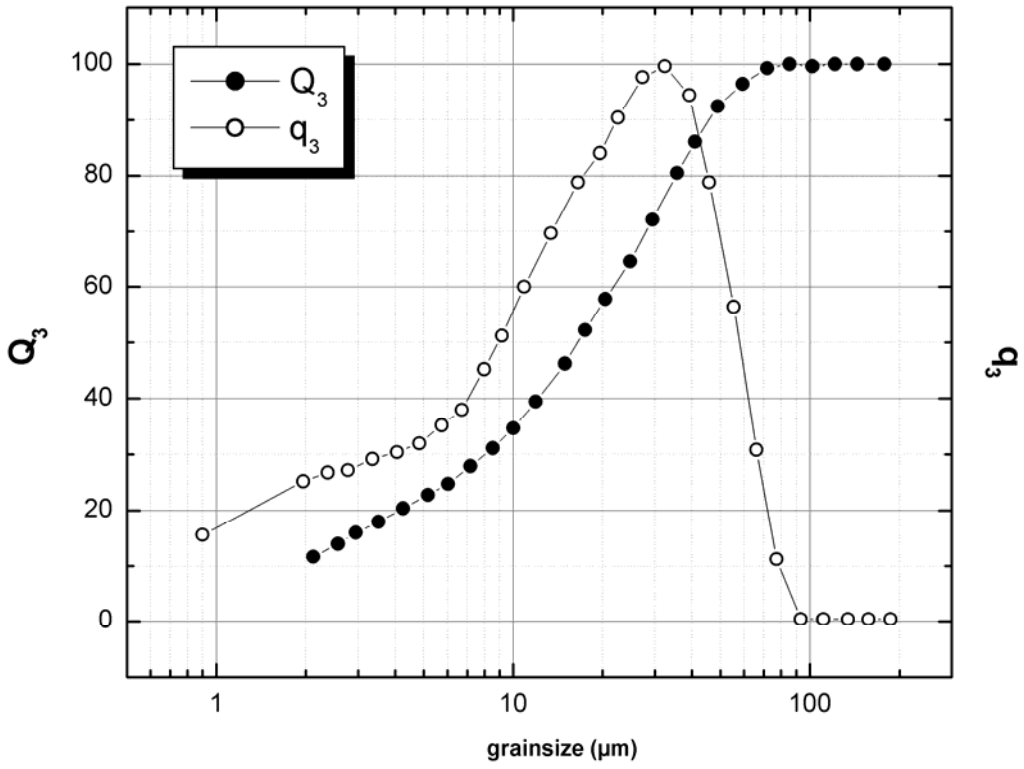

Figure 3

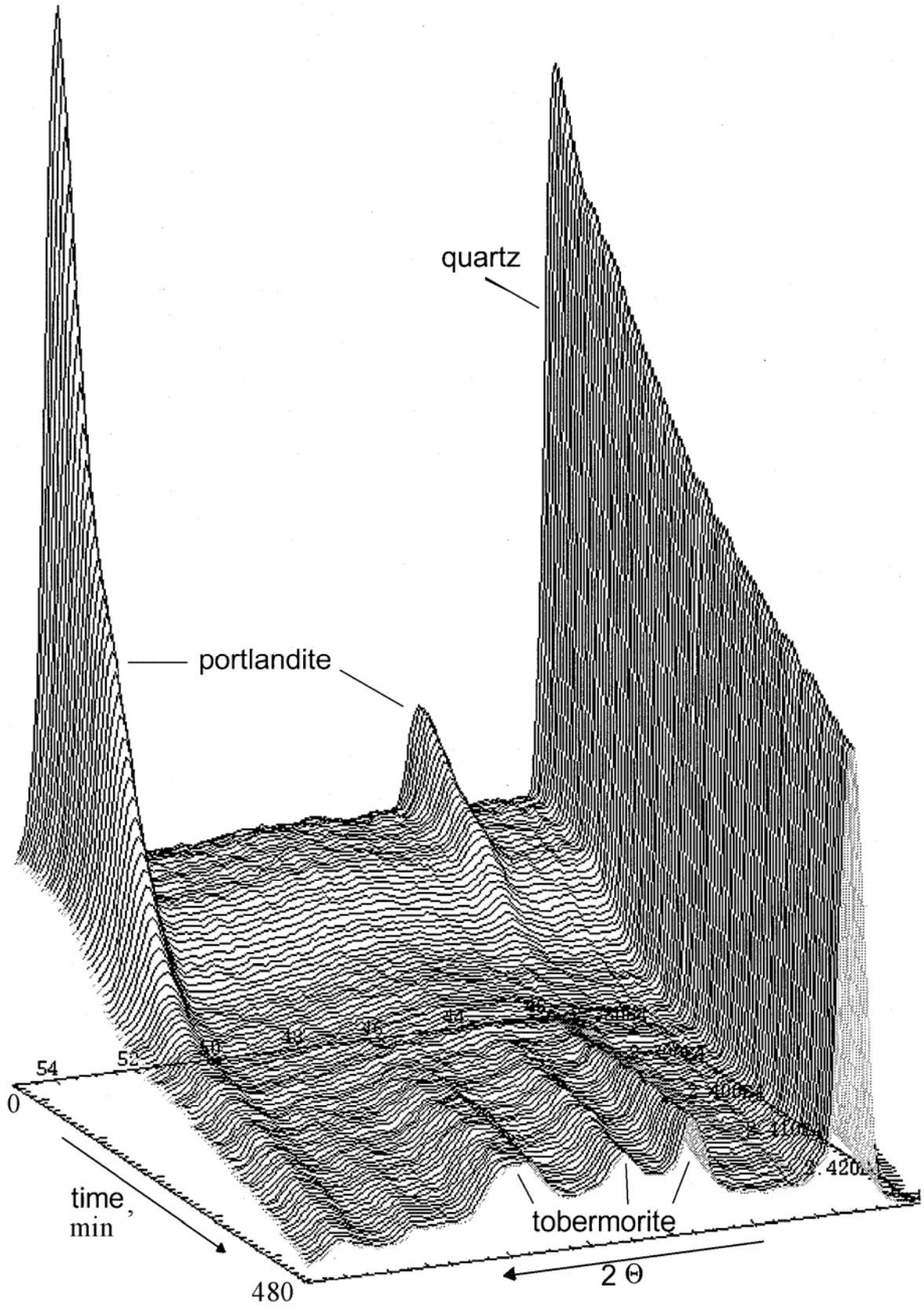
quartz
portlandite
tobermorite
time, min
0
480
2 Θ
54
52
50
48
46
44
42
40
38
36
34
32
30
28
26
24
22
20

Figure 4

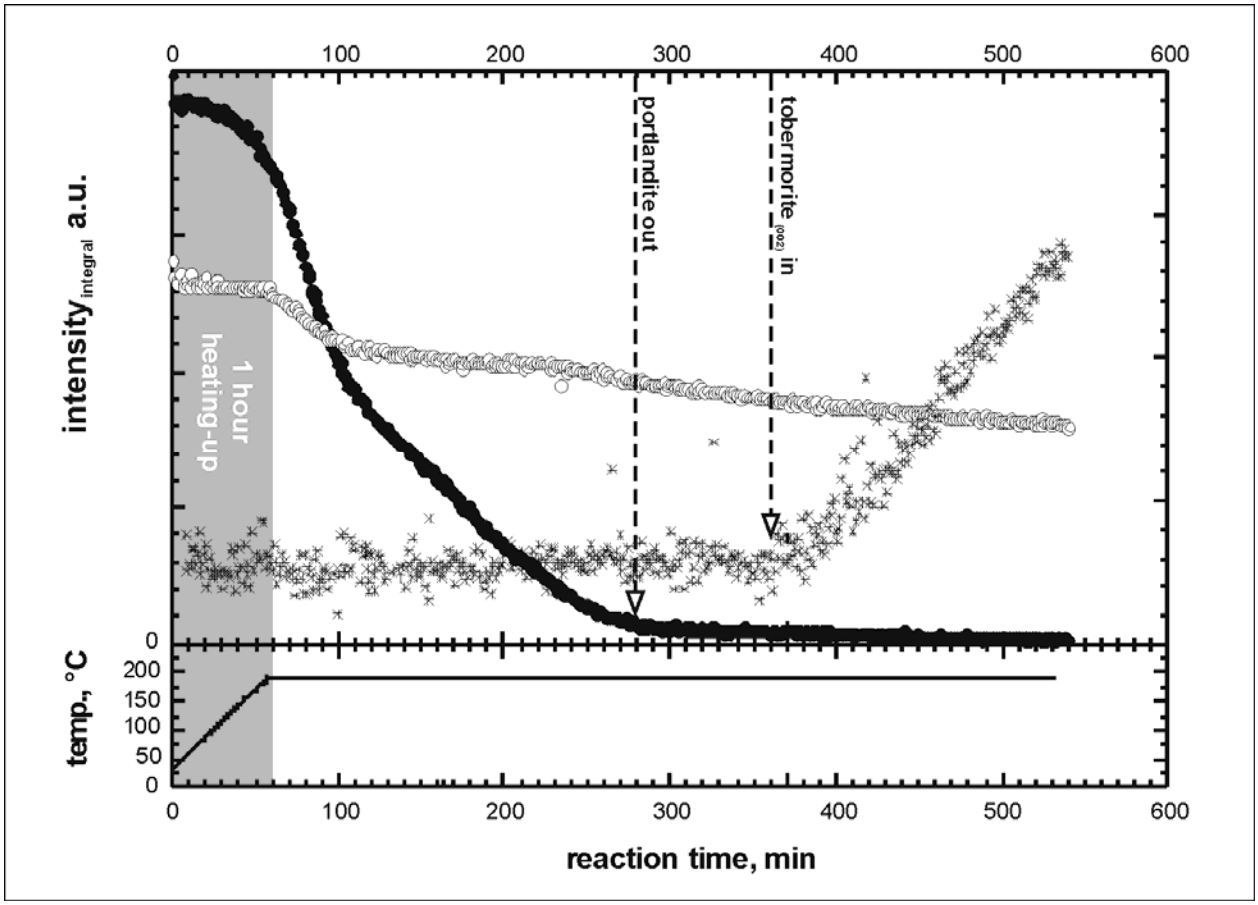
intensity integral a.u.
1 hour heating-up
portlandite out
tobermorite (002) in
temp., °C
reaction time, min
0
100
200
300
400
500
600
50
150

Figure 5

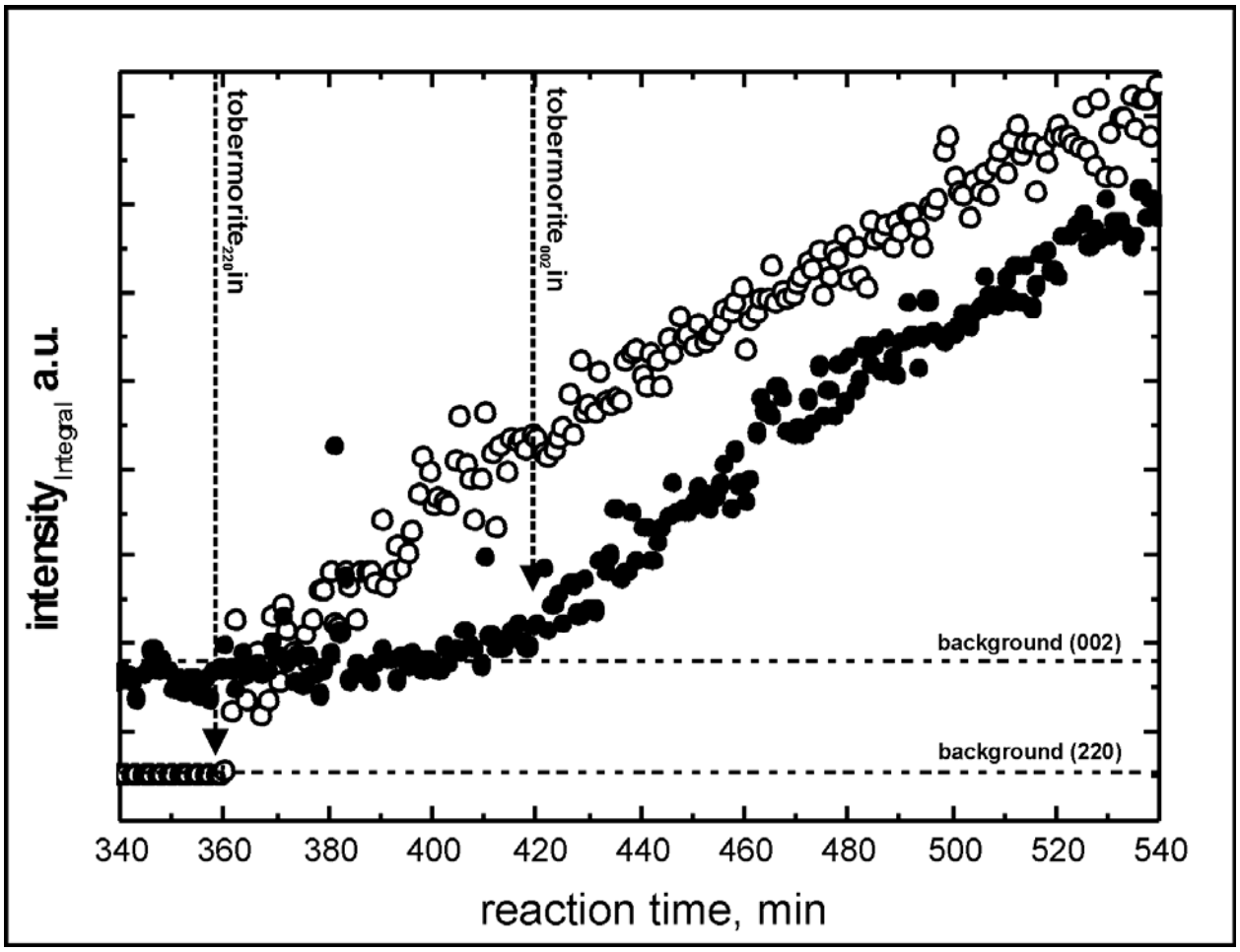
tobermorite220in
tobermorite002in
intensityIntegral a.u.
background (002)
background (220)
340
360
380
400
420
440
460
480
500
520
540
reaction time, min

Figure 6

Appendix D

The Formation of 1.13nm Tobermorite under Hydrothermal Conditions:
1. The influence of quartz grain size within the system $CaO\text{-}SiO_2\text{-}D_2O$
Progress in Crystall Growth and Characterisation of Materials, in press

The Formation of 1.13nm Tobermorite under Hydrothermal Conditions:

1. The influence of quartz grain size within the system $CaO\text{-}SiO_2\text{-}D_2O$

S. Bernstein[a,*], K.T. Fehr[a]

[a]*Ludwig Maximilians University, Department of Earth and Environmental Sciences, Theresienstraße 41/III, 80333 Munich, Germany*

1. Abstract

The influence of grain size of quartz on the formation of 1.13nm tobermorite in aerated autoclaved concrete was investigated by applying in-situ neutron diffraction. Experiments were performed at 210°C/P_{sat} employing quartz of 8µm and 16µm, respectively. The results reveal changes in the reaction mechanism from solution control to diffusion control. The grain size of the quartz fraction clearly influences the occurrence of those changes. Based on those results an interpretation of former not clearly interpretable quenching experiments was performed. An interpretation using different reaction mechanisms for those experiments leads to a coherent picture of the reaction.

Keywords: 1.13nm tobermorite, kinetic, aerated autoclaved concrete, in situ neutron diffraction

1. Introduction

Calcium Silicate Hydrates (CSH-phases) are very rare in nature but one deploys their properties in several technical applications. Up to now the main scope lies in the production of steam cured building materials. For the fabrication of aerated autoclaved concrete (AAC),one of the most popular building materials in Europe for lightweight mode of construction, 1.13 nm tobermorite is the predominant phase. The evolved crystal texture mainly controls the mechanical and thermal properties of the product, like high pressure resistance and low thermal conductivity.
1.13 nm tobermorite crystallizes in a layered structure, stacked along [001] with a basal spacing of 1.13 nm. The average structure was described by Hamid [1] but the real structure was solved by Merlino et al. [2,3] which is based on two polytypic modification of orthorhombic and monoclinic symmetry leading to a disordered structure (O/D character). The common structural feature is characterized by infinite silicate double chains of a type called Dreierdoppelketten built up of condensed dreierketten (kinked to repeat at intervals of

three tetrahedra) along [010]. The chains are intercalated by a Ca-O layer (portlandite layer) so the structure consists of a central layer of calcium octahedra which has silicate sheets on each side. The calcium octahedra share oxygens with the silicate tetrahedra, the distance between two edges in the calcium octahedral layer is about the same length as a silicate dreierketten unit. This type of structural unit is characteristic for most of all CSH-phases. In 1.13nm tobermorite the composite layers of one calcium and two silicate layers are bound together by an interlayer containing calcium ions and water molecules. The interlayer contains variable amounts of calcium so that charge balance is achieved by variation of hydrogen atoms bonded to the silicate chains. Therefore, the variable occupancy of calcium in these layers allows the Ca:Si ratio to vary from $Ca_5Si_6O_{16}(OH)_2 *4H_2O$ ($C_5S_6H_5$) to $Ca_4Si_6O(OH)_2 *2H_2O$ ($C_4S_6H_3$) [2,3]. In AAC, 1.13nm tobermorite is close to the composition $Ca_5Si_6O_{16}(OH)_2 *4H_2O$ and occurs in association with semi-crystalline CSH-phases CSH (I) and CSH (II) as minor components. In contrast to tobermorite these phases are highly disordered and display a wide range of compositions. They are classified by their Ca:Si ratio: CSH (I) with a Ca:Si ratio <1.5 and CSH (II) with a Ca:Si ratio > 1.5 according to Taylor [4,5].
There has been a lot of work in this field aimed at understanding the formation mechanisms and growth kinetics of CSH-phases [e.g.6,7]. But little quantitative data exist on the kinetics of 1.13 nm tobermorite formation. In addition there is no accordance on the nature of the reaction mechanism because some studies proposed being solution controlled and others being diffusion controlled as pointed out in detail by Klimesch et al. [8].
The reaction mechanism and kinetics of the formation of 1.13 nm tobermorite in the pure cement-free system $CaO\text{-}SiO_2\text{-}H_2O$ from lime, silica and water ($CaO + SiO_2 + H_2O$) under hydrothermal conditions were determined by quenching experiments at 180°-190°C/Psat [5,6,9] and by an in-situ Neutron diffraction experiment [10] as well. Quenching experiments reveal the disadvantage of missing data for the early evolution of phases in time and have prevented a quantitative kinetic description so far.
The formation of tobermorite is, in addition to reaction temperature and the amount of Al in the initial mixture, mainly affected by the grain size of quartz [8,11] .Therefore, the major aim of this investigation was to determine reaction mechanism and kinetics of the formation of 1.13 nm tobermorite under hydrothermal conditions as a function of the grain size of quartz. Experiments were conducted at 210°C employing quartz with a grain size of 8µm and 16 µm, respectively. In order to avoid quenching effects in short-time runs the experiments were conducted at in-situ conditions and data will be collected by means of neutron-diffraction with the HAND apparatus [12].

3. Experimental

In-situ experiments under hydrothermal conditions were conducted at 210°C under saturation pressure and within a time-range of up to 10 hours by applying a hydrothermal autoclave cell for neutron diffraction HAND [12] at the D20 powder diffractometer of the high-flux neutron-source ($4.2* 10^7$ n cm^{-2} s^{-1}) at Institute Laue-Langevin (ILL), Grenoble. In order to obtain neutron diffraction spectra with a low background noise, hydrogen-free substances have to be used, and contact of the materials with humidity must be minimized. Thus the experiments were carried out with heavy water (D_2O) instead of H_2O as hydrous reactant. To control the influence of D_2O on the kinetics of the tobermorite-forming reaction two preliminary quenching experiments were conducted in cold seal pressures vessel at 190°C/P_{sat} for 8 hours, using D_2O and H_2O as hydrothermal fluid, respectively. Analyses of the final products by X-rax diffraction demonstrate no differences between both runs as indicated by similar phase assemblages and phase amounts.
Pure SiO_2, CaO and D2O were used as starting materials in order to determine the reaction kinetics in the simple system $CaO\text{-}SiO_2\text{-}D_2O$ according to the reaction:

$$5CaO + 6SiO_2 + 5H_2O \Rightarrow Ca_5Si_6O_{16}(OH)_2 * 4H_2O \quad (1)$$

CaO used was produced by heating calcium carbonate (Merck p.a.), having a particle size of <0.090mm at 1250° C for 14 h. The source of SiO_2 was ground Miocene quartz sand (SiO_2 > 99.5 wt.-%) supplied by the Quarzwerke Company in Frechen, Germany, revealing a medium grain size of 8µm (SH500) and 16µm (W12), respectively. Pure deuterium oxide (Merck, Uvasol, D_2O > 99.8 %) was used as liquid reactant. The mixture was prepared at D_2O/solids ratio of 0.8 with a Ca:Si ratio of 0.5.
The experiments were designed to examine in-situ the hydrothermal hardening of lime-silica based samples in the vapour phase and not in suspension like Shaw et al. [13] corresponding to the production process of AAC or lime-silicate bricks. Therefore the initial specimen has to reveal a mechanical stability that is great enough to be placed on the sample support. For this purposes the raw materials were mixed using mortar and pestle to obtain a homogeneous paste. The mass was poured into a previously prepared paper wrapper (diameter 1.5 cm, height 8 cm) and stored at 60° C for 120 minutes in a sealed container. The raised temperature resulted in an acceleration of the binding process. After this thermal treatment, the solid and hardened sample was placed on the sample holder in the autoclave. The desired temperature was reached by 1 hour of controlled heating up and then held for the defined length of time (8 up to 10h). The inner and outer temperature of the sample was monitored and regulated with thermocouples inside and on the bottom of the sample. The temperature gradient across as well as along the sample determined in some preliminary tests is 2°C.
The time-resolved neutron diffraction pattern were taken within the range of 8° to 153.6° 2-θ at λ = 2.4 Å to allow the analysis of d-spacing up to 11.3 Å, where the basal (002) reflection of the evolving tobermorite is expected. Due to a rather high background from heavy water and the presence of semi-crystalline phases in the initial steps of the reaction, good counting statistics are necessary. Therefore the typical acquisition time for one powder pattern was set to one minute.
The mechanisms of the tobermorite forming reaction can be evaluated on the basis of the reaction conversion of quartz according to Chan et al (1978)[6] assuming that there are no seeds in the reactants and the growth rate is low:

$$1-(1-\alpha)^{\frac{1}{3}} = kt^{1/n} \qquad (2)$$

where α gives the reaction conversion of quartz, k the reaction constant and t the reaction time. According to equation 2 the factor n reveals information on the reaction mechanism. If n=1 the reaction is solution controlled (phase boundary modell), if n=2 the reaction is diffusion controlled (Jander equation) [14]. Values for α were calculated from the decreasing integral intensity of the (101)-Bragg reflection of quartz. The integral intensity was obtained by using the peakfitting-routine "STR_fit" implemented in the Large Array Manipulation Program (LAMP) provided by the ILL. The diffraction patterns were fitted in the range from 41 to 44 ° 2theta, the peak shape was set to Pseudo-Voigt and a linear background was chosen. By applying equation 2 to these data and plotting them in logarithmic scale, one obtains information on the reaction mechanism from the slope of the data points. The complete expense of portlandite was determined by the disappearance of the (101) reflection at 54.3° 2Θ. The first occurrence of tobermorite was determined by the appearance of (hk0) reflections at 46° 2Θ.

4. Results

The results for the experiments are depicted in Figure 1a) and b). Both experiments don't show a curve linearity but different slopes of 1 and 0.5 within the reaction progress. According to equation (2) the slope of the data points yields information on the reaction mechanism. Therefore the reaction can be split into 3 sections with a diffusion or solution controlled mechanism. The times where the changes in slope occur are labelled here with t_1_transit and t_2_transit respectively. Determined transition temperatures, the moment of portlandite expense and 1.13nm tobermorite occurrence are summarized in Table 1.
For the first experiment (Fig. 1a) a quartz with a mean grainsize of 16µm was used in the initial mixture. The desired reaction temperature of 210°C was reached after 60 min of heating up. Up to 30 min (t_1_transit) after starting the experiment the reaction is solution controlled, followed by a diffusion controlled period. After 228 min a further change back to a solution controlled reaction mechanism can be observed. Portlandite is consumed after 142 minutes of the running experiment within the diffusion controlled section of the reaction. Just after 250 min, within the second solution controlled period, the first reflections of 1.13nm tobermorite could be observed.
On the first glance the second experiment using quartz with a mean grain size of quartz at 8µm shows a similar curve progression. The differences becomes just apart if one compares the transition times and the expense and occurrence of protlandite and tobermorite, respectively. The reaction starts again with a solution controlled segment but the first change to a diffusion controlled mechanism already occurs after 18 minutes (t1_transit). The second change back to solution control is detectable after 180 min, compared to the 16µm experiment almost 50 min earlier. Also the consumption of portlandite after 60 min and the first appearance of tobermorite is accelerated. The transition times, the moment of the expense of portlandit and the occurrence of tobermorite show a clear increasing trend with increasing grain size of quartz (Fig.2)

5. Discussion

In situ neutron diffraction experiments conducted in this study at 210°C with two different grain sizes of quartz revealed a non isokinetic behaviour of the tobermorit forming reaction in AAC. The reaction mechanism changes from solution control to diffusion control and back to a solution controlled segment. The duration of these segments is strongly influenced by the grain size of quartz employed in the initial mixture. If the grain size is decreased to 8µm, the first solution controlled part is reduced from 30 to 18 minutes. Likewise the following diffusion controlled stage is just present up to 180 min (t_2_transit) compared to 228 min (t_2_transit) in the experiment with the coarser quartz. With the finer quartz portlandite is expensed earlier and 1.13 tobermorite can be detected already after 140 min in the diffusion controlled segment of the reaction. Lasaga & Luettge [15] used a modified Gibbs Thomson equation to describe the dissolution of crystals (equation 3).

$$\Delta G = \Delta G^0 + RT \ln a_l / a_s + \sigma \Delta A + u(r) \Delta V \qquad (3)$$

By neglecting the term for the strain field of dislocation defects, this equation can also be used to see the influence of different factors to the formation of 1.13nm tobermorite.
This equation shows the dependence of solubility to the activity (a) of the liquid and the solid reactants and the surface free energy(σ). the surface free energy depends on the grain size of the solids and the activity (a) on the composition of the reactants (in case of tobermorite if Al is added to the system. Equation (3) shows a linear correlation between the solubility and the influencing factors. To generalize this for 1.13nm tobermorite formation, the reaction is constrained by the grain size of the reactants (this study) and the composition of the initial mixture (forthcoming paper)

With the results from this study one can make interpretations in terms of the reaction path. The changing reaction mechanism denote that tobermorite is not formed initially but by an intermediate step. The initial reaction is controlled by the solution of quartz to form semicrystalline CSH-phases. Such phases are evident by a bumb in the background of the diffraction patterns. The second step is controlled by the diffusion of quartz through a layer of semicrystalline CSH-phases and the last step, after the expense of portlandite,is controlled by the reaction of still existing quartz with the CSH-phases to form tobermorite. This is in good agreement with results of Fehr et al. [10]

Quenching experiments conducted in the past [6,7,9] could not be interpreted in terms of a reaction displaying a isokinetic behaviour with just a single slope. Interpretations are often not unambiguous due to a low density of data points. Furthermore information for the initial part of the reaction are missing due to lacking short time experiments.

Based on the results of this study some quenching experiments [6,7,9] were recalculated in terms of reaction conversion of quartz according to equation (2) and reinterpreted. Non-isokinetic reaction mechanisms of the quenching experiments becoming evident by applying the findings from in-situ experiments as demonstrated in Figure 3. the determined transition temperatures are summarized in Table 2. The quenching experiments at 180°C/P_{sat} [6,7] are carried out in the system CaO-SiO_2-H_2O beyond the stability field of 1.13 nm tobermorite [9]. The experiments of Chan et al. [6] were carried out with different Ca:Si ratios (0.8 and 1.0) but there are no differences in reaction mechanism as displayed in Figure 2. Their experiments applying quartz < 10 µm only exhibit a diffusion controlled mechanism and higher values for the reaction conversion of quartz (α) compared to the results on 8 µm-quartz used by Klimesch & Ray [7] as shown in Figure 3. The reaction mechanism for 8 µm-quartz [7] is solution controlled up to 5.0 hours (t_3_transit time) followed by diffusion control and indicating an estimated t_2_transit time below 1 hour.

The reaction mechanism for 16 µm-quartz [6] is solution controlled up to 5.2 hours (t_3_transit time) followed by diffusion control and indicating an estimated t_2_transit time below 1.5 hours. Finally, the reaction mechanism for 35 µm-quartz [7] is diffusion controlled up to 2.1 hours (t_2_transit time) followed by solution control up to 7.2 hours (t_3_transit time) reaching diffusion control at the final stage.

The quenching experiments at 190°C/P_{sat} [9] are carried out in the system CaO-SiO_2-H_2O beyond the stability field of 1.13 nm tobermorite [9] and this phase crystallizes metastable. The quartz used in these experiments displays a grain size of 45 µm [9]. The reaction mechanism for 45 µm-quartz is diffusion controlled up to 6 hours (t_2_transit time) followed by solution control up to 9.8 hours (t_3_transit time) ending in diffusion control at the final stage. Summarizing the quenching experiments at 180°C/P_{sat} [6,7] no t_1_transit time dividing solution from diffusion control can be observed due to the lack of short-time experiments. Two additional transition times occur dividing diffusion from solution control (t_2_transit time) and finally solution from diffusion control (t_3_transit time).

Comparing the transition times from experiments with different grin sizes of quartz the same increasing trend with increasing grain size becomes apparent as shown in Figure 4.

The reaction temperature seems to have just a minor influence on the reaction mechanism though data from experiments with different temperatures are compareable and are plotted in one diagram (Fig.3).

Experiments with quartz < 10µm at 180 °C [6] just show a slope indicating a diffusion controlled mechanism. for the early stage of the reaction, where solution controlled mechanism is expected, no data are available thus one can just assume the same progress as found for experiments performed by Klimesch & Ray [7]. In addition data from Chan et al [6] show higher values for the reaction progress then the one from Klimesch & Ray [7]. This could be ascribed to the different upheating and the different water /solid ratios in the experimental setup. Data from the experiment with 35mm quartz at 180 °C are ambiguous but

transition times were constructed with regard to the results from in situ experiments. As the initial step of the reaction is very fast and the density of data points obtained by quenching experiments is low the t_1_transit time can not be determined from those but an additional change from solution to diffusion control (t_3_transit) can be assigned. Due to lacking data for short time experiments at 180°C with a quartz grain size of 8µm [7] and 10-20µm [6], t_2-transition times where estimated to be under 0.8 and 1.4h respectively. Comparing the results for different grain sizes of quartz one can observe the same trend of decreasing transition times with increasing grain size of quartz (Fig.4) as found by in situ experiments of this study. The t_2_transit times obtained by quenching experiments are much lower than the one from in-situ experiments. This can be assigned to the different calcination temperatures for the CaO used. There is a strong influence of the calcination temperature to the reactivity of CaO as shown by .Moropoulou et al. [16]. As the reaction is solution driven, the solution of the reactants plays an important role for the reaction progress. The solution (reactivity) is for both reactants quartz and CaO is primarily influenced by their specific surface area but for CaO the reactivity is additionally increased by lower calcination temperatures.

6. Conclusion

The formation of 1.13 tobermorite in AAC can be described as a non isokinetic reaction. One can observe changes in the reaction mechanism between solution and diffusion controlled when plotting the reaction conversion of quartz against reaction time in terms of equation (2). Based on experiments conducted at 210°C with two different grain sizes of quartz it could be shown that a finer quartz fraction is decreasing the several transition times and therefore accelerating the reaction due to an increase in reactivity. The moment of portlandite expense and 1.13 tobermorite occurrence and the related change in reaction mechanism could be assigned to the reaction path. 1-13nm tobermorite is not formed initially but by an intermediate step of semicrystalline CSH-phases.
The effect of decreasing transition temperatures when using a smaller grain size of quartz was also detectable in quenching experiments (6,7) after recalculating them by applying equation (2). The 1.13 nm tobermorite forming reaction is mainly controlled by the solubility of the involved phases and their speciation. This solubility is influenced by the specific surface area of the reactant and in case of CaO on the calcination temperature.

* **corresponding author:** Tel.: +49 89 2180 4276; fax: +49 89 2180 4176
email address: bernstein@min.uni-muenchen.de

References

[1] S.A. Hamid, Z. Krist. 154 (1981) 189.
[2] S. Merlino, E. Bonaccorsi and Th. Armbruster, Amer.Miner. 84 (1999) 1613.
[3] S. Merlino, E. Bonaccorsi and Th. Armbruster, Eur. J.Min. 13 (2001) 577.
[4] H.F.W. Taylor, J. Chem. Soc. 30 (1950) 82.
[5] H.F.W. Taylor, Proc. Vth Int. Symp. Chem. Cem. Vol II (1968) 1.
[6] C. F.Chan, M. Sakiyama and T. Mitsuda , Cem.Concr.Res. 8 (1978) 1.
[7] D. S. Klimesch and A.Ray , J.Therm.Anal.Calorim. (2002) 995.
[8] D. S. Klimesch and A.Ray and B.Sloane , Cem.Concr.Res. 26 (1996) 1399.
[9] S.G. Zuern and K.T. Fehr., Proc. Joint ISHR & ICSTR, Kochi (2000) 286.
[10] K.T. Fehr, M: Huber, S.G. Zuern and T. Hansen, *Proc. 5th ICSTR* (2002) 37.

[11] N.Isu, H. Ishida and T. Mitsuda , Cem.Concr.Res. 25 (1995) 243-248

[12] S.G. Zuern, K.T. Fehr and T. Hansen, Proc. 5th ICSTR (2002) 33-36

[13] S. Shaw, S.M. Clark and C.M.B. Henderson, Chem. Geol. 167 (2000) 129.

[14] J.D. Hancock and J.H. Sharp, J. Amer.Ceram.Soc. 55 (1972) 74.

[15] C. Lasaga and A.Luettge, Eur.J.Mineral. 15 (2003) 603.

[16] A. Moropoulou, A. Bakolas, E. Aggelak, Cem.Concr.Res.31 (2001) 633.

Tables

Table 1: net weight, determined transition times and points of portlandite out and tobermorite in

experiment.	W12 g	SH500 g	CaO g	t_1 min	t_2 min	portlandite out	tobermorite in
W12_210	16	-	8	30	228	142	250
SH500_210	-	16	8	18	180	60	140

Table 2: employed grain size of quartz and reaction temperatures and determined transition times of recalculated quenching experiments from literature

experiment	grain size (µm)	temperature (°C)	t_2 (h)	t_3 (h)
K&R02 [1]	8	180	~0.8	5.0
K&R02 [1]	35	180	2.1	7.2
C&M78 [2]	16	180	~1.4	5.2

[1] Klimesch &Ray (2002) [7]; [2] Chan et al. (1978)[6]

Figures:

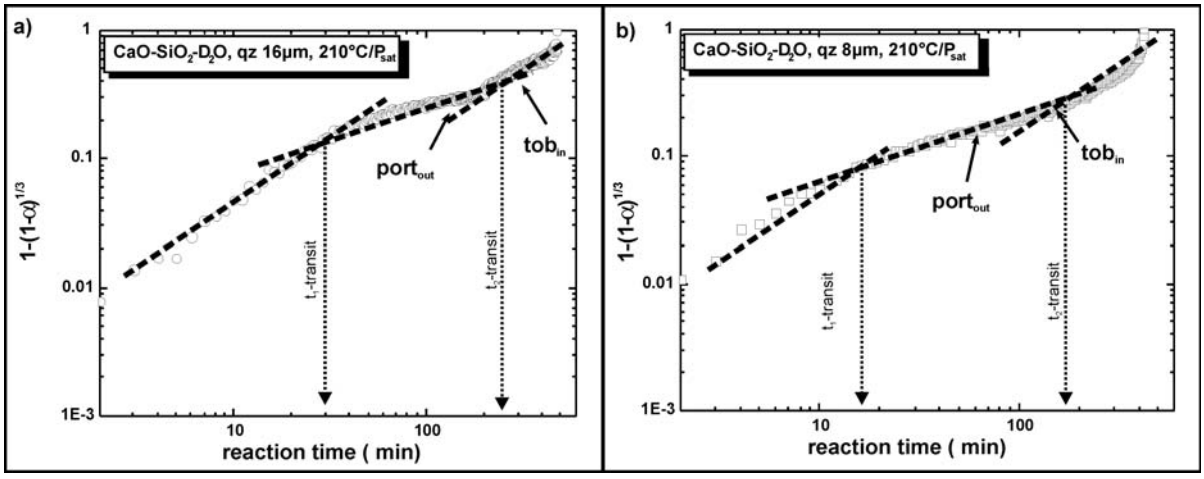

Figure 1:
Reaction conversion of quartz in the system CaO-SiO2-D2O at 210°C/Psat and employing quartz of 16µm (a) and 8µm (b) according to equation (2)

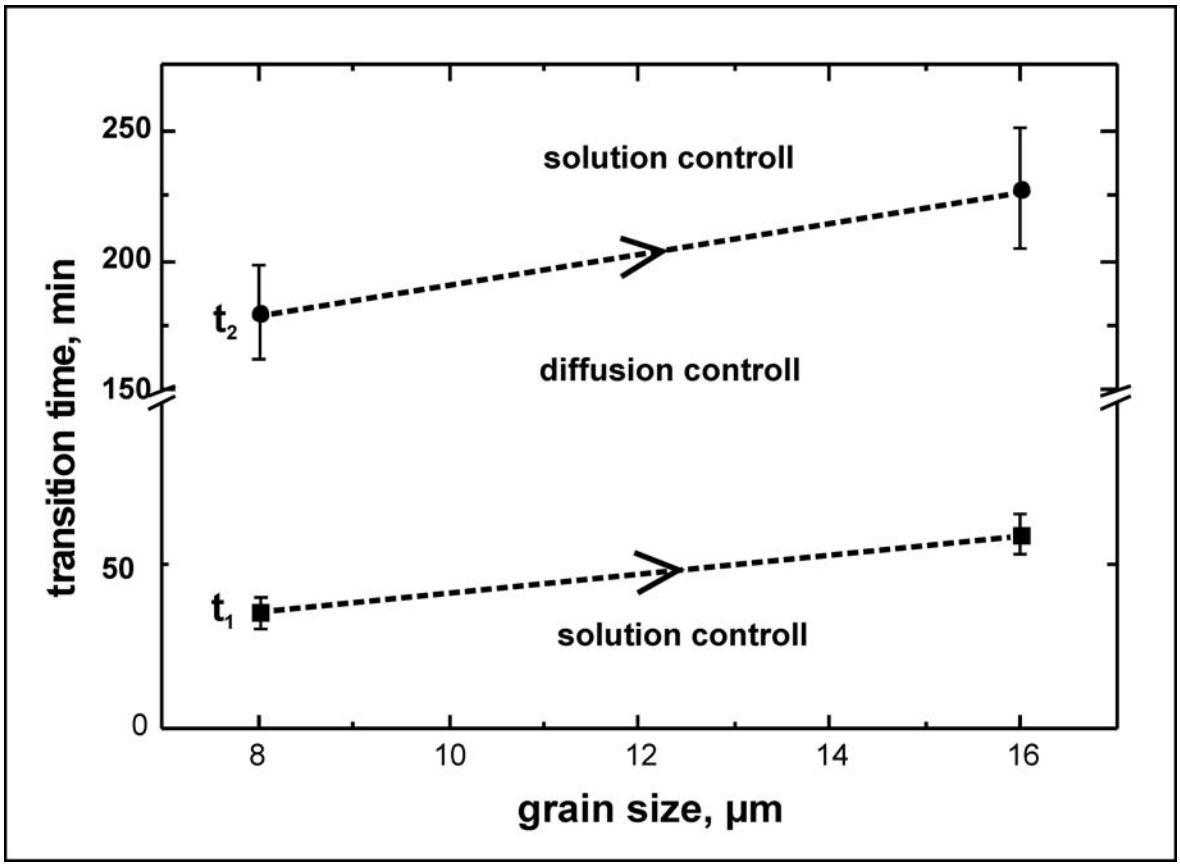

Figure 2:

Grain size dependency of t_1_transit (squares) and t_2_transit (circles) determined from in situ experiments

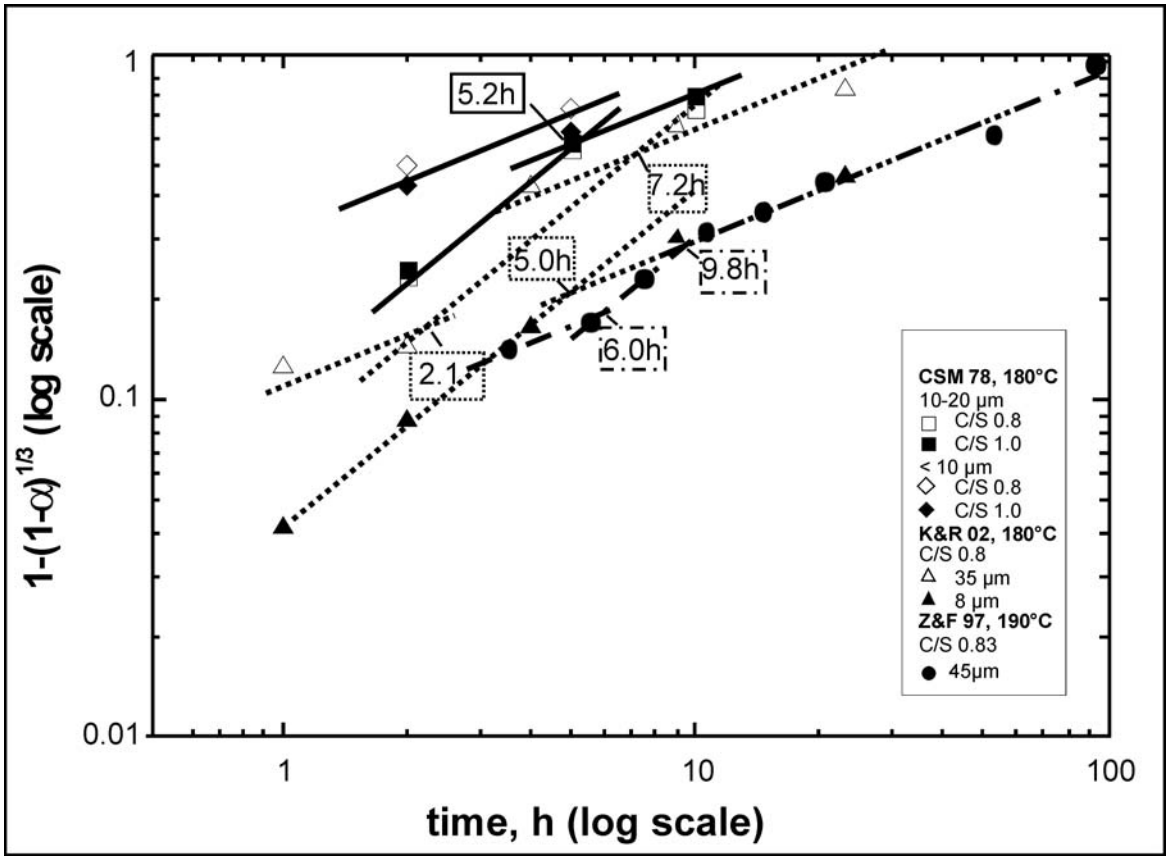

Figure 3:
Recalculated data from quenching experiments [6,7,9] in terms of equation (2) assigned transition times are displayed in boxes

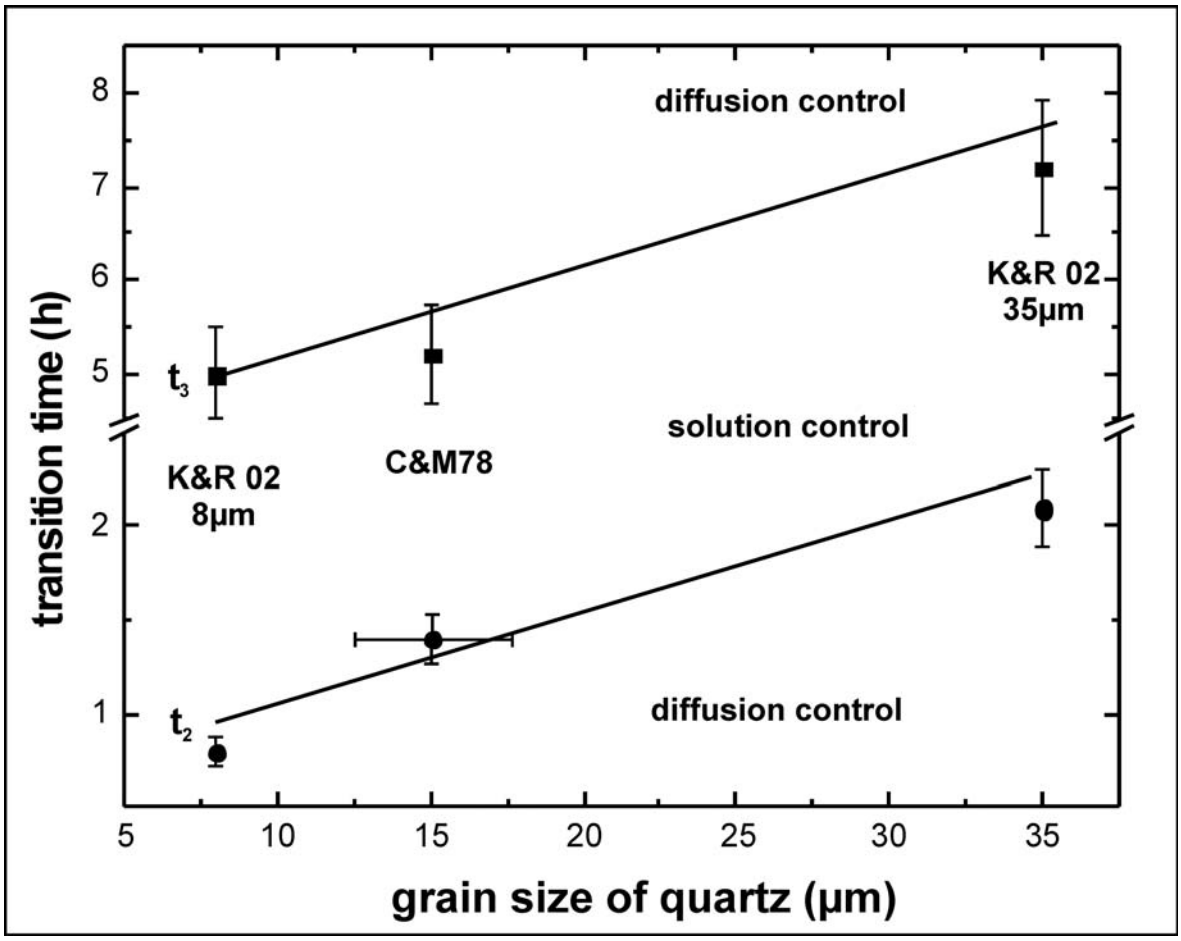

Figure 4:
Grain size dependency of t_2_transit (circles) and t_3_transit (squares) determined from recalculated quenching experiments [6,7]

Appendix E

The hydrothermal formation of 1.13nm tobermorite within the system CaO-SiO_2-D_2O: a kinetic study by in situ neutron diffraction

submitted to: Cement and Concrete research (under review)

The hydrothermal formation of 1.13nm tobermorite within the system CaO-SiO_2-D_2O: a kinetic study by in situ neutron diffraction

Saskia Bernstein[a,*], Karl Thomas Fehr[a]

[a]*Ludwig Maximilians Universität München, Department of Earth and environmental Sciences, Theresienstrasse 42/III, 80333 München, Germany*

**corresponding author: saskia.bernstein@gmx.de; Tel.: 00498921804276, Fax:00498921804176*

Abstract

1.13 nm tobermorite was synthesized hydrothermal within the system CaO-SiO_2-D_2O simulating the conditions during the hydrothermal hardening of aerated autoclaved concrete. The reaction was monitored in situ by neutron diffraction at the D20 powder diffractometer of the ILL (Grenoble) and the influence of reaction temperature (170-210 °C) and grain size of quartz (8 and 16µm) was investigated. The experiments revealed the non isokinetic nature of the mineral forming reaction with changes in the dominant reaction mechanisms between solution and diffusion control. Based on these insights rate constant ($9.924 \cdot 10^{-5}$ – $5.5 \cdot 10^{-3}$ s^{-1}) and for the first time activation energies (16.5-33.8 kJ/mol*K) were calculated.

keywords: 1.13nm tobermorite, neutron diffraction, reaction mechanism, kinetics

Introduction

The group of Calcium Silicate Hydrates (CSH-phases) is a comparatively rare mineral family with 40 members known from natural sources, nevertheless their synthetic equivalents are

used for a multitude of applications. One of the phases of most interest is the 1.13nm tobermorite ($Ca_5Si_6O_{16}(OH)_2$ *$4H_2O$) which is known to be formed during the hydrothermal hardening of aerated autoclaved concrete (AAC), a widely-used building material for light weight constructions. In consequence of the rapid increase in applications of such materials during the last 10 years a strong need of more detailed scientific research arose simultaneously. Fundamental knowledge on the nature of CSH-phases had been given by Taylor [1] with his studies on portland cement phases but there is still a demand for further investigations. The existence of various poorly ordered and metastable phases in the CSH-system hinders experimental work, thus the thermodynamics, kinetics and structural features of 1.13nm tobermorite and its neighbours are still poorly understood. The knowledge of these properties is of essential importance as the mechanical properties of the aforementioned building materials are strongly dependent from the type, amount and texture of the evolving CSH-phases.

For the tobermorite-family three members are known, the 0.9 nm tobermorite or riversideite, the 1.13 nm tobermorite or tobermorite sensu stricto and the 1.4 nm tobermorite also called plombierite. The numerical value in the name indicates the different d[002]-spacing due to different water contents in the structure. Tobermorite 1.4nm transforms into the 1.13 nm one by heating to 100 °C, further heating up to 300 °C leads to the 0.9nm tobermorite due to proceeding dehydration [2]. Some tobermorites are known not to shrink on dehydration and are therefore called “anomalous [3]. Recently a new member is described, crystallizing in monoclinic symmetry and hence called clinotobermorite. This polytype was first found in Fuka (Japan) [4] and also at Wessels mine (South Africa) [5]. The d-spacing in [001] is similar to the one of 1.13 nm tobermorite which is in focus of this study. An accurate description of the tobermorite structure in general and the one of 1.13 nm tobermorite in particular is complicated by presence of structural disorder evidenced by diffuse streaks or spots in X-ray or electron diffraction patterns [6]. A first structural model was given by

Megaw & Kelsey [7] in which they just outlined the main modules of the average structure without presenting any quantitative structural data. First cell dimensions are given by Hamid [6], determined by single crystal diffraction on a specimen from Zeilberg (Germany). According to the most recent structural refinement the structure of 1.13 nm tobermorite consists of layers of Ca_2O_7-polyhedras flanked on both sides by wollastonite-like Si-Dreiereinfachketten running along [010] [8] as the basic structural unit.

Two alternative occupied positions of the silicate chains shifted by b/2 and two opposite orientations of the bridging tetrahedron in the chain [6] lead to long range stacking disorder in both natural and synthetic 1.13nm tobermorite. Merlino et al. [2;8] successfully described the order-disorder character of 1.13nm tobermorite (normal and anomalous) by means of OD-theory [9]. Moreover they have shown that the difference in the thermal behaviour is not related to a different arrangement of the tetrahedral chains [10] but rather by the presence of interlayer Si-O-Si linkage in the anomalous tobermorites and their absence in the normal ones.

In 1.13nm tobermorite the composite layers of one calcium and two silicate layers are bound together by an interlayer containing calcium ions and water molecules. The interlayer contains variable amounts of calcium so that charge balance is achieved by variation of hydrogen atoms bonded to the silicate chains. Therefore, the variable occupancy of calcium in these layers allows the Ca:Si ratio to vary from $Ca_5Si_6O_{16}(OH)_2$ *$4H_2O$ ($C_5S_6H_5$) to $Ca_4Si_6O(OH)_2$ *$2H_2O$ ($C_4S_6H_3$) [8;11]. In AAC, 1.13 nm tobermorite is close to the composition $Ca_5Si_6O_{16}(OH)_2$ *$4H_2O$ and occurs in association with semi-crystalline CSH-phases CSH (I) and CSH (II) as minor components. In contrast to tobermorite, these phases are highly disordered and display a wide range of compositions. They are classified by their Ca/Si ratio: CSH (I) with a Ca:Si ratio <1.5 and CSH (II) with a Ca/Si ratio > 1.5 according to Taylor [11;12].

There has been a lot of work in this field aimed at understanding the formation mechanisms and growth kinetics of CSH-phases [13; 14]. But little quantitative data exist on the kinetics

of 1.13 nm tobermorite formation. In addition there is no agreement on the nature of the reaction mechanism. Some studies proposed it being solution controlled and other authors determined a diffusion controlled mechanism. as pointed out in detail by Klimesch et al.[15].

The reaction mechanism and kinetics of the formation of 1.13 nm tobermorite in the pure cement-free system CaO-SiO_2-H_2O from lime, silica and water under hydrothermal conditions were determined by quenching experiments at 180°-190 °C/P_{sat} [12;13;16] and by an in-situ Neutron diffraction experiment [17] as well. Quenching experiments reveal the disadvantage of missing data for the early evolution of phases in time and have prevented a quantitative kinetic description so far.

The major aim of this study was to determine the influence of reaction temperature and quartz grain size on the formation of 1.13 nm tobermorite in terms of reaction mechanism and reaction rate. Therefore, the reaction mechanism was determined by in situ neutron diffraction experiments at different temperatures (170,190,210 °C) and a varying grain size of the quartz component (16 and 8 µm). Based on this experiments, reaction constants and activation energies were calculated.

Methods and experimental setup:

Pure SiO_2, CaO and D_2O were used as starting materials to prepare the samples for neutron diffraction. In order to obtain a low background noise in the diffraction patterns hydrogen free substances are necessary. Therefore heavy water (Merck, Uvasol, >99.8%) was used as liquid reactant. CaO used was produced by heating calcium carbonate (Merck p.a.), having a particle size of <0.090 mm at 1250 °C for 14 h. The source of SiO_2 was ground Miocene quartz sand (SiO_2 > 99.5 wt.-%) supplied by the Quarzwerke Company in Frechen, Germany, revealing a medium grain size of 8 µm (SH500) and 16 µm (W12) and a specific surface of 0.9 m²/g and

1.6 m²/g, respectively. The grain size and the specific surface was determined by Gas-absorption (BET) at Quarzwerke Frechen.

The solid initial materials were mixed well using mortar and pistil then the required amount of D_2O for a water/solid ratio of 0.8 was added. The CaO/SiO_2 ratio was set to 0.5, the exact initial weight can be taken from Table 1. The compound was poured into a mould and stored in a drying furnace for 60 minutes to obtain a cylindrical greenbody of 8 cm in length and 1.5 cm in diameter of sufficient solidness.

For neutron diffraction experiments a hydrothermal autoclave was designed consisting of a steal tube and a bottom part with the sample support and the D_2O reservoir as described by Zürn et al. [18] with modifications concerning the housing of the thermocouples and the evacuating valve (see Fig. 1). The temperature during the experiments was controlled and regulated by two thermocouples on the bottom and inside the sample. The whole cell was heated using a vanadium furnace. The desired temperatures of 170, 190 or 210 °C were reached after a heating period of 60 minutes and subsequently the real experiment started. After the experiment was completed, the furnace was turned off for cooling down. The wavelength was set to 2.4 Å by applying a pyrolitic graphite monochromator (HOPG (002)) at a take-off angle of 42°. This set up leads to an effective neutron flux of 4.2×10^7 n $s^{-1}cm^{-2}$ which provides the possibility to measure a wide 2Θ range (8-156 °2Θ) accompanied by a sufficient time resolution of one diffraction pattern per minute and good counting statistics. A wide 2Θ range is important especially for the low values of 2Θ to record also the basal reflections of 1.13 nm tobermorite which are expected at d-values of 11.3 Å. Once the experiment was succesfully finished, the now hydrothermal hardened sample and the remaining eluate was kept for possible further investigation.

The obtained enormous amount of neutron diffraction data of up to 600 patterns for experiments conducted at 170 °C/Psat were handled with the LAMP software provided by ILL [19].

The time-resolved neutron diffraction patterns were taken within the range of 8° to 153.6° 2-θ at λ = 2.4 Å to allow the analysis of d-spacing up to 11.3 Å, where the basal (002) reflection of the evolving 1.13 nm tobermorite is expected. The mechanisms of the 1.13 nm tobermorite forming reaction can be evaluated on the basis of the reaction conversion of quartz according to Chan et al [13] assuming that there are no seeds in the reactants and the growth rate is low:

$$1-(1-\alpha)^{\frac{1}{3}} = kt^{1/n} \qquad (1)$$

where α gives the reaction conversion of quartz, k the reaction constant and t the reaction time. According to equation 1 the factor n reveals information on the reaction mechanism. If n=1 the reaction is solution controlled (phase boundary model), if n=2 the reaction is diffusion controlled (Jander equation) [20]. Values for α were calculated from the decreasing integral intensity of the (101)-Bragg reflection of quartz. The integral intensity was obtained by using the peak fitting-routine "STR_fit" implemented in the Large Array Manipulation Program (LAMP) provided by the ILL [19]. The diffraction patterns were fitted in the range from 41 to 44 °2Θ, the peak shape was set to Pseudo-Voigt and a linear background was chosen. By applying equation (1) to these data and plotting them in logarithmic scale, one obtains information on the reaction mechanism from the slope of the data points. The complete consumption of portlandite was determined by the disappearance of the (101) reflection at 54.3° 2Θ. The first occurrence of 1.13 nm tobermorite was determined by the appearance of (hk0) reflections at 46° 2Θ.

Results:

The results for the reaction conversion of quartz in terms of equation (1) for each experiment are depicted in Figure 2.

What immediately becomes apparent is that the experiments cannot be described applying one slope over the whole reaction progress. The experiments can be divided into different segments and compared to each other by the changing transition times from one segment to the other. The different transition times for all experiments are summarized in Table 2.

(Table 2 here)

The changes in slope could now lead to the assumption that the chosen kinetic model of Chan [13] is not valid for the investigated reaction. However, if one surveys the single segments of each curve they are either describable with a slope of 1 or 0.5 referring to an exponent of n= 1 or n= 2 in equation (1), respectively. Interpreting this in terms of the reaction mechanism it implies changing reaction mechanisms with the reaction progress. This is also confirmed by the changing Ca/Si ratio during the proceeding reaction depicted for the run at 190 °C/ P_{sat} and16mm quartz (Fig. 3). First the Ca/Si ratio of the evolving products increases to a maximum of 1.4 after 230 min and then decreases again and converge to the theoretical Ca/Si ratio of 1.13 nm tobermorite after 500 min of reaction [17]. The same effect of first increasing and then decreasing Ca/Si Ratio was described by Klimesch & Ray [14]

For all experiments one can observe changes from solution controlled mechanisms to diffusion controlled ones. An additional change back to a solution controlled part is present for experiment 1, 2, 3 and 4 (Table 1). Comparing the transition times, the consumption of portlandite and the occurrence of 1.13 nm tobermorite, one can notice a strong influence of the employed grain size of quartz and the reaction temperature.

For the experiment conducted at 210 °C/P_{sat} (Exp 3 in Table 1, Fig. 2e), applying a grain size of quartz of 16 µm, the first transition from a solution to a diffusion controlled mechanism occurs after 30min and the second one back to solution control after 228min. Portlandite is expensed after 142 min within the diffusion controlled part and first reflexions of 1.13 nm tobermorite could be assigned after 250 min. Using the fine grained quartz (8µm) at the same conditions, (exp.6 in Table 1 and 2, Fig. 2f) a considerable acceleration of the reaction can be

detected. The first transition occurs at 12min and the second at 150 min of reaction time, 18 and 78 min earlier as in experiment 3. Likewise, portlandite is already expensed after 60 min and 1.13 nm tobermorite occurs after 140min, at the end of the diffusion controlled part.

Plotting the transition times against the reaction temperature a trend of increasing transitions times with increasing temperature becomes apparent for the experiments employing quartz 0f 16 µm grain size (Fig 4a). T1_transit ascends from 10 min at 170 °C to 30 min at 210 °C (Table 2). The influence of increasing temperature becomes more distinct at t2_transit, it increases from 30 min at 170 °C over 190 min at 190 °C up to 230 min at 210 °C (Fig 4a, Table 2).

Whereas the times of portlandite consumption and 1.13 nm tobermorite occurrence shows an opposite trend. The time decreases from 254 min and 374 min at 170 °C/P_{sat} to142 min and 250 min at 210 °C/P_{sat} with decreasing temperature, respectively (see Fig. 4b, Table 2). One could also detect a temperature dependence of the length of the diffusion controlled segment. An increase in temperature leads to an extension of the period of diffusion control (Fig. 4a).

Experiments employing the 8 µm quartz (Exp. 4,5,6 in Table 1 and 2, Fig 2 b,d,f) show a slightly different behaviour.

What stands out is the missing second change back to a solution controlled mechanism for the experiments at 190 and 170 °C/P_{sat} (exp. 4,5 in Tab 1&2, Fig. 2d,f). Hence, just t1_transit could be determined for all three experiments revealing a strong decrease from 93 min over 65 min down to 12 min with rising temperature (see exp 6,5,4 in Table 2, Fig.5). Likewise, the consumption of portlandite is accelerated from 70 to 60 min with increasing reaction temperature (see exp 4,5,6 in Table 2; Fig 5). The same trend can be determined comparing the first occurrence of 1.13 nm tobermorite at 87min at 190 °C/P_{sat} and 105 min at 170 °C/P_{sat} (exp 4 and 3 in Table 2, Fig. 5). For the experiment at 210 °C/P_{sat}, a change back to a solution controlled reaction can be detected and the occurrence of 1.13 nm tobermorite seems to be

retarded (140 min) compared to the experiments at lower reaction temperatures (see exp. 6 in Table 2, Fig 5).

Rate constants for the overall reaction progress were calculated using equation (1) assuming slopes of 1 (n = 1) and 0.5 (n = 2) for a solution and diffusion controlled reaction mechanism, respectively ($9.924 \cdot 10^{-5}$ – $5.5 \cdot 10^{-3}$ s^{-1},see Table 2).

The change of the rate constants with increasing specific surface for the three investigated reaction temperatures clearly shows an increase as depicted in Figure 6. Based on the calculated rate constants at three different temperatures, activation energies ($E_{A)}$ can be determined according to the Arrhenius equation (2) by plotting the data according to equation as follows

$$k = A \cdot e^{-\frac{E_A}{RT}} \quad (2)$$

where k is the rate constant, E_A the activation energy, T the temperature in Kelvin, R the gas constant and A the pre-exponential factor. The pre-exponential factor A is equivalent to the amount of collisions between reactants with energies higher than the activation energy. Its temperature dependence can be neglected due to the fact that the exponential part changes much stronger with temperature. From experiments with coarse quartz E_A could be determined for the three different segments of the reaction. Whereas for the experiments with fine quartz, E_A could just be determined for the first solution controlled segment, due to the fact that just one experiment shows two changes in the reaction mechanism. Experiments using fine quartz reveal remarkably lower values for E_A of 16.5 kJ/mol*K compared to 30.8 kJ/mol*K for the ones using coarse quartz (Fig. 7).

Discussion

Neutron diffraction experiments were conducted to determine the reaction kinetics of 1.13nm tobermorite formation in the system $CaO\text{-}SiO_2\text{-}D_2O$. The varying slopes for the reaction conversion of quartz after applying the kinetic model of Chan et al. [13] indicate a change in the present reaction mechanism between solution and diffusion control during the proceeding reaction. The initial step of the reaction is controlled by the solution of quartz and its reaction with portlandite, leading to the formation of a layer of semicrystalline CSH-phases surrounding the quartz grains as shown in Figure 8 for AAC steam cured at 190 °C/P_{sat}, previously published by Zürn et al [18]. The second part of the reaction is controlled by the diffusion through this layer of CSH-phases and portlandite is expensed completely, however, the two experiments applying the 8µm quartz conducted at 170 and 190 °C/ P_{sat} do not show further changes in the reaction mechanism. In contrast, all other experiments of this study show a second change back to diffusion control (see Fig. 2). If this second change is present the first reflections of 1.13 nm tobermorite occur within the last diffusion controlled segment of the reaction. Implying that 1.13 nm tobermorite is formed by the reaction of quartz with the primarily formed semicrystalline CSH-phases.

This acceleration of the reaction can be explained by the increase in specific surface of quartz with decreasing grain size. A 50% reduction of the mean grain size results in a 44% increase of the reactive surface. An increase in specific surface does not only accelerate the reaction, but it also has a strong influence on the present reaction mechanisms as well, demonstrated by the missing second diffusion controlled segment in the experiments at 170 and 190 °C/P_{sat} applying the 8µm quartz. At 210 °C/ P_{sat} with a grain size of quartz of 8 µm again two changes are present.

Elevating the reaction temperature using 16µm quartz causes an increase in the transition times between the different reaction mechanisms. The period of diffusion control seems to

extend (see Fig 4a), whereas the consumption of portlandite and the formation of 1.13 nm tobermorite is accelerated by rising the reaction temperature (Fig. 4b).

In experiments with the fine quartz fraction, t1_transit clearly shows a decrease by increasing the reaction temperature (Fig. 5). The time needed to consume portlandite is as well decreased by elevating the reaction temperature but this trend could not be detected for the 1.13 nm tobermorite occurrence. At first the formation of 1.13 nm tobermorite was slightly accelerated by increasing the temperature but at 210 °C it could not be detected before 140 minutes of reaction. This means a retarding of tobermorite formation at high temperatures using fine quartz powder. This effect can be attributed to the metastable formation of 1.13 nm tobermorite beyond its stability field under these conditions [16]. Comparing the increasing intensities of 1.13 nm tobermorite hk0 and 00l reflections, it stands out that the (hk0) reflections occur before the (00l) reflections (see Fig: 3). This can be interpreted in terms of how the crystallization of 1.13 nm tobermorite takes place. It starts with the of nanoscale ab-planes which then, at a later stage of the reaction, start to stack along [001] to form the characteristic lathlike tobermorite crystals.

With decreasing grain size of quartz the calculated rate constants are increasing at a given temperature(Fig. 6). Based on these data, activation energies for the pure system CaO-SiO_2-D_2O were calculated for the first time. The calculated values (Table 2) for coarse quartz experiments, 30.8 kJ/mol*K (solution controlled segment) and 33.8 kJ/mol*K (diffusion controlled segment), are within the range of activation energies for the Al-bearing system determined by Shaw et al. [21]. Activation energies for experiments using fine quartz (16.5 kJ/mol*K, Tab. 2) are considerably below those values. This may be due to the fact that Shaw was assuming an isokinetic reaction and applying a slope of 1 to the Arrhenius equation.

There exist several studies trying to determine the reaction kinetics of 1.13 nm tobermorite and describe the influence of the reaction temperature and grain size of quartz by performing quenching experiments. Those experiments were not interpretable at all with the hitherto level

of knowledge of an isokinetic reaction. Now, taking into account that the reaction mechanism changes between solution and diffusion control, this is possible. Based on the results and new insights in the1.13 nm tobermorite forming reaction kinetic data obtained from quenching experiments [14;22,23] were recalculated in terms of equation (1,) applying two different slopes (n=1 and n=2). The transition temperatures were determined (Fig.9) and interpreted concerning to the grain size and temperature dependency (Fig.10). The results are in good agreement with findings of this study, showing an increase of reaction time with increasing grain size of quartz.

Conclusion:

It could be shown that in-situ neutron diffraction is a very suitable method to investigate the kinetics of the 1.13 nm tobermorite formation. For the first time the non isokinetic behaviour of the reaction could be evidenced by combining the high intensity of the D20 powder diffractometer at ILL together with an improved hydrothermal autoclave (HAND, Fig. 1) allowing constant reaction conditions and a fast and easy sample exchange. Furthermore exact times for the transition and the consumption of portlandite and the occurrence of 1.13 nm tobermorite could be determined. Based on the data obtained by applying the kinetic model of Chan et al. [13] on the values for the overall reaction progress rate constants could be determined for the first time. Likewise Shaw et al. [21] calculated rate constants for the tobermorite forming reaction but did not interpret their date in terms of the present reaction mechanism. By conducting experiments at three different temperatures, the temperature dependence and hence activation energies could be determined. The results of this study yield detailed kinetic data on the 1.13 nm tobermorite formation, which were just insufficient investigated in the past. Beyond that the conducted experiments yield information on the crystallisation path of 1.13 nm tobermorite as well. These data give a better understanding of the processes present during the production of AAC and could help to optimize production

conditions and recipes resulting in shorter production times and an optimal exploit of the available resources.

References:

[1] Taylor, H.F.W. 'The Chemistry of Cements, Ed., Academic Press, London, 1992.

[2] Merlino S., Bonaccorsi E. and Armbruster Th., The real structure of tobermorite 11 angstrom: normal and anomalous forms, OD character and polytypic modifications, Eur. J.Min. 13 (2001) 577-590

[3] Mitsuda T. & Taylor H.W.F., Normal and anomalous tobermorites, Min. Mag.42 (1978) 229-235,

[4] Henmi C. & Kusachi I., Monoclinic tobermortie from Fuka, Journal of the Japanese Association of Mineralogists, Petrologists and Economic Geologists 84 (1989) 374-379.

[5] Hofmann C. & Armbruster T., Clinotobermorite, $Ca_5[Si_3O_8(OH)]_2.4H_2O$ - $Ca_5[Si_6O_{17}].5H_2O$, a natural C-S-H(I) type cement mineral: determination of the substructure, Z. Kristallogr. 212 (1997) 864–873.

[6] Hamid S.A., The crystal structure of the 11Å natural tobermorite $Ca_{2.25}[Si_3O_{7.5}(OH)_{1.5}].1H_2O$, Z. Kristallogr. 154 (1981) 189–198.

[7] Megaw H.D., Kelsey C.H., Crystal structure of tobemorite, Nature 177 (1956) 390–391.

[8] Merlino S., Bonaccorsi E. and. Armbruster Th, Tobermorites: Their real structure and order-disorder (OD) character, Amer.Miner. 84 (1999) 1613-1621.

[9] Dornberger-Schiff K.:Grundzüge einer Theorie von OD-Strukturen aus Schichten, Abhandl. d. Deutsch. Akad. d. Wiss. zu Berlin. Klasse f. Chemie, Geol. u. Biol., 3 (1964) 1–107.

10] Wieker, W., Grimmer, A.-R., Winkler, A., Mägi, M., Tarmak, M., Lippmaa, E., Solid state high-resolution ^{29}Si NMR spectroscopy of synthetic 14Å, 11 Å and 9Å tobermorites. Cem. Concr. Res., 12 (1982) 333–339.

[11] H.F.W. Taylor, Hydrated calcium silicates. Part I. Compound formation at ordinary temperatures, J. Chem. Soc. 30 (1950) 3682.

[12] H.F.W. Taylor, *Proc. Vth Int. Symp. Chem. Cem.* **Vol II** (1968) 1-26

[13] Chan F., Sakiyama M. and Mitsuda T., Kinetics of the CaO-quartz-H_2O reaction at 120°C to 180°C in suspension, Cem.Concr.Res., 8 (1978) 135-138.

[14] Klimesch D. S., Ray A., Effects of silica reactivity on the nature and formation of Al-1.1nm tobermorite, J.Therm.Anal.Calorim., (2002) 995-1003.

[15] Klimesch D. S.; Ray A.; Sloane B., Autoclaved cement-quartz pastes: The effects on chemical and physical properties when using ground quartz with different surface areas .1. Quartz of wide particle size distribution, Cem.Concr.Res. 26 (1996) 1399-1408.

[16] Zuern S.G. & K.T. Fehr., Phase Relations and Thermodynamic Properties of 1.13 nm Tobermorite and Xonotlite, Proc. Joint ISHR & ICSTR Kochi, (2000) 286-289

[17] Fehr K.T., Huber M, Zuern S.G.; Hansen T., Determination of the reaction kinetics and reaction mechanisms of 1.13 nm tobermorite by means of in-situ neutron diffraction, Proc. 5th ICSTR, (2002) 37-40

[18] Zürn S., Fehr K.T., Hansen T., Design, Technique and Applicability of a Hydrothermal Autoclave for Neutron Diffraction (HAND) for Analyzing the Reaction Process of Steam Cured Building Materials Proc. Vth ICSTR East Brunswick, (2002) 33-36.

[19] LAMP, the Large Array Manipulation Program. http://www.ill.fr/data_treat/lamp/lamp.html

[20] D. Hancock and J.H. Sharp, Method of Comparing Solid-State Kinetic Data and Its Application to the Decomposition of Kaolinite, Brucite, and $BaCO_3$, J. Amer.Ceram.Soc. 55 (1972) 74-77.

[21] Shaw, S., Clark S. M., Hydrothermal formation of the calcium silicate hydrates, tobermorite ($Ca_5Si_6O_{16}(OH)_2$* $4H_2O$) and xonotlite ($Ca_6Si_6O_{17}(OH)_2$): an in situ synchrotron study, Chemical Geology 167(1-2) (2000) 129-140.

[22] Zürn, S. Fehr, K.T., Kinetic study on the crystallisation of calcium-silicatehydrates in steam cured building materials, Intern. Symp. Hydrotherm. Reactions, Gatlinburg, (1997).

[23] Chan, F., Mitsuda, T., Formation of 11 Å tobermorite from mixtures of lime and colloidal silica with quartz, Cem.Concr.Res., 8 (1978) 135-138.

Table 1

Reaction conditions, composition, employed grain size of quartz and corresponding specific surface of the conducted experiments.

run	temperature (°C)	quartz grain size (µm)	specific surface (m^2/g)	SiO_2 (g)	CaO (g)	W/M
1	170	16	0.9	20	10	0.8
2	190	16	0.9	30	15	0.8
3	210	16	0.9	30	15	0.8
4	170	8	1.6	16	8	0.8
5	190	8	1.6	16	8	0.8
6	210	8	1.6	16	8	0.8

Table 2

Transition times, portlandite expense, tobermorite occurrence and calculated rate constants and activation energies for the conducted experiments

run	t1_transit (min)	t2_transit (min)	port_out (min)	tob_in (min)	rate constants P1 (s^{-1}, x 10^{-5})	rate constants P2 (s^{-1}, x 10^{-3})	E_A solution controlled part (kJ/mol*K)	E_A diffusion controlled part (kJ/mol*K)
1	15	36	254	374	5.529(39)	0.885(03)		
2	42	150	120	360	4.754(14)	2.398(01)	30.8(16.04)	33.8(10.68)
3	30	228	142	250	7.667(10)	3.343(02)		
4	93	-	70	105	6.882(08)	4.863(03)		
5	65	-	64	87	9.924(17)	5.599(02)	16.5(11.15)	-
6	12	150	60	140	8.935(21)	2.651(01)		

Figure headings

Figure 1:

mechanical drawing of the hydrothermal autoclave for neutron diffraction designed for this study

Figure 2

Consumption of quartz versus reaction time for different reaction temperatures and grain sizes of quartz in terms of equation (1) (Chan et al., 1978) for the conducted experiments. Time of portlandite expense and 1.13nm tobermorite occurrence are marked by arrows, slopes with n= 1 or n=2 indicating a solution or diffusion controlled reaction mechanism, respectively.

Figure 3

Changing Ca/Si ration with increasing reaction time for the run at 190°/ P_{sat} and 16µm grain size of quartz after [17]

Figure 4

Temperature dependence of t1_transit and t2_transit (a) and portlandite expense and tobermorite occurrence (b) for experiments conducted with 16µm grain size of quartz

Figure 5

Temperature dependence of t1_transit (small graphic) ,portlandite expense and tobermorite occurrence (b) for experiments conducted with 8µm grain size of quartz

Figure 6

Rate constants versus specific surface for the first solution controlled part of the reaction

Figure 7

calculated activation energies (E_A) versus specific surface for the solution controlled segment of the reaction.

Figure 8:
Backscattered electrons image of AAC showing a large quartz grain (qz) next to semicrystalline CSH-phases (CSH) and 1.13nm tobermorite (Tob) crystallizing into the gap between qtz and CSH.

Figure 9
Recalculated quenching experiments [14;22,23] according to equation (1) ,determined transition times are given in boxes

Figure 10

transition time versus grain size of quartz from recalculated quenching experiments [14,22,23]

Figure 1

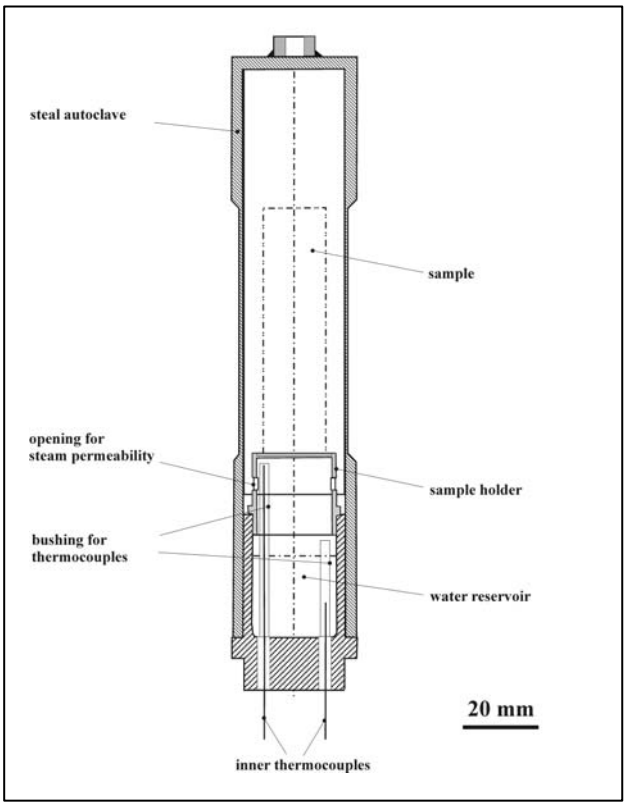

Figure 2

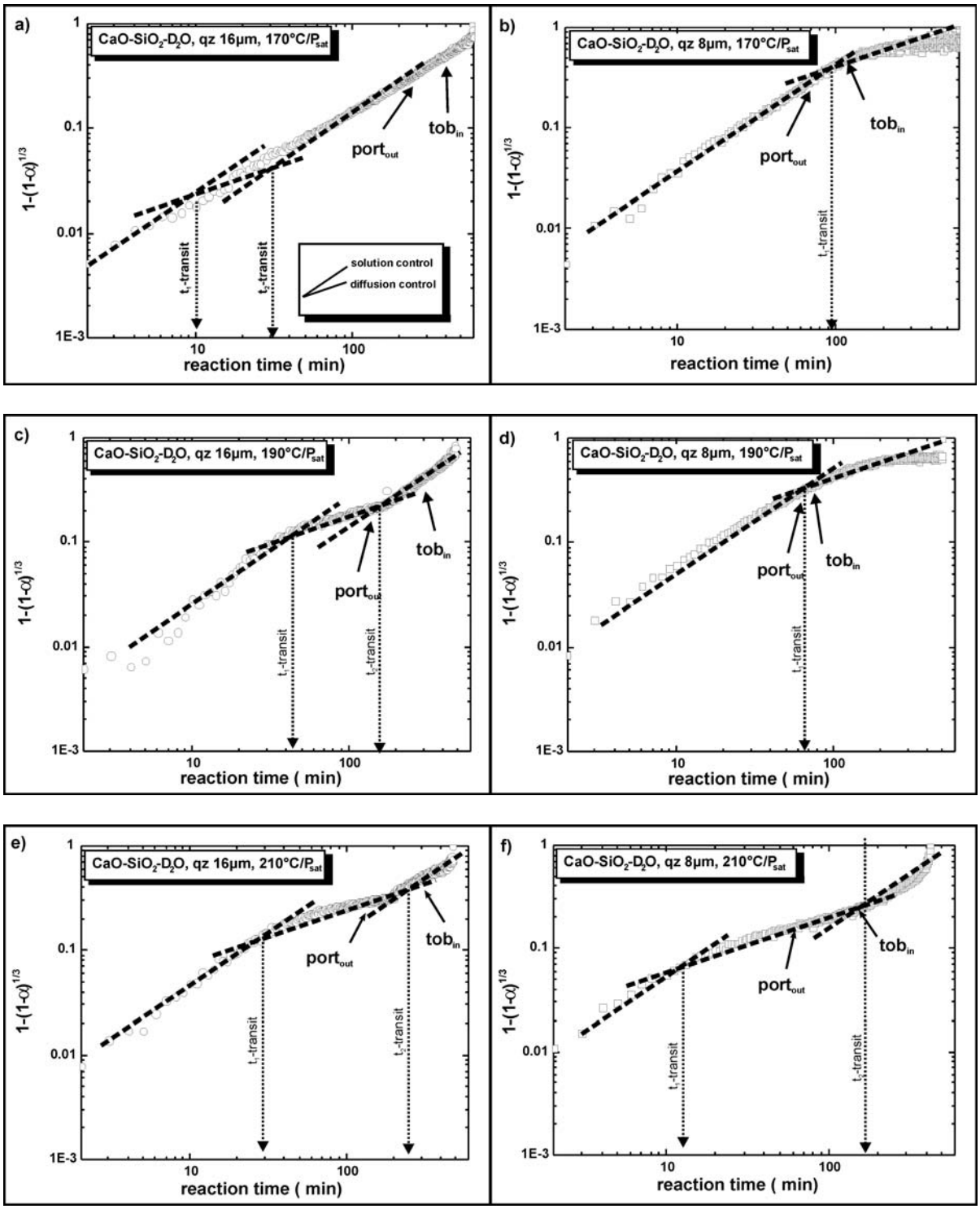
a)
CaO-SiO2-D2O, qz 16µm, 170°C/Psat
b)
CaO-SiO2-D2O, qz 8µm, 170°C/Psat
c)
CaO-SiO2-D2O, qz 16µm, 190°C/Psat
d)
CaO-SiO2-D2O, qz 8µm, 190°C/Psat
e)
CaO-SiO2-D2O, qz 16µm, 210°C/Psat
f)
CaO-SiO2-D2O, qz 8µm, 210°C/Psat
1-(1-α)^1/3
reaction time (min)
port_out
tob_in
t1-transit
t2-transit
solution control
diffusion control

Figure 3

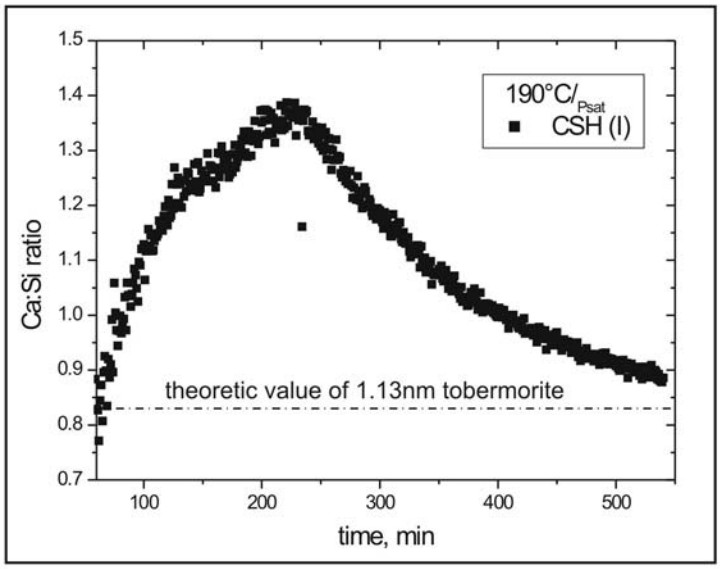

Figure 4

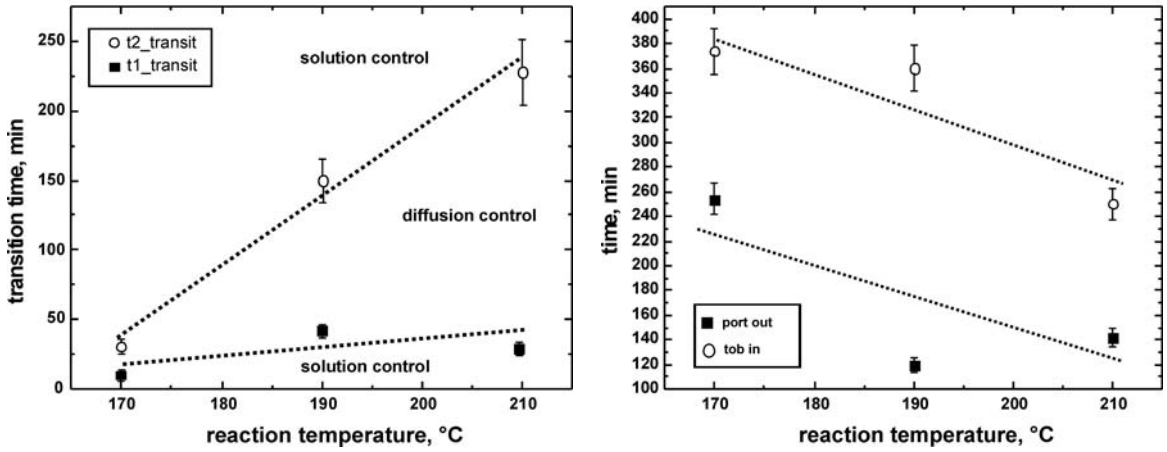

Figure 5

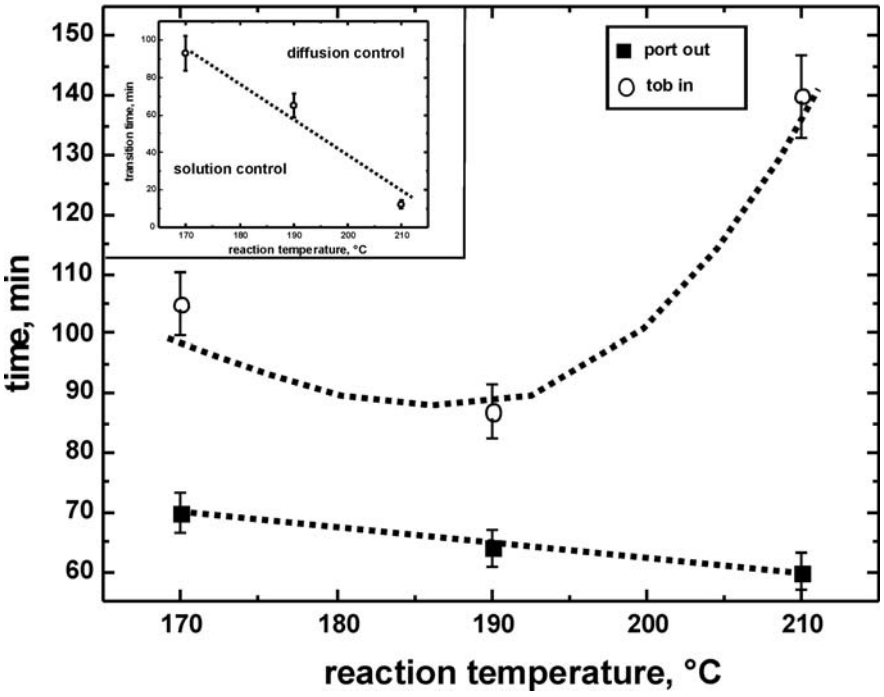

Figure 6

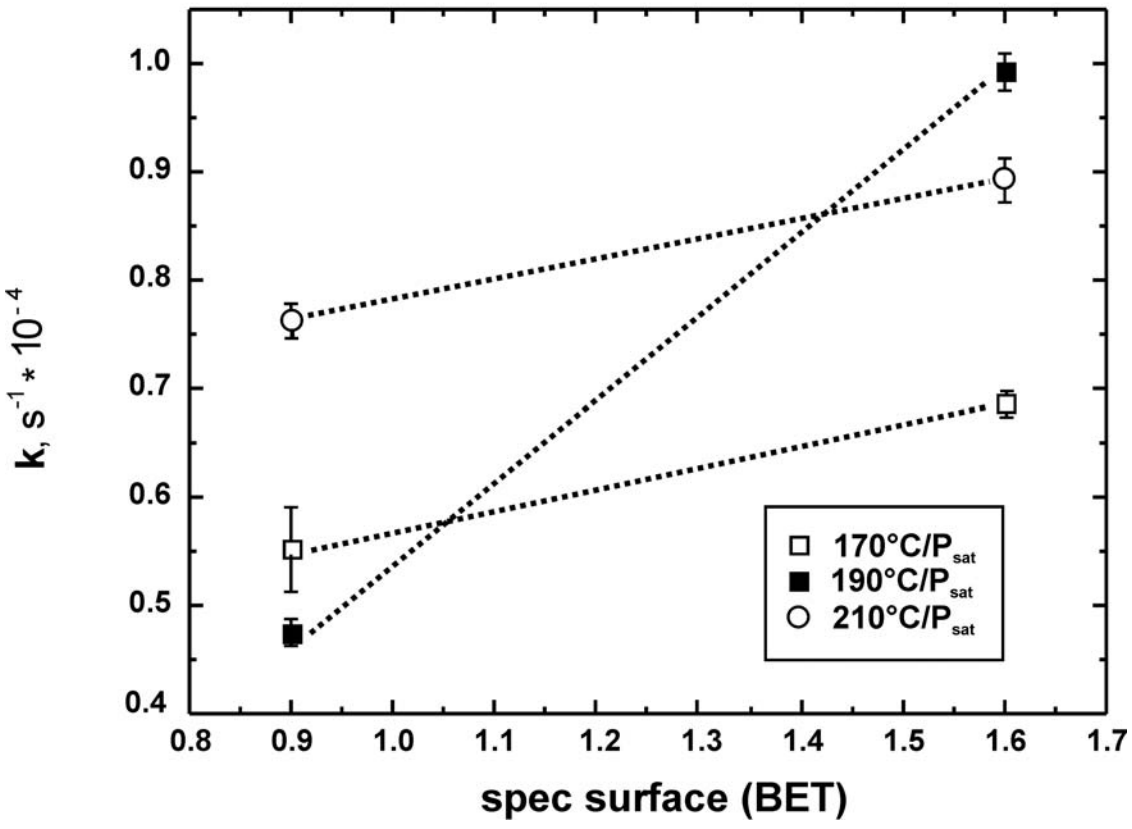

Figure 7

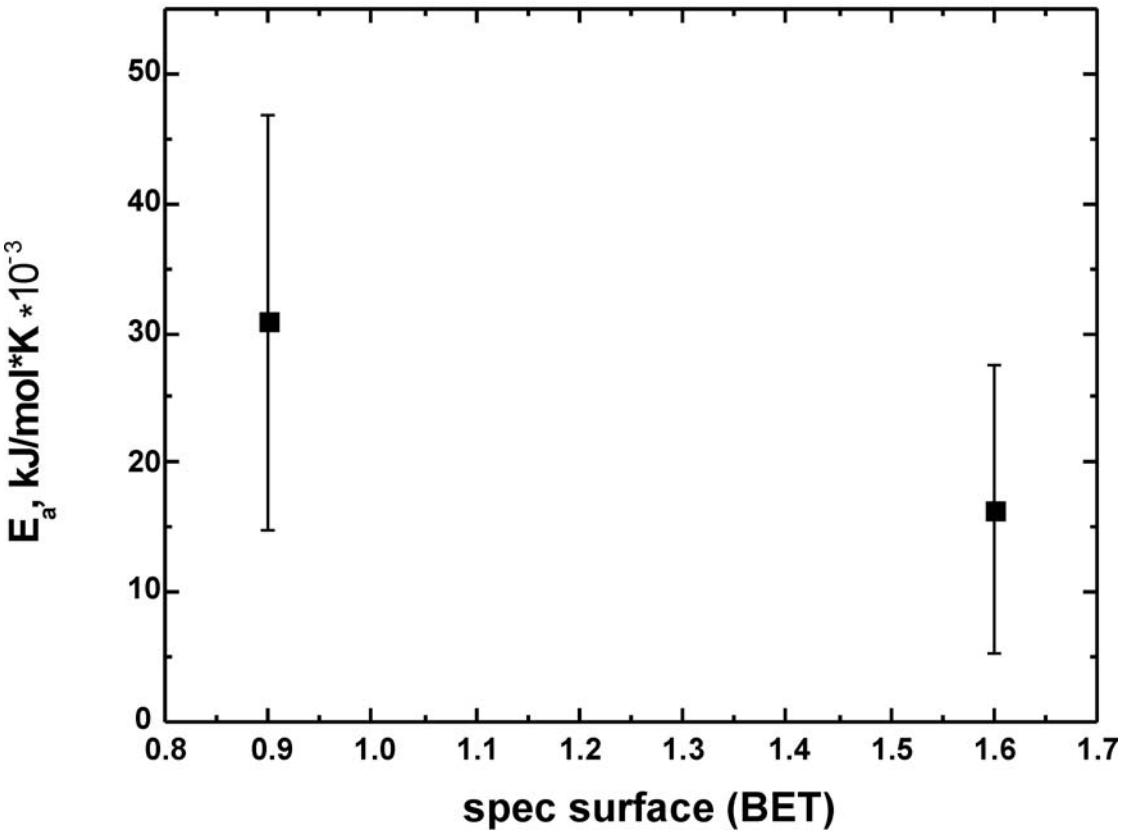

Figure 8

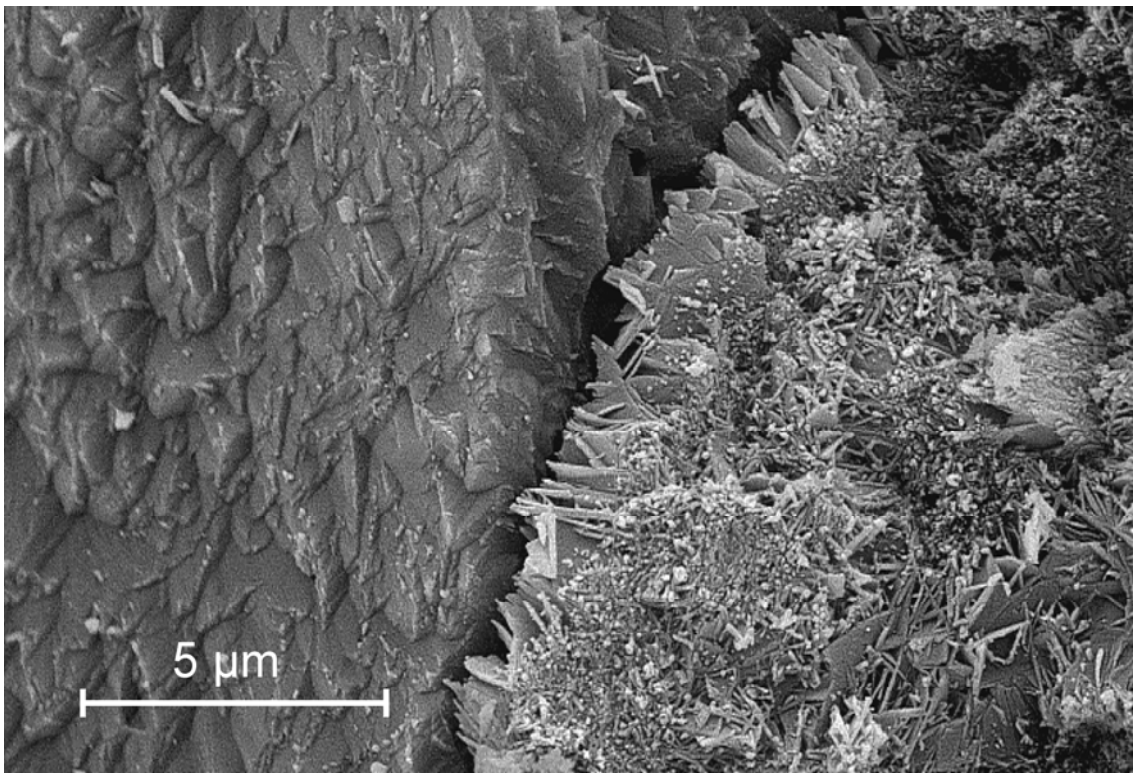

Figure 9

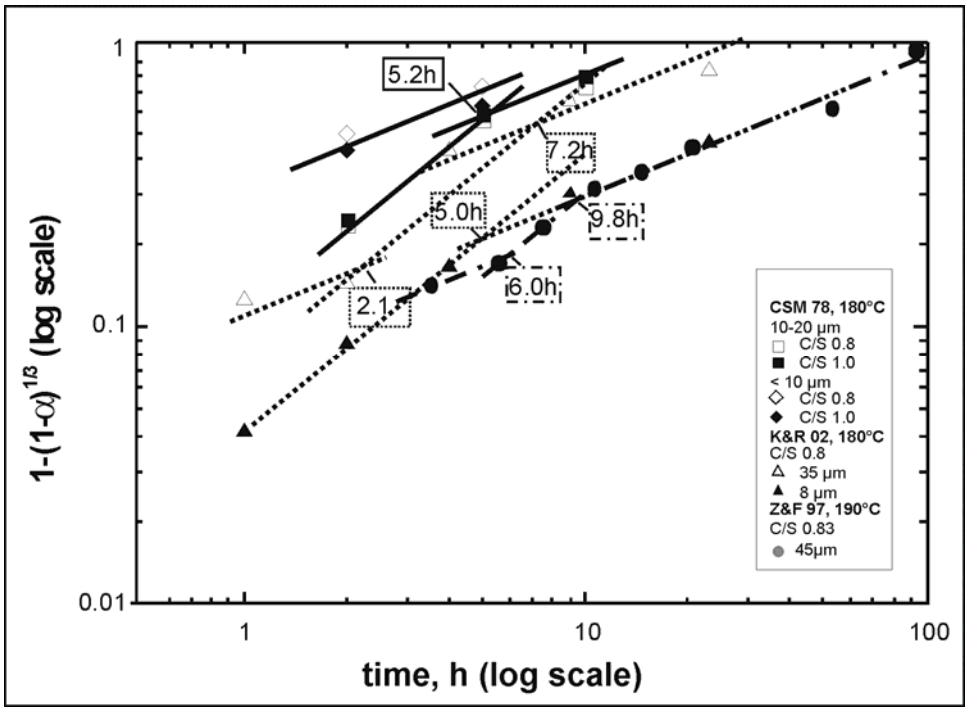

Figure 10